Electronic transport and flicker noise in graphene structures

Submitted by Alexey A. Kaverzin to the University of Exeter as a thesis for the degree of Doctor of Philosophy in Physics
November, 2011

I certify that all material in this thesis which is not my own work has been identified and that no material has previously been submitted and approved for the award of a degree by this or any other University.

Alexey A. Kaverzin
November, 2011

Abstract

In this thesis the properties of graphene are studied via the various aspects of the quantum transport: doping of the graphene surface with organic molecules, flicker noise and transport in the quantum Hall regime.

First, it was shown that certain molecules (toluene, aniline and water), which possess such common properties as non zero dipole moment and ability to undergo the electrochemical reaction, have a peculiar doping effect on graphene. The effect of toluene doping was studied in detail and is explained by the electrochemical reaction, which takes place in the vicinity of the graphene and results in a gate voltage dependent doping.

Second, the flicker noise in graphene and its relation to the scattering mechanisms were studied. The flicker noise as a function of the carrier concentration was demonstrated to be sensitive to the scattering potential determining the resistance of the graphene. Therefore, as it was suggested, the flicker noise can be used as a tool for determining the dominant scattering mechanism in graphene, although it was found that the resistance and noise can originate from different scattering potentials.

Also, the flicker noise spectrum was shown to decompose into individual lorentzians at low temperatures (below $\sim 25\,\mathrm{K}$), where the fluctuations of the resistance is supposedly coming from the random jumps of electrons between the conductive channel in the graphene flake and the nearby impurity states.

Third, the transport properties of the bilayer/trilayer graphene structure were studied at different temperatures and different magnetic fields including the quantum Hall regime. Bilayer and trilayer parts of the sample revealed the signatures of the quantum Hall effect predicted theoretically. The transport through the interface between bilayer and trilayer parts was also investigated. Signatures of the interface resistance were seen, although the observed behaviour is not explained. Under high magnetic fields the properties of the interface longitudinal resistance were described qualitatively by the classic transport equations.

Acknowledgements

I would like to show my deepest gratitude to the people whose persistent help and guidance were invaluable during the years of my studies in Exeter University.

I am very grateful to my former supervisor Prof. Alex Savchenko, who supported me a lot, not only in terms of my studies but also in terms of social life, especially during my first year of PhD. Prof. Savchenko continuously and convincingly conveyed to everyone, and to me in particular, his enthusiasm to the science.

A big thank you to my current supervisor Dr. David Horsell, with whom I have had very productive discussions, which summarised all the results I had and led to the publications. I would like to thank Dr. Andrey Shitov, who has willingly answered hundreds of my questions.

I wish to thank former students of our lab: Roman Gorbachev, Alexander Mayorov and Feodor Tikhonenko, who were my first teachers in all the measurement and fabrication techniques, and became the first friends I found here in Exeter. I owe a thank you to Adam Price for his continuous and detailed help with all the equipment in our lab. A big thank you to my colleagues Peter Hale, Freddie Withers, Aleksey Kozikov and Samuel Hornett, who were always there for advice and help of any sort. Thanks also due to the team of English native speakers of our lab, who were the first readers of all my papers, presentations and this thesis.

I would like to express my gratitude to the team of our technicians. David Manning, Adam Woodgate and David Gregory have kindly supplied our lab with the liquid helium. Paul Wilkins has helped me with many bits of the experimental set ups.

I would like to express my appreciation to the University of Exeter as this work would not have been possible without its financial assistance.

I am very thankful to my friends Sergey Alyamkin and Alexey Galda who believed in me since we were at school. A special thank you to my housemates and friends Ivan Khrapach, Timofiy Khodkov and Alexander Markevich for the great welcoming atmosphere in our house.

Of course, I cannot forget to thank my parents and my sisters for their unconditional love and support through all the years of my study.

Contents

List of Figures

List of Tables

Introduction

During the last 7 years, interest in graphene has been continuously growing. A significant development has been achieved in investigation of both fundamental properties and applications of graphene. Graphene structures provide a large variety of different types of conducting particles: from massless particles in monolayer to particles with a diverging effective mass near the charge neutrality point in ABC stacked trilayer. All these particles are of a different nature than that studied in conventional semiconductor devices and are of a great interest for fundamental science. Multiple extraordinary properties of graphene have being under study in an attempt to employ this material in electronic devices. A rather big step forward has been made by developing a technique for producing graphene on a large scale.

This work is dedicated to studying different aspects of the electronic transport in graphene structures. In particular, the doping effect on the graphene conduction is discussed for different organic and inorganic molecules; the flicker noise is studied as a phenomenon related to the scattering of the carriers; and also the effects of the temperature and magnetic field on the transmission through the boundary between bilayer and trilayer is described including the quantum Hall effects in both bilayer and trilayer graphene.

Chapter 1 gives an introduction to the basic properties of graphene. Starting from the tight-binding approximation the Dirac equation for the particles in graphene is derived and the most important features of graphene particles for electronic transport are discussed. The theoretical background of scattering and flicker noise in graphene is given. The fabrication technique of a standard graphene transistor along with a typical dependence of the device resistance on the gate voltage are described.

Chapter 2 describes the various aspects of the interaction between graphene and organic molecules: importance of the dipole moment, the role of the π-π interaction.

The main focus of the chapter is on the electrochemical nature of the doping effect of organic molecules.

Chapter 3 presents an investigation into the relation between flicker noise and the scattering mechanisms determining conductance in graphene. The behaviour of the resistance fluctuations at low temperatures and the appearance of the random telegraph signals are also discussed.

Chapter 4 presents the studies of the conductance of a graphene structure consisting of two regions with different number of layers. The effect of the temperature and high magnetic field is shown. The quantum Hall regime is investigated independently in both regions with a focus on that in trilayer part. The effect of the stacking in trilayer graphene on the signatures of the quantum Hall effect is discussed.

Chapter 5 summarises all the unanswered questions, which appeared during the discussions in this thesis, and gives the suggestions for further work.

Chapter 1

Theoretical background, sample fabrication and measurement techniques

1.1 Dispersion relation

1.1.1 Monolayer of carbon atoms

Carbon is the sixth element on the periodic table and its allotropes are believed to have been discovered several thousand years ago, well before the formation of theoretical description of the properties of these materials. Carbon has 4 valence orbitals in the outer shell: $2s$, $2p_x$, $2p_y$ and $2p_z$. Depending on the environmental conditions, the bond between carbon atoms is formed by means of different types of hybridization of these orbitals. For instance, in diamond, sp^3 hybridization leads to 4 equivalent bonds between each atom and its 4 neighboring atoms. Graphite is a layered material, where each layer consists of sp^2 hybridized atoms with 3 bonds lying in plane and one bond sticking out of the plane.

In this thesis a single layer of carbon atoms, which is called graphene, will be considered. It is a one atom thick material with a simple hexagonal structure in the plane. For each atom there are three σ orbitals, which hybridize in sp^2 configuration, and one π orbital perpendicular to the plane. Strong σ bonds connect each carbon atom with its neighbors and an additional bonding between atoms comes from the weak overlap between the π orbitals.

1.1.2 Tight-binding approximation

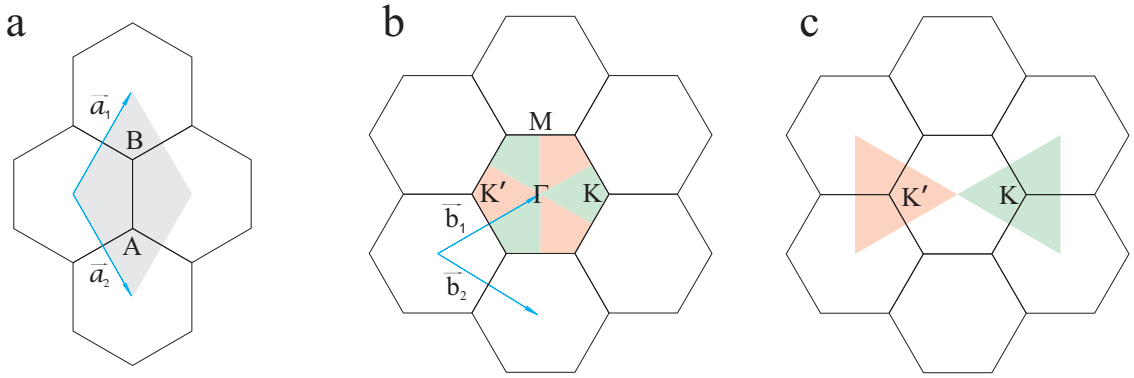

Figure 1.1: Real (a) and reciprocal space (b, c) graphene lattices with unit vectors and shadowed unit cells.

The unit cell of graphene has a two atom basis, Fig. 1.1(a). The two sublattices formed from the basis atoms are inequivalent and called A and B sublattices. Unit vectors of the real space graphene lattice $\vec{a}_1, \vec{a}_2$ and reciprocal space lattice $\vec{b}_1, \vec{b}_2$ are shown in Fig. 1.1(a) and (b), respectively.

$$\begin{aligned} \vec{a}_1 &= \tfrac{a}{2}\left(1, \sqrt{3}\right) & \vec{b}_1 &= \tfrac{2\pi}{a}\left(1, \tfrac{1}{\sqrt{3}}\right), \\ \vec{a}_2 &= \tfrac{a}{2}\left(1, -\sqrt{3}\right) & \vec{b}_2 &= \tfrac{2\pi}{a}\left(1, -\tfrac{1}{\sqrt{3}}\right), \end{aligned} \tag{1.1}$$

where $a = \sqrt{3}a_{C-C}$, and a_{C-C} is the length of the $C-C$ bond ($a_{C-C} = 1.42\,\mathring{A}$).

Because of the symmetry of the σ orbitals and the asymmetry of the π orbital perpendicular to the lattice plane, overlap between the π wave function and the σ wave function is zero. This allows us to consider the π band independently of the σ bands. Moreover, it has been shown by first principle calculations that the σ bands have a 10 eV gap near the Fermi level [1], and, therefore, do not contribute to the conduction at low energy excitations. Thus, in order to calculate the band structure of graphene near the Fermi level, one needs to evaluate only two π orbitals from different sublattices.

The crystal wave function $\Psi(\vec{k})$ satisfies the Schrödinger equation

$$H\Psi(\vec{k}) = E(\vec{k})\Psi(\vec{k}), \tag{1.2}$$

where $E(\vec{k})$ is the eigenvalue of the Hamiltonian, H, as a function of wave vector

$\overrightarrow{k}$. Within the tight-binding method the Eq. 1.2 for Bloch functions $\Phi_{A,B}$, which are constructed as a sum of the atomic wave functions, takes the form

$$\begin{pmatrix} H_{AA}(\overrightarrow{k}) & H_{AB}(\overrightarrow{k}) \\ H_{BA}(\overrightarrow{k}) & H_{BB}(\overrightarrow{k}) \end{pmatrix} \begin{pmatrix} \Phi_A \\ \Phi_B \end{pmatrix} = \begin{pmatrix} E(\overrightarrow{k})S_{AA}(\overrightarrow{k}) & E(\overrightarrow{k})S_{AB}(\overrightarrow{k}) \\ E(\overrightarrow{k})S_{BA}(\overrightarrow{k}) & E(\overrightarrow{k})S_{BB}(\overrightarrow{k}) \end{pmatrix} \begin{pmatrix} \Phi_A \\ \Phi_B \end{pmatrix}. \tag{1.3}$$

Therefore, the dispersion relation, $E(\overrightarrow{k})$, should obey the following equation

$$\begin{vmatrix} H_{AA}(\overrightarrow{k}) - E(\overrightarrow{k})S_{AA}(\overrightarrow{k}) & H_{AB}(\overrightarrow{k}) - E(\overrightarrow{k})S_{AB}(\overrightarrow{k}) \\ H_{BA}(\overrightarrow{k}) - E(\overrightarrow{k})S_{BA}(\overrightarrow{k}) & H_{BB}(\overrightarrow{k}) - E(\overrightarrow{k})S_{BB}(\overrightarrow{k}) \end{vmatrix} = 0, \tag{1.4}$$

since the determinant of a homogeneous system has to be zero in order to have a non-trivial solution. Matrix elements, H_{ij} and S_{ij}, are defined by

$$H_{ij} = \langle \Phi_i | H | \Phi_j \rangle \qquad S_{ij} = \langle \Phi_i | \Phi_j \rangle. \tag{1.5}$$

Atoms in sublattice A are indistinguishable from atoms in sublattice B, which allows one to simplify Eq. 1.4. Since the matrix elements H_{ii} and S_{ii} are determined by the interaction of atoms in sublattice i only, they should be independent of the sublattice index. That is, $H_{AA} = H_{BB}$ and $S_{AA} = S_{BB}$. Following the same logic it is concluded that H_{BA} is simply the complex conjugate of H_{AB}. Moreover, to a good approximation, one can assume that the wave functions between neighbouring atoms do not overlap, which means that $S_{AB} = S_{BA} = 0$ and $S_{AA} = S_{BB} = 1$. Therefore, the solution of simplified Eq. 1.4 reads

$$E(\overrightarrow{k})^{\pm} = H_{AA}(\overrightarrow{k}) \mp |H_{AB}(\overrightarrow{k})|, \tag{1.6}$$

where "$+$" and "$-$" correspond to conductance π^* band and valence band π respectively. Furthermore, for the nearest neighbour approximation, H_{AA} becomes constant. Taking into account that the π^* and π bands cross each other at the Fermi level, which is set to zero, the solution takes form

$$E(\overrightarrow{k})^{\pm} = \mp |H_{AB}(\overrightarrow{k})|. \tag{1.7}$$

The energy of the excitations of the Fermi sea is now measured with respect to the

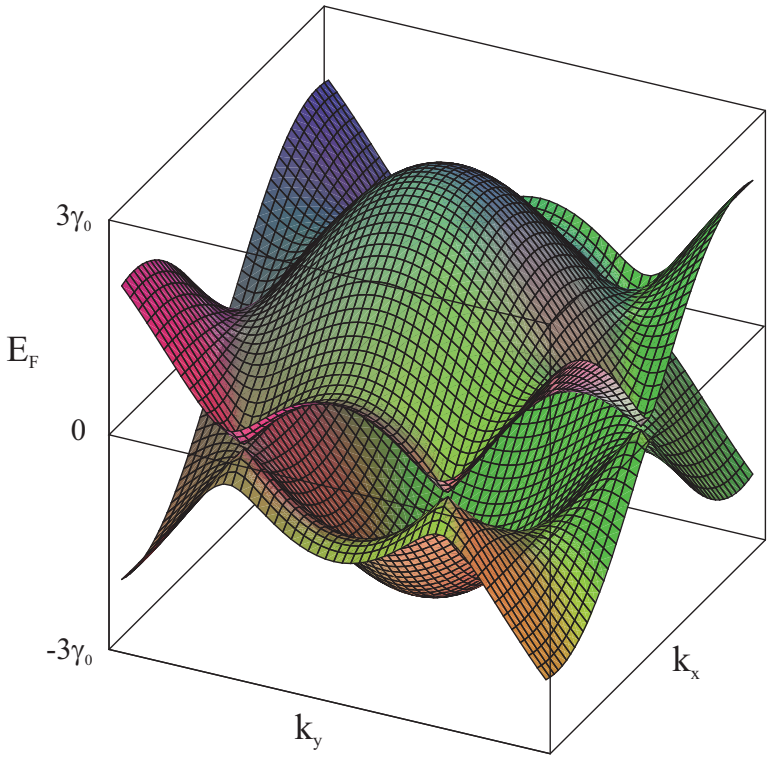

Figure 1.2: Calculated band structure of graphene. Due to the low resolution of the plotting the valence and conductance bands are not intersecting and, thus, forming a small band gap. However, with increased resolution this artificial band disappears.

Fermi level. Calculating the matrix element H_{AB} from Eq. 1.5 one can find [1]

$$E(\overrightarrow{k})^{\pm} = \mp\gamma_0\sqrt{1+4\cos^2(k_x a/2)+4\cos(k_x a/2)\cos(\sqrt{3}k_y a/2)}. \qquad (1.8)$$

where γ_0 is a transfer integral determined by the hopping amplitude of electrons between the two sublattices, and $\overrightarrow{k} = (k_x, k_y)$.

In Fig. 1.2, $E(\overrightarrow{k})$ is plotted as a function of (k_x, k_y). There are 6 points on the edge of the first Brillouin zone called K and K′ points, where the conductance and valence bands intersect. After combining all three K points together in one group and three K′ points in the other group, one can find an equivalent Brillouin zone with two separate regions in $\overrightarrow{k}$-space (Fig. 1.1, c). These regions are called K and K′ valleys with corresponding K and K′ points. The inequivalence of the two valleys comes from the inequivalence of the two sublattices in the graphene structure. Since both valleys contribute to the conduction, both of them have to be considered in understanding the electronic properties.

Reliability of the tight-binding method was confirmed by numerical calculations.

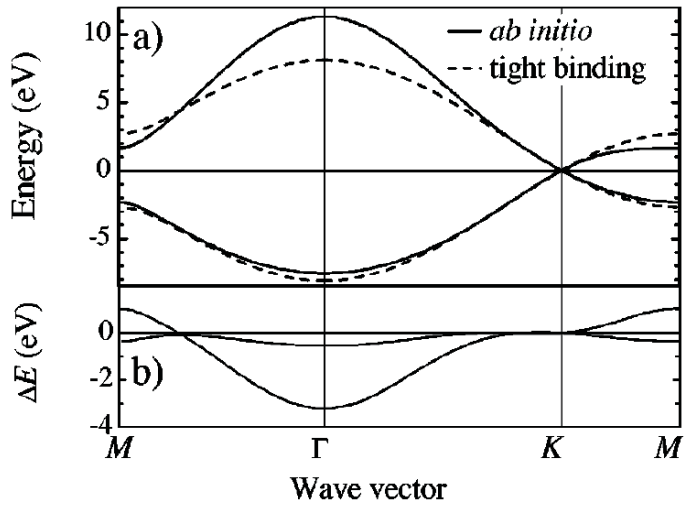

Figure 1.3: Comparison of ab-initio calculations and tight-binding calculations of π^* and π bands of graphene. Adapted from Ref. [2].

As an example, in Fig. 1.3 the results of ab-initio calculations are presented in a comparison with the analytically derived expressions obtained within the tight-binding calculations model. As it is seen the analytical expressions are in a good quantitative agreement with the calculations only in the vicinity of the K and K′ points.

1.1.3 Linear dispersion relation

Crossing of the π valence band and π^* conductance band at the K and K′ points has significant consequences on the observed electronic properties of graphene. The crossing point lies exactly at the Fermi energy (which is usually set to zero), therefore making linear parts of π and π^* bands available experimentally. This linear part of the spectrum provides an extraordinary electronic transport in graphene interesting in many aspects [3, 4].

The range of energies, where the linear relation can be used, is set by γ_0. In Ref. [1] by fitting the band structure obtained from numerical calculations with Eq. 1.8 γ_0 was estimated to be $\sim -2.7\,\mathrm{eV}$. Therefore, the linear relation is valid only when the inequality $|E(\overrightarrow{k})| \ll |\gamma_0|$ is satisfied (this is true for the experimental work described in this thesis). Then, the dispersion relation reads

$$E(\overrightarrow{k}) = \pm\hbar v_F |\overrightarrow{k}|. \tag{1.9}$$

Here v_F is a constant group velocity (Fermi velocity), which was experimentally found

to be $\sim 10^6$ m/s [5]. Eq. 1.9 implies that there are excitations with positive and negative energies. In the following sections low-energy excitations with positive (negative) energies will be called electrons (holes). In Fig. 1.4 the low-energy linear dispersion relation for graphene is shown. There are conduction and valence bands which intersect at the K point. The crossing point is also called the Dirac point.

It is interesting to note that the applicability of the Eq. 1.9 is also limited from the bottom, $E(\overrightarrow{k}) \gg E_0$, due to reduced screening at low carrier densities [6]. Below E_0 the energy spectrum is no longer linear, leading to an energy dependent Fermi velocity.

To derive an effective low energy Hamiltonian, one needs to expand the Hamiltonian from Eq. 1.4 in the vicinity of the K and K′ points. Their coordinates in $\overrightarrow{k}$-space are

$$\overrightarrow{K} = (\frac{4\pi}{3a}, 0) \quad \overrightarrow{K'} = (-\frac{4\pi}{3a}, 0). \tag{1.10}$$

Therefore, after the substitution $(k_x, k_y) \rightarrow (k_x \pm \frac{4\pi}{3a}, k_y)$ the Hamiltonian takes the form

$$H_{K,K'} = -\gamma_0 \frac{\sqrt{3}}{2} a \begin{pmatrix} 0 & \pm k_x - \imath k_y \\ \pm k_x + \imath k_y & 0 \end{pmatrix}. \tag{1.11}$$

One can rewrite this as follows

$$H_K = \upsilon_F \overrightarrow{\sigma}\overrightarrow{p} \qquad H_{K'} = \upsilon_F \overrightarrow{\sigma}'\overrightarrow{p}, \tag{1.12}$$

where $\overrightarrow{\sigma} = (\sigma_x, \sigma_y)$ and $\overrightarrow{\sigma}' = (-\sigma_x, \sigma_y)$ are vectors composed of Pauli matrices $\sigma_{x,y}$, and Fermi velocity $\upsilon_F = \sqrt{3}|\gamma_0|a/(2\hbar)$.

Finally, the Hamiltonian for low energy excitations in graphene has been deduced. Wave functions Ψ_K and $\Psi_{K'}$ should satisfy the equation

$$H_K \Psi_K = E(\overrightarrow{k})\Psi_K, \qquad H_{K'}\Psi_{K'} = E(\overrightarrow{k})\Psi_{K'}, \tag{1.13}$$

which are Dirac equations for a massless particle (Dirac-Weyl equation). The solutions of these equations are two-component spinors. In the non-relativistic Dirac equation, the operator σ plays the role of a spin operator, whereas for graphene massless particles σ is assigned to a different concept called pseudospin.

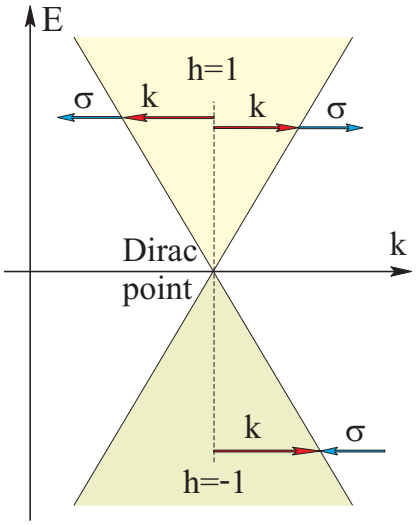

Figure 1.4: Helicity of the carriers in graphene.

To understand the meaning of pseupospin let us introduce the helicity operator

$$h = \frac{1}{2}\overrightarrow{\sigma}\frac{\overrightarrow{p}}{|\overrightarrow{p}|}, \tag{1.14}$$

which for photons gives the projection of the spin $\overrightarrow{\sigma}$ along the momentum $\overrightarrow{p}$. One can easily see that the eigenfunctions of the graphene Hamiltonian are eigenfunctions of the helicity operator. Therefore, helicity or so called chirality is a good quantum number for eigenstates near the K and K′ points, where Eq. 1.11 is valid. This means that the direction of pseudospin either coincides or counter coincides with the direction of $\overrightarrow{p}$, Fig. 1.4. It is worth noting that the concept of pseudospin arises due to the presence of two inequivalent sublattices in graphene, and, therefore, is not a spin, which was not introduced in our derivations.

Chirality in graphene plays an important role in understanding the behaviour of the carriers in this material. For example, the backscattering in graphene is largely suppressed [7, 8]. The chirality is an eigenvalue of the Hamiltonian and has to be preserved, while the scattering backwards implies a change of its sign.

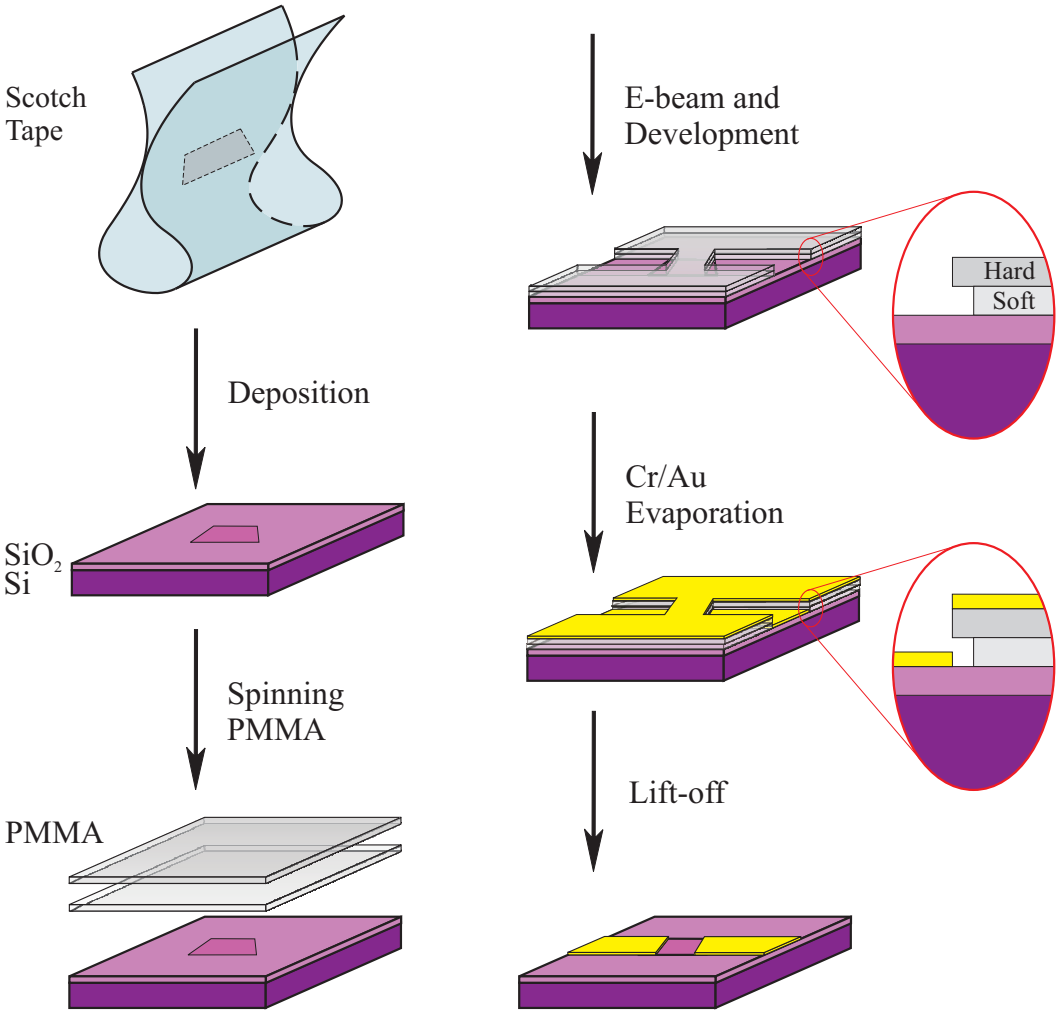

Figure 1.5: Fabrication process of a standard graphene device

1.2 Sample fabrication and measurement techniques

1.2.1 Graphene fabrication

Although the first graphene device was made in 2004 [9], the method of fabrication for the best quality graphene still remains the same. It starts with a cleavage of graphite using scotch tape. This technique of obtaining thin films of layered material has been known for a long time, but in the case of graphene it is used to produce a one atom thick layer of carbon atoms. A small piece of graphite is placed on one side of the tape, then two sides of the tape are stuck together and unstuck, peeling off the graphite piece into two pieces. After repeating this procedure for several times one can obtain monolayers of graphene at some regions of the tape. The part of the tape which is assumed to have the thinnest flakes is pressed onto a precleaned substrate, Fig. 1.5.

The most common material for the substrate is silicon. It consists of two layers, Fig. 1.5. The bottom layer is heavily doped Si which is used as a gate and, therefore, it needs to be conductive. The top layer is SiO_2, which serves as a dielectric separating the graphene and the gate. These substrates were used for most of the samples described in this work, although SiO_2 is known to be a material of a poor quality for producing graphene devices on top of it. First of all, it contains a significant amount of charged impurities near the top surface which causes substantial scattering of carriers in graphene [10]. Second of all, SiO_2 is grown thermally and its surface is not atomically flat. This results in ripples and also leads to additional scattering (see section 1.3.2).

In order to improve the quality of the devices, many different materials were tried as a dielectric [11]. Boron nitride, BN, was found to have the best characteristics. It is a layered material and can also be cleaved to a thin flake. BN has much less contamination and fewer defects than SiO_2 and is atomically flat. The highest mobility samples nowadays are produced using this material as an interlayer between graphene and SiO_2 [12, 13].

After deposition of graphene on the substrate, an optical microscope is used to search for monolayers, bilayers or multilayers, depending on the device required. Graphene is seen optically on Si/SiO_2 due to a Fabry−Perot cavity formed by the transparent SiO_2, reflecting Si and partially reflecting graphene flake. The measured optical contrast of monolayer C_1 under our experimental conditions is approximately 6 percent* [14]. The contrast depends linearly on the number of layers, N_l, provided this number is small, therefore, $C_{N_l} \simeq N_l C_1$. Thus, it is possible to optically distinguish between flakes with different thicknesses. However, because of the large error in contrast measurements for $N_l \geq 2$ the ranges of contrast values for two successive thicknesses intersect. This makes the optical method of determining the number of layers unreliable and gives only approximate numbers which need to be confirmed by more complex techniques [15–17].

When the flake is located on the substrate it is covered with two layers of polymethyl methacrylate (PMMA) of different molecular mass, Fig. 1.5. PMMA is a positive electron resist, which is used for patterning marks and metal contacts to the flake

*C_1 is defined as a ratio $(I_1 - I_2)/I_1$, where I_1 and I_2 are the intensities of the light reflected from the substrate and from the flake, respectively.

by means of e-beam lithography. $\sim 100\,\text{nm}$ of harder PMMA (with higher molecular mass) go on top of $\sim 200\,\text{nm}$ of the soft one. The necessity to have two layers of PMMA will be explained later. The set of marks (crosses) is exposed by the electron beam in PMMA. After development the crosses become visible in the e-beam system as holes in PMMA and form a coordinate system. Using these marks for determining the exact position of the flake and for alignment of the electron beam, the pattern of the contacts is exposed. After second development the regions where the contacts should be are open, while the rest of the substrate is still covered with PMMA. Under the same dose of exposure, hard PMMA is less soluble in the developer than soft PMMA. This leads to an undercut profile which prevents an overlap between metal films evaporated on the substrate (contacts) and on adjacent PMMA. Cr/Au contacts are used since Cr provides a better adhesion to graphene and Au is a good inert conductor. Thicknesses of the metal films are typically 10 nm and 10 nm for Cr and Au, respectively. After lift-off in acetone the metals with PMMA are removed except for the contact regions, Fig. 1.5. Electron-beam lithography used for our samples has a resolution of ~ 50 nm which allows to make several contacts to micron-sized flakes (typical sizes of the flakes used in this work were about $10\,\mu$m in both directions). As a result one obtains a contacted graphene flake on top of the chip, which is then mounted inside a chip carrier, convenient for putting it into the measuring stations and probes.

1.2.2 Typical $R(V_G)$ dependence

In the case of 4-terminal geometry the measurement setup is shown in Fig. 1.6(a). A ballast resistor, R_B, provides a constant current regime since the sample resistance, R, is much smaller than R_B (Typically, pure graphene gives $\sim 1\,\text{kOhm}$ per square and, therefore, a 10 MOhm resistor can be used as a ballast). The current flows between source and drain electrodes. A lock-in amplifier measures the voltage drop between the potential contacts, which is simply proportional to the resistance of the measured part of the flake. The 4-terminal scheme is employed to exclude the contact resistance which occurs near the interface between the graphene and metal (Cr). In etched devices, where the potential probes are made from graphene itself, contribution from contact resistance is negligible, whereas in those contacted directly by Au/Cr this contribution is finite and depends on the gate voltage [18].

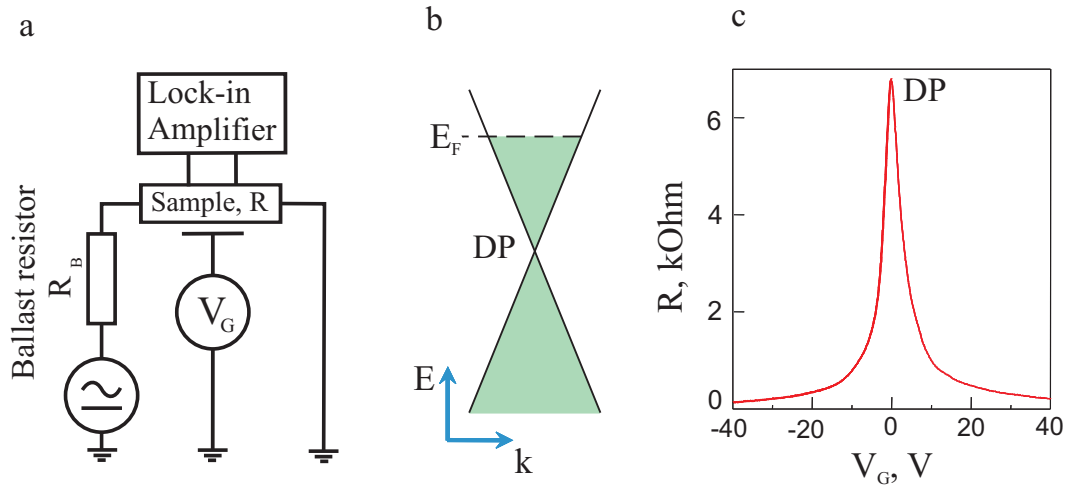

Figure 1.6: (a) Experimental setup. (b) Fermi level E_F changing with applied gate voltage V_G. The position of the Dirac point (DP) is indicated. (c) Dependence of resistance of typical graphene monolayer on V_G.

Gate voltage, V_G, is used to control the concentration of carriers in graphene. The gate and flake form two plates of a capacitor. Therefore, by applying a voltage difference, V_G, between them, the additional carrier concentration is induced in both Si and graphene. In Fig. 1.6(b) the concentration of carriers is schematically shown as filled states up to the Fermi level, which moves up (down) when V_G increases (decreases). At $V_G = 0$ V the Fermi level of clean graphene lies exactly at the Dirac point. Knowing the capacitance between gate and flake (i.e. thickness and permittivity of SiO_2 is known) and the graphene density of states, one can derive the relations $n = V_G \cdot 7.2 \cdot 10^{14}\,\mathrm{m^{-2}V^{-1}}$ [9] and $E_F = sign(V_G)31\sqrt{|V_G|}$ meV/V$^{1/2}$ [19]. A typical dependence of the resistance of a graphene monolayer on V_G is plotted in Fig. 1.6(c). The resistance curve experiences a maximum when the Fermi level crosses the Dirac point. At this point the concentration of carriers is nominally zero, although due to a nonuniform distribution of potential in the flake there are always regions of opposite potential. These regions have nonzero local concentration and form a percolation network which has a finite conductance [20, 21].

1.2.3 PMMA-free samples

After the fabrication process there are a significant number of contaminants left on the sample surface. Measurements of the sample resistance show that freshly prepared

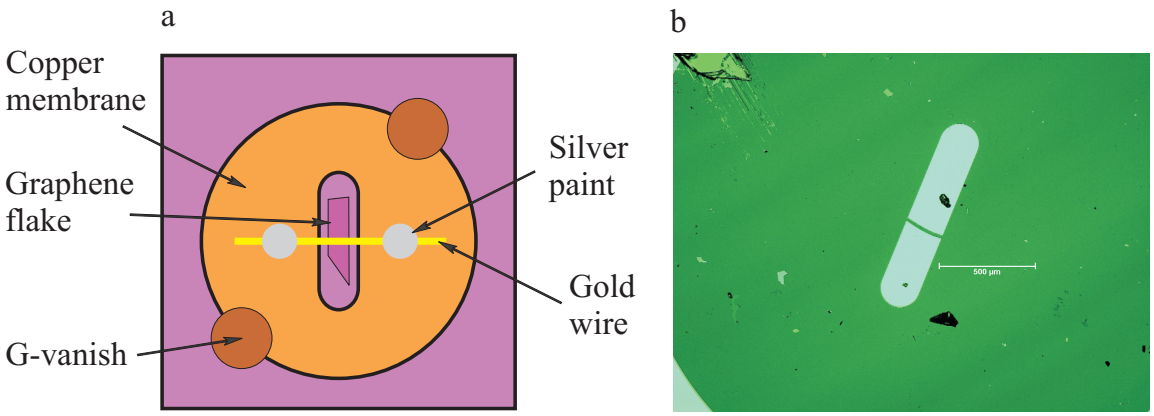

Figure 1.7: (a) The shadow mask glued on top of the substrate with a graphene flake. (b) Photo of the sample after evaporation of contacts and with the mask removed.

graphene devices are usually doped*. One of the sources of these contaminations is PMMA, and in order to avoid it a method of producing PMMA-free samples has been developed.

To exclude the lithography step, which requires PMMA, a shadow mask for evaporation of the metal contacts was employed. The mask is made from a copper membrane and an 18 μm thick gold wire, Fig. 1.7. The membrane has a 0.2 mm by 1 mm slot in the centre. The gold wire is placed across the slot and fixed on both sides with a silver conductive paint† [22]. The wire divides the slot into two regions with an 18 μm distance between them. Under the optical microscope the membrane is placed on top of the substrate so that the wire is above the graphene flake and divides it into two halves. When the membrane is in its required position, it is glued by GE-varnish [23]. It dries very slowly which allows correction of the position of the membrane in case of any unexpected movement. Finally, one obtains a flake on the substrate with the mask aligned such that the gold wire crosses the flake and is ~ 0.5 mm (thickness of the membrane) above it. Since the contacts are evaporated from two different metal sources, inaccurate alignment of the sources with respect to the sample can cause a shadow effect. To minimise this effect the wire is bent over the edge of the slot in order to make it as close to the flake as possible. After evaporation the mask is removed and the sample has two large contacts, Fig. 1.7.

Experimentally, PMMA-free samples did not show, on average, any increase of the mobility in comparison to usual devices made by lithography, which means that the

*The doping is seen as a shift of the Dirac point from $V_G = 0$ V.
†Any type of quick-drying glue can be used.

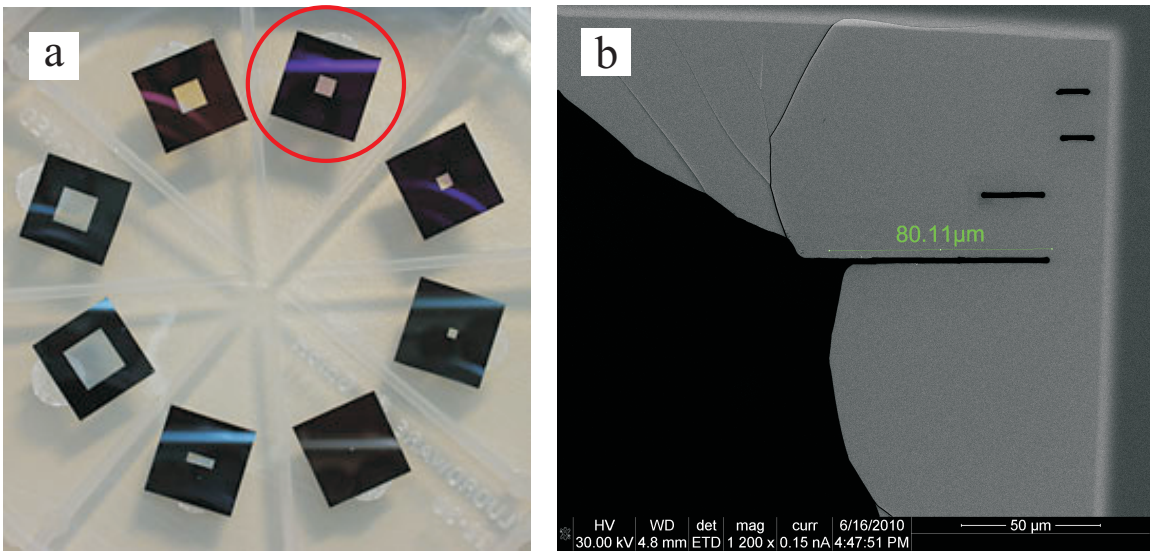

Figure 1.8: (a) Photo of the selection of commercially available Si_3N_4 membranes. The type of the membrane used in this work is highlighted. Taken from [24]. (b) SEM image of cracked Si_3N_4 membranes. Small slots do not cause the breakage, although if the size of the slot is above ~ 70 μm the membrane cracks.

PMMA residues give a negligible contribution to the scattering in this graphene. Also, this method can only be used to produce two-terminal devices. Masks for multiterminal devices (of micron size) cannot be made by hand and require equipment with high patterning resolution. For example, one can use a Focused Ion Beam system (FIB), as was done in this work, where it is possible both to obtain the high resolution (less than 100 nm) and to mill slots in thin membrane-like materials. Si_3N_4 windows on top of a Si frame, which are commercially available in different sizes [24], were used as an initial material for producing the membranes, Fig. 1.8(a).

During the milling the ion beam heats the surface of the target and knocks out the atoms of the target material. In addition to this, some of the ions pass on charge to the target. This charge accumulates with time and causes damage to the membrane, since the membranes are rather fragile. To minimise this effect 20 nm of metal (Cr/Au) is evaporated on both sides of the membrane. After optimisation of the parameters (ion current, shape of the hole) this technique was found to be quite robust if the size of the milling pattern does not exceed a certain limit. For example, a 70 μm by 2 μm hole (the first contact) was successfully milled in the membrane, although the membrane cracked during an attempt to enlarge the slot, Fig. 1.8(b). The damage can be caused by two reasons: firstly, accumulation of the charge in the membrane can still be significant,

since most of the time the ion beam heats uncovered inner material; secondly, the holes in the Si_3N_4 can cause an additional stress in the membrane, which result in its breakage. So far, all the membranes with slots exceeding 70 μm were damaged by the ion beam and the outcome of this technique is zero, and it is quite likely that Si_3N_4 is a too fragile material for the milling process (although this technique is successfully used for the slots of a smaller size).

1.3 Scattering

1.3.1 Introduction

In this section the basic mechanisms of scattering of carriers in graphene will be overviewed. These mechanisms affect electronic transport and are seen experimentally in resistance and $1/f$ noise measurements. Theoretical models of different types of scattering behaviour will be discussed and illustrated with recent experiments which agree or disagree with theoretical predictions.

1.3.2 Scattering mechanisms

Analytically, the conductance of graphene can be derived using the Boltzman equation written for the deviation of the distribution function from its value in zero external field [3]. Using the relaxation time approximation and keeping only linear terms in the external field, one can find the conductivity, σ, to be

$$\sigma = \frac{e^2 v_F^2}{2} \int D(E)\tau(E) \left(-\frac{\partial f(E)}{\partial E}\right) dE, \tag{1.15}$$

where $\tau(E)$ is a relaxation time of carriers for a particular scattering mechanism. Density of states, $D(E)$, dispersion relation, $E(\overrightarrow{k})$, and distribution function, $f(E)$, are given by relations

$$D(E) = \frac{4|E|}{2\pi\hbar^2 v_F^2}, \quad E = \hbar v_F |\overrightarrow{k}|, \quad f = 1/\left(1 + \exp\left(\frac{E - E_F}{k_B T}\right)\right).$$

At low temperatures, when $T \ll E_F$, $\partial f(E)/\partial E$ is practically a delta function with a non-zero value at $E = E_F$, which allows one to derive an explicit formula

$$\sigma = \frac{e^2 \upsilon_F^2}{2} D(E_F)\tau(E_F). \tag{1.16}$$

As seen from Eq. 1.16, the conductivity is determined by $D(E_F)$ and $\tau(E_F)$. When $D(E_F)$ is determined by the band structure of graphene only, $\tau(E_F)$ is given by a particular type of carrier scatterers and their distribution on the graphene surface.

In reality there are always several types of impurity near the conductive channel. In order to take into account all contributions one can use Matthiessen's rule, which allows the summation of resistivities (which are simply proportional to the scattering probabilities) determined by the different scattering mechanisms. The conductivity reads*

$$\sigma^{-1} = \sigma_{lrs}^{-1} + \sigma_{srs}^{-1} + \sigma_{mgs}^{-1} + \sigma_{ph}^{-1} + \sigma_{scorr}^{-1}. \tag{1.17}$$

The subscripts in this expression denote contributions from long-range scatterers, lrs, short-range scatterers, srs, midgap states, mgs, phonons, ph, and surface corrugations, $scorr$. The type of dominant contribution varies from sample to sample due to both variety and irreproducibility of fabrication techniques.

Long-range scattering (which, for example, comes from the Coulomb potential) is believed to be a significant source of scattering in supported graphene. One of the origins of this type of potential is charged impurities in the SiO_2 [10]. Moreover, during the fabrication process graphene can be immersed into different chemicals or covered by polymers and at some stages is open to the atmosphere, which also introduce charged contaminations on the surface.

The contribution to the conductance from long-range scatterers is calculated using Eq. 1.16, where in the case of unscreened Coulomb potential τ has the form $\tau_{lrs}(\overrightarrow{k}) = \upsilon_F/u_0^2|\overrightarrow{k}|$ [26], where u_0 is the strength of the scattering potential proportional to the concentration of impurities ($u_0^2 \sim n_{lrs}$). Therefore, the conductivity reads

$$\sigma_{lrs} = \frac{e^2 \upsilon_F^2}{\pi \hbar u_0^2} k_F^2 \sim n, \tag{1.18}$$

*Different contributions to the scattering were discussed in a similar way in Ref. [25].

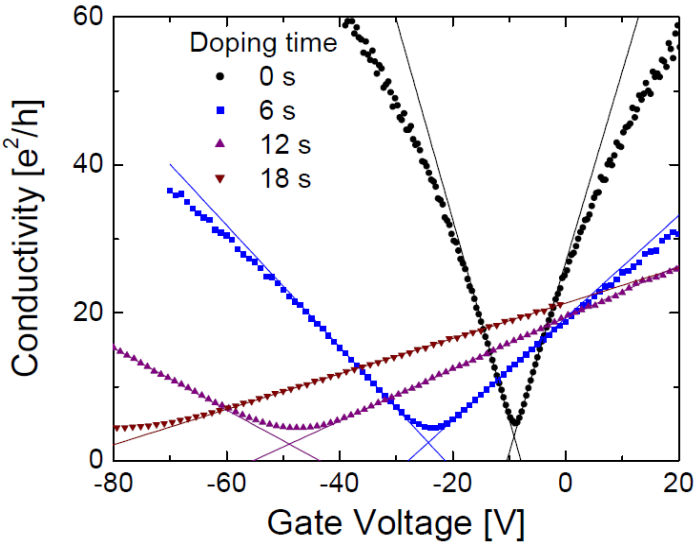

Figure 1.9: Dependence of the graphene conductivity on the gate voltage. Different curves represent different doses of doping with increasing doping from the right curve to the left. Adopted from [25].

where n is the carrier concentration and the relation between n and k can be obtained by taking the integral

$$n = \int_0^{E_F} D(E)dE = \frac{E_F^2}{\pi\hbar^2 \upsilon_F^2} = \frac{k_F^2}{\pi}. \tag{1.19}$$

Screening of the Coulomb potential by carriers increases conductance in the whole range of n, although it does not change the linear relation between σ and n [27]. It is interesting to note that screening effects depend on the temperature and can contribute to the temperature dependence of graphene conductance.

Experimentally the effect of charged impurities on the transport properties was shown in Ref. [25]. Different amounts of potassium atoms were deposited onto the graphene surface and the $\sigma(V_G)$ dependence was measured at each level of contamination, Fig. 1.9. Near the graphene surface a potassium atom donates an electron into the channel and becomes a positively charged impurity. As seen in the figure there is a range of V_G where $\sigma(V_G)$ is linear and the slope of the dependence decreases with increasing concentration of potassium, which indicates an increase of the strength of the scattering potential.

The relaxation time for short-range scattering potential has a form $\tau_{srs} = 4\upsilon_F/(n_{srs}v_0|\overrightarrow{k}|)$, where v_0 is the scattering potential strength and n_{srs} is the con-

centration of impurities [28]. The conductivity

$$\sigma_{srs} = \frac{4e^2 \upsilon_F^2}{\pi \hbar n_{srs} \upsilon_0}, \tag{1.20}$$

therefore, the short-range scattering potential results in a contribution to the resistance independent of the carrier density. In spite of the fact that all experiments show graphene conductance dependent on concentration, the signature of short-range impurities is still present. For example, the black curve in Fig. 1.9 represents $\sigma(V_G)$ dependence before doping. One can see that the conductance deviates from its linear dependence starting from $\sim 10\,\mathrm{V}$ from the Dirac point. This sublinear behaviour is usually assigned to the presence of a constant contribution in Eq. 1.17. Also, the short-range potential has the form of a delta function and can change the wave vector of the carrier by $2\overrightarrow{K}$ (where $\overrightarrow{K}$ is a wave vector of the K point) during the scattering event and thereby cause intervalley scattering (scattering between K and K' valleys). Presence of such scattering is seen in samples with a high level of disorder by Raman spectroscopy [17] and by weak localization measurements [29]. Physically, short-range impurities can be neutral contaminations close to the conductive channel, or lattice defects in the graphene structure.

Another type of scatterer which can lead to a close to linear dependence of σ on n is resonant scatterers. The energy level of these impurities coincides with the Fermi level of the Dirac fermions and can cause resonant scattering. For the case where these resonant states lie exactly at the crossing point between the conductance and valence bands (that is why they are also called midgap states) conductance has the form [30]

$$\sigma_{mgs} = \frac{4e^2}{h} \frac{n \ln^2(k_F R)}{n_{mgs}}. \tag{1.21}$$

Here n_{mgs} is the concentration of impurities and R is the effective radius of the scatterer. In Ref. [31] the midgap states were suggested to be the dominant scatterers in supported graphene.

Linear conductivity can also result from scattering of carriers on the roughness of the graphene surface [32]. Graphene is nominally a flat material, although in reality there are always reasons for it to form surface corrugations, also called ripples. Supported graphene lies on the rough surface of the substrate, whereas in suspended graphene

there is always some inhomogeneous tension causing wrinkles. Random movements of the graphene sheet introduce ripples, similar to the long-range scatterers. For this type of ripples the conductivity reads $\sigma_{scorr1} = C_{scorr1}(n/n_{scorr1})$, where C_{scorr1} is a constant and n_{scorr1} is an effective concentration of ripples. Another type of ripples introduced from the substrate results in conductance of the form $\sigma_{scorr2} \sim \ln^2(k_F a)$ (a is the distance between carbon atoms). This behaviour is similar to the one caused by a short-range potential since the logarithmic dependence is practically a constant for the typical range of concentrations used in transport experiments.

The last type of scatterers that will be discussed here is phonons. Phonon scattering is independent of n, but gives a major contribution to the temperature-dependent part of resistance (or inverse conductance). Phonons are divided into acoustic and optical modes. Acoustic phonons are expected to give a linear dependence of resistivity on the temperature [25]

$$\sigma_{ph}^{-1} = \left(\frac{h}{e^2}\right) \frac{\pi^2 D_A^2 k_B T}{2h^2 \rho_s \nu_S \nu_F}. \tag{1.22}$$

Here ρ_s is the 2D mass density of graphene, ν_s and ν_F are the sound and Fermi velocities in graphene and D_A is the acoustic deformation potential. At room temperature (and below) scattering from optical phonons is negligible and will not be considered. There are also flexural phonons that give a quadratic in temperature contribution to the graphene resistivity and are believed to be the dominant scatterers in suspended samples [33].

1.4 Noise

Noise, according to the most general definition, is the fluctuation of any physical quantity from its average value. In this thesis only electrical noise will be considered (i.e. the fluctuations in voltage, current or resistance). Usually one measures only an average value of the signal $\overline{V(t)}$, although the time dependence $V(t)$ can give additional information about the origin of the signal and reveal physical processes hidden within the averaged value. It is convenient to study the time dependence in terms of frequency, f, since the majority of the local processes have their particular characteristic frequencies. Therefore, the noise power spectral density, $S_V(f)$, is introduced as a quantity which

is defined by the strength of the fluctuations at a particular frequency f and is given by the integral

$$S_V(f) = 2\int_{-\infty}^{+\infty} C_V(\tau)\exp(\imath 2\pi f\tau)d\tau, \tag{1.23}$$

where $C_V(\tau)$ is the signal autocorrelation function defined as

$$C_V(\tau) = \overline{V(\tau)V(0)} - \overline{V(0)}^2 = \lim_{T\to\infty}\frac{1}{T}\int_{-T/2}^{T/2}(V(\tau) - \overline{V(0)})(V(0) - \overline{V(0)})d\tau. \tag{1.24}$$

Several types of noise are identified based on the origin of fluctuations and on the character of the frequency dependence of $S(f)$.

1.4.1 Thermal noise

Thermal noise (or Johnson-Nyquist noise) is present in all resistors regardless of any applied voltages and results from thermal fluctuations - random thermal motions of charge carriers. Thermal noise is the lowest possible level of noise in the system and it cannot be reduced by any method other than by decreasing the temperature. This type of noise can be measured as voltage fluctuations across the resistor R. Theoretical prediction for $S_V(f)$ reads

$$S_V(f) = 4k_BTR. \tag{1.25}$$

Here k_B is the Boltzmann constant and T is the temperature of the resistor, R. As seen from Eq. 1.25 thermal noise depends only on the product TR and, therefore can be used for determining the temperature of the resistor, provided that the resistance is known.

1.4.2 Random telegraph noise

Quite often an electronic system does not stay in one equilibrium state but instead switches between several states with close total energies. Let us assume, that there are two such states and the system randomly jumps between them due to temperature fluctuations. Some physical parameters, for example resistance, can depend on the state and, therefore, one can observe experimentally random transitions of the system between two states with different resistances. This kind of noise is called random telegraph noise (RTN) or burst noise.

RTN is seen in MOSFET structures. The active volume in these devices is very small and local fluctuations of potential can cause a significant fluctuations of the resistance. For example, in the vicinity of the conducting channel there is always a finite number of impurities. Some of them usually have energy levels close to the Fermi level in the system, thus, a conductive electron can jump from the conductive channel to the impurity state with probability p_1. If the current in the channel is carried by a small number of electrons, the device resistance will change significantly when the number of carriers is changed by unity. This implies that RTN is seen only when current flows through the device. While occupying the impurity state the electron has a probability p_2 to jump back. This switching is completely random and has the power spectral density of the form

$$S_{RTN}(f) = (R_1 - R_2)^2 p_1 p_2 \frac{4\tau}{1 + (2\pi f\tau)^2}, \tag{1.26}$$

where R_1 and R_2 are the resistances of the device in states 1 and 2, respectively, and τ is a characteristic relaxation time of the random process. This is equal to an average time the system spends in a state between two successive transitions. Eq. 1.26 is plotted as a function of f in Fig. 1.10.

1.4.3 $1/f$ noise

An impurity described in subsection 1.4.2 has its own characteristic relaxation time, τ. For the case where there are many impurities in the vicinity of the conductive channel, it is convenient to describe them using the distribution function of their relaxation times, $D(\tau)$. In MOSFET systems, where impurities are located at various distances, z, in a dielectric, and electrons tunnel between impurity states and channel, the τ distribution can be rewritten as a function of z: $D(\tau)d\tau = D(\tau(z))(d\tau/dz)dz = D_z(z)dz$. Since all the impurities contribute to the overall fluctuations of resistance, the spectral power density of these fluctuations is

$$S(f) = \int_{\tau_1}^{\tau_2} D(\tau) S_{RTN}(\tau) d\tau \propto \int_{\tau_1}^{\tau_2} D(\tau) \frac{\tau}{1 + (2\pi f\tau)^2} d\tau. \tag{1.27}$$

As seen from Eq. 1.27, the resulting dependence of $S(f)$ on frequency is determined by $D(\tau)$. As an example, let us assume that $D(\tau) \propto 1/\tau$ (an example of such distribution

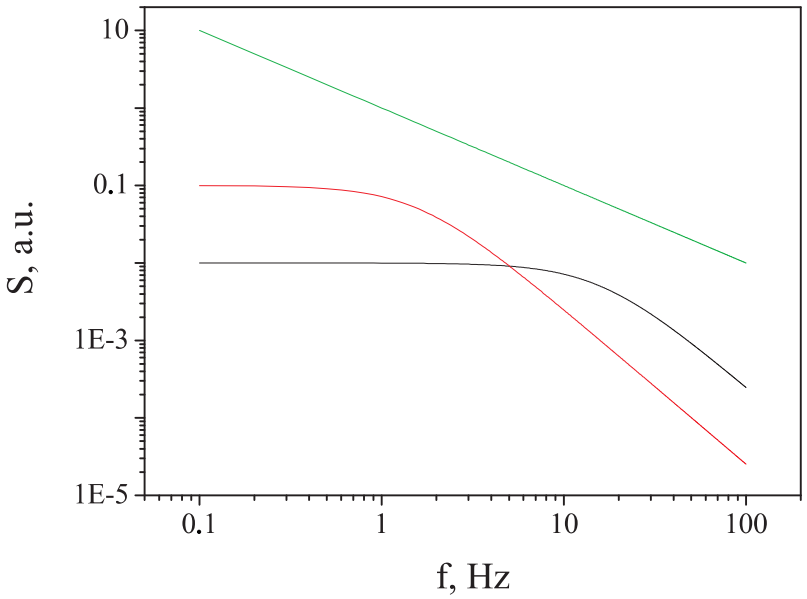

Figure 1.10: Power spectral density, S, as a function of frequency for RTN ($\tau =$ 0.01 seconds for the black curve and $\tau = 0.1$ seconds for the red curve) and $1/f$ noise (green curve).

is given in Ref. [34]), then the integral in Eq. 1.27 can be analytically taken, and for $1/\tau_2 \ll f \ll 1/\tau_1$

$$S(f) \propto \frac{1}{f}\left(\arctan(2\pi\tau_2 f) - \arctan(2\pi\tau_1 f)\right) \simeq \frac{\pi}{2f}. \tag{1.28}$$

Thus, in a range of frequencies determined by τ_1 and τ_2 the noise power spectral density is inversely proportional to f and is an example of so-called $1/f$ noise, or flicker noise.

$1/f$ noise is present in many electronic systems. Generally, if the noise scales with f as $1/f^{\alpha}$, where α is close to unity, it is called $1/f$ noise, Fig. 1.10. Its origin varies from system to system and its presence can be explained by many physically different mechanisms. For the example given above, the noise results from tunneling events between the impurities and conductive channel, but the required distribution of relaxation times can also be obtained from absorption-desorption processes of different molecules on the sample surface, from tunneling of electrons between impurities, or from slow thermally activated fluctuations of the sample structure (flexural phonons in graphene). Studies of the $1/f$ noise in graphene will be discussed in Chapter 3.

Chapter 2

Electrochemical doping of graphene

2.1 Introduction

Doping by the addition of impurities is a very common procedure in the semiconductor industry, where it is used to modulate the electronic properties of the initial material. It introduces empty or occupied electron states into the energy gap in the band structure, changing the number of carriers in either conductance (electrons) or valence (holes) bands.

Doping of graphene is also widely used nowadays for different purposes. Firstly, dopants (impurities which either donate or accept electrons) form a corresponding scattering potential, Section 1.3.2. Studying this potential can clarify the scattering mechanism limiting mobility of carriers in graphene devices. For example, it was shown that introducing the potassium atoms on the graphene surface (molecular doping) causes the long-range scattering seen as a linear dependence of the conductivity on the carrier concentration [25]. Secondly, creation of p-n barriers by local doping is an interesting subject not only for device applications, but it also provides an insight into the chiral nature of carriers in graphene. In Ref. [35] the conductance oscillations in extremely narrow graphene heterostructures revealed the signatures of the Klein tunneling effect [36]. Thirdly, graphene was shown to be a good candidate for sensing purposes. Sensitivity of graphene transistor to a single NO_2 molecule was reported in Ref. [37]. Several laboratories are working towards the functionalisation of graphene in order to produce a selective sensor of organic molecules. Electrolyte-gated graphene was demonstrated to be sensitive to a change in pH and a protein concentration in

the electrolyte [38]. However, the selective sensitivity of the graphene devices has not been achieved yet. Fourthly, ordered impurities on the graphene surface can lead to an opening of the gap in the graphene bandstructure as was suggested in Ref. [39].

In this chapter the interaction between graphene and benzene-based molecules will be addressed with the aim to understand the capability of graphene to be used for sensing of organic substances. The doping effect on graphene of water and such organic molecules as toluene ($C_6H_5CH_3$), naphthalene ($C_{10}H_8$), aniline ($C_6H_5NH_3$) and pyrene ($C_{16}H_{10}$) will be described in order to understand the importance of both the dipole moment of the dopants and their π-π interactions with graphene. It will be shown, that in the vicinity of graphene some molecules undergo electrochemical reactions, and, therefore, represent a new type of graphene dopant which was not described earlier.

2.2 Experimental setup

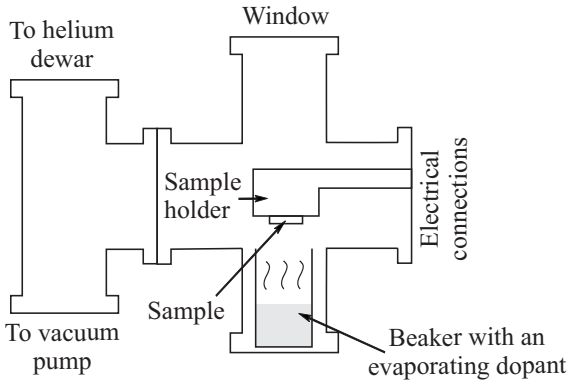

Figure 2.1: Experimental setup.

A special setup was designed to suit the needs of our experiment, Fig. 2.1. All the measurements were performed inside a sealed metal chamber connected to a vacuum pump and to a source of helium gas. This provided the controllability of the environment in the vicinity of the sample. The sample holder was placed in the middle of the chamber with its face down, and was thermally linked to a heater. This allowed the temperature of the sample to be changed up to $\sim 140\,^{\circ}\mathrm{C}$. The temperature was measured by a thermal resistor mounted inside the heater. During annealing the pressure in the chamber was kept below $\sim 10^{-4}\,\mathrm{mbar}$, which ensured an effective removal of contamination coming from the surface of the sample. Inert helium was employed as a background atmosphere containing the dopant vapour. The source of the dopant, glass

container with a liquid or solid substance, was introduced into the chamber through an open flange. In order to avoid contamination from the air, the transfer of the dopant into the chamber was done under the continuous flushing flow of helium. The dopant container was placed immediately under the sample holder.

2.3 The role of π-π interaction in the doping by organic molecules

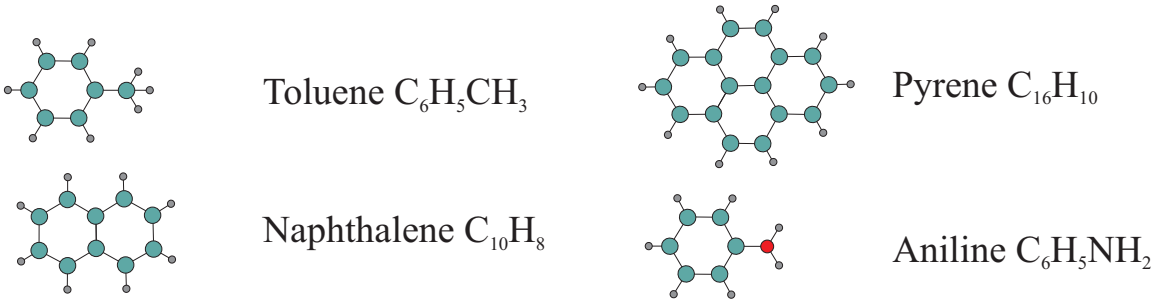

Figure 2.2: Organic molecules used in this work are shown schematically. Blue circles represent carbon atoms, grey circles - hydrogen atoms and red circle - a nitrogen atom.

In graphene the interaction between the π orbitals determines the band structure, Sec. 1.1.2. Moreover, in multilayer graphene (bilayer, trilayer, etc.) the π-π interaction between the layers results in the band structure different from that of the monolayer graphene [40]. Organic molecules studied in this work have a ring of carbon atoms in their structure, Fig. 2.2, - the base element of graphene. Therefore, it is reasonable to expect that the π-π interaction between graphene and organic molecules can potentially affect the electronic properties of graphene. For example, one can assume that an adsorbed benzene molecule would locally change the band structure and transform a monolayer into a "bilayer".

Molecules that have a carbon ring in their structure interact with each other by means of the π orbitals. For example, it was shown that benzene and toluene do not form isotropic liquids, but tend to assemble themselves into clusters due to the π-π interaction [41]. Also, an attractive force between a single pyrene molecule and HOPG graphite surface was directly measured in Ref. [42], which suggests that the same force should appear between graphene and a pyrene molecule (or any other benzene ring based molecule). However, even if such organic molecules are attracted to graphene

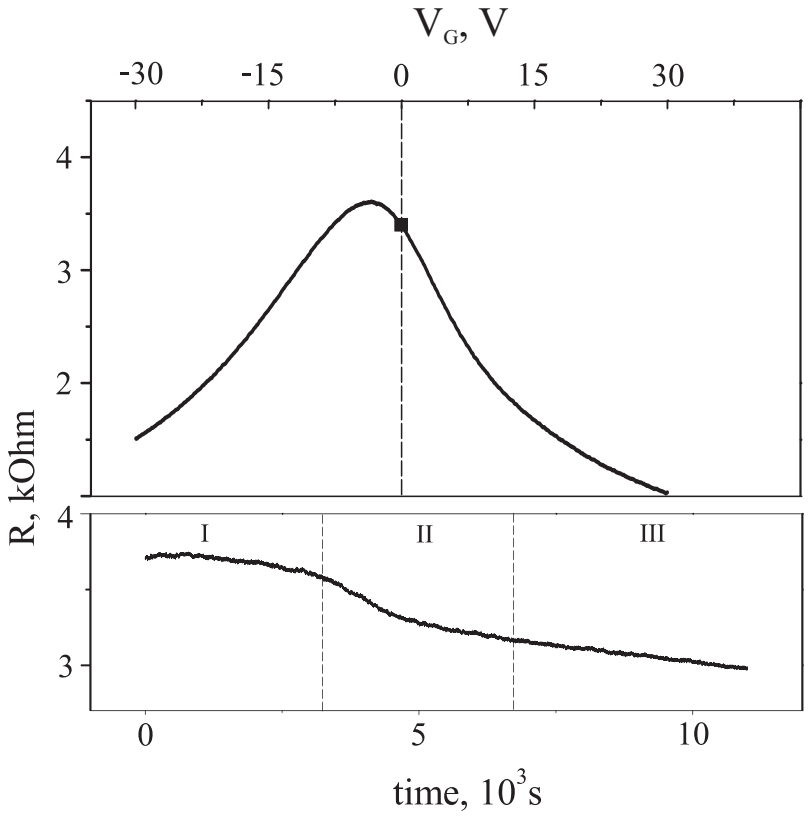

Figure 2.3: Top: resistance R of a typical graphene device (sample AG4D1) as a function of the gate voltage V_G. The starting point of measurements shown in the bottom panel is indicated. Bottom: change of the resistance as a function of time after adding toluene vapour with no applied gate voltage ($V_G = 0$). Three distinct time intervals are highlighted.

and adsorbed on its surface, it does not ensure that the electronic properties of graphene will be affected by this interaction.

To test the role of the π-π interaction, graphene was doped by toluene ($C_6H_5CH_3$), naphthalene ($C_{10}H_8$), aniline ($C_6H_5NH_3$) and pyrene ($C_{16}H_{10}$). 11 monolayer samples* were doped with these organic molecules (see Appendix A for sample statistics). The measurements were performed at room temperature in helium atmosphere at pressure $p \gtrsim 1\,\text{bar}$ (see Sec. 2.2 for details). Before doping, the samples were annealed in vacuum for ~ 1 hour at $T \simeq 140\,^\circ\text{C}$ to remove atmospheric water contamination. (The temperature of the annealing is chosen to be above the boiling temperature of the water. Time is chosen to be sufficient for saturation of the change in R during the annealing at given T.) After annealing, the chamber was filled with helium and the beaker with the dopant was placed in the chamber immediately under the downward

*All samples were verified to be monolayers by contrast measurements [43], which was checked for most of them by means of Raman spectroscopy [44].

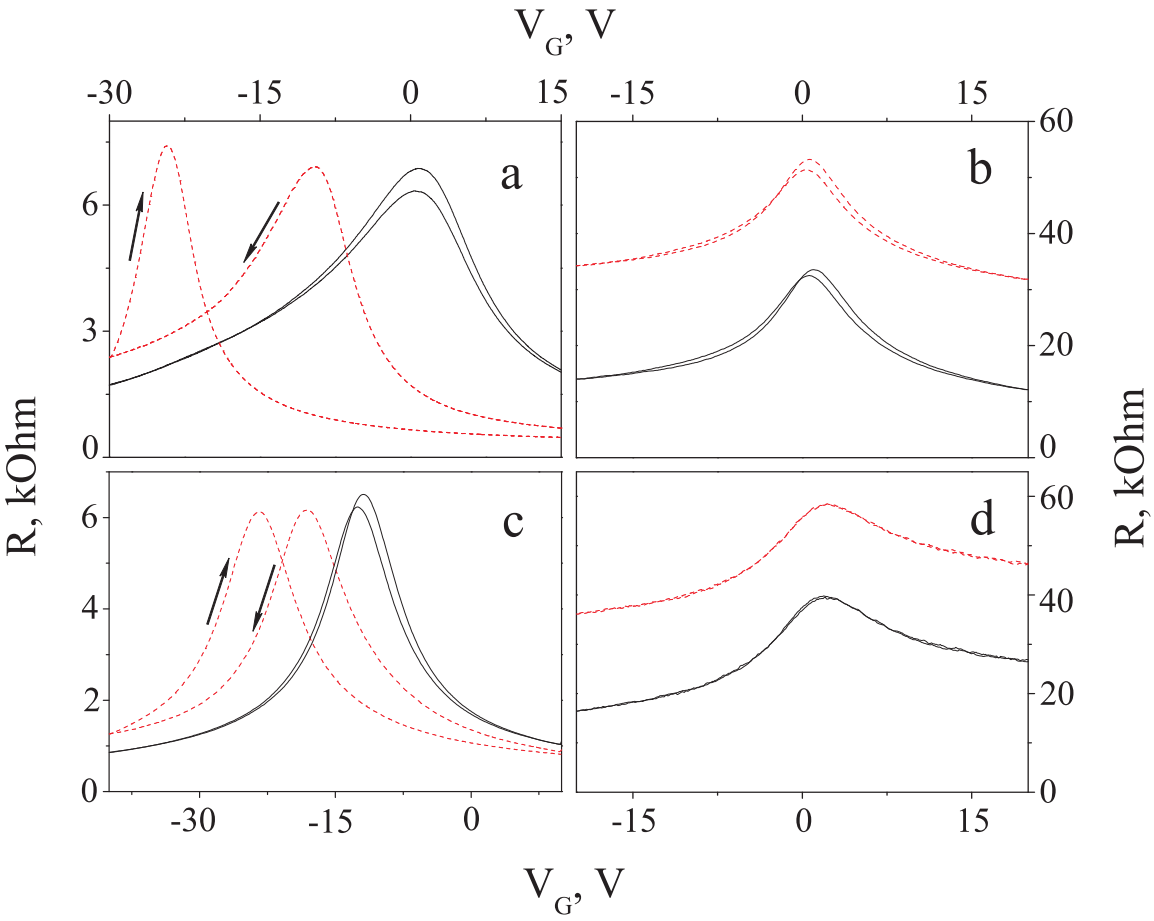

Figure 2.4: $R(V_G)$ dependence of graphene samples before and after doping by (a) toluene (sample AG1D1F1), (b) naphthalene (sample AG5D1), (c) aniline (sample AG4D4) and (d) pyrene (sample AG5D1). For each stage of the experiment two curves are shown indicating the hysteresis between different directions of changing gate voltage (direction is given by arrows). $R(V_G)$ dependences after doping are designated by dashed lines. In panels (b) and (d) curves for doped samples are offset up by 20 kOhm.

facing sample holder. Then, the time dependence of the sample resistance, R, at fixed back gate voltage, V_G, was measured during the exposure of the sample to the dopant vapour. $R(V_G)$ dependence was measured before and after exposure.

Figure 2.3 shows that the sample resistance changed significantly during the doping by toluene. It is known that the dopants can affect graphene in two ways*. They can either introduce scattering, which changes mobility of the carriers and, therefore, changes the resistance; or donate carriers (holes or electrons), which shifts the Dirac point with respect to its initial position, and, therefore, changes the resistance at any fixed V_G. In reality both effects take place, as seen from both our results and Ref. [25].

*The third possibility is that the dopants such as organic molecules can locally change the graphene band structure and, thus, change the density of states. This mechanism is not considered here as the coverage of the graphene by the molecules is assumed to be small, Sec. 2.5.6.

In Fig. 2.4(a) the resistance as a function of the gate voltage is shown before and after doping by toluene. Toluene exposure is seen to shift the resistance peak towards negative voltages, which clearly indicates the doping of graphene by electrons*. One can also note that the shape of the $R(V_G)$ peak is changed. This observation is complicated by the hysteretic behaviour of the sample. However, in general, the change of the shape of $R(V_G)$ curve indicates the change in the mobility of the carriers (or, in other words, change of the scattering potential in the sample) unrelated to the shift of the curve. The observed hysteresis after toluene doping will be discussed in Sec. 2.5.1.

Panels (b), (c) and (d) in Fig. 2.4 show $R(V_G)$ dependences before and after sample exposure to naphthalene, aniline and pyrene vapours, respectively. At normal conditions, aniline (as toluene) is a high volatility liquid, whereas naphthalene and pyrene are solid. One can assume that the sublimation of these solids cannot provide enough vapour to affect graphene. The vapour pressures under normal conditions of toluene, aniline, naphthalene and pyrene are 3.8 kPa, $\sim$ 90 Pa, $\sim$ 13 Pa and less than 1 $\sim$ mPa, respectively [45–47]. Vapour pressure of naphthalene is much smaller than that of aniline, therefore, in order to exclude the difference in the volatilities, the naphthalene effect was measured for a longer time period ($\sim$ 10 times longer) than aniline effect. The effect of pyrene was measured for the same amount of time as naphthalene effect, therefore, the absence of the doping by pyrene seen in the figure can be ascribed to its low volatility.

Aniline vapour was observed to dope graphene in a similar way to toluene, whereas naphthalene and pyrene were seen to have no effect. Since all the organic molecules, which have a carbon ring in its structure, are known to be attracted to the graphite surface [42], the selective sensitivity of graphene to these molecules rules out the π-π interaction as a mechanism affecting electronic properties of graphene. Thus, aniline and toluene dope graphene via a mechanism unrelated to π-π interaction, and naphthalene and pyrene do not affect the transport in graphene, although they most likely are adsorbed on its surface.

The doping effects of toluene and naphthalene were studied in detail on separate

*The maximum of $R(V_G)$ dependence indicates the position of the Dirac point, which is the only point where in average the carrier concentration in graphene is zero (neutrality point). Therefore, the shift of this point suggests that stronger negative gate voltages are required in order to reach the zero concentration. In turn, stronger negative potential on the gate implies higher initial concentration of electrons in graphene.

samples and were reproduced. The doping effects of aniline and pyrene were not the focus of our current study and, therefore, have not been studied carefully. The effect of pyrene was measured only on sample AG5D1 after the exposure of this sample to naphthalene. Therefore, the surface of it was most likely covered by naphthalene molecules before exposure to pyrene, which could crucially change the sensitivity of graphene to pyrene. However, the effect of toluene was noticeable on the same sample after it was covered by naphthalene (although the amplitude of the effect was reduced indicating decrease of the graphene sensitivity). Also, the doping by aniline was measured on two samples (AG5D1 and AG4D4) and only one of them (AG4D4) was found to be affected, Fig. 2.4(c). Insensitivity of sample AG5D1 to aniline can be explained by the fact that before treatment with aniline this sample was exposed to naphthalene and pyrene, whereas sample AG4D4 was not, and turned out to be clean enough to absorb aniline on its surface. This argument support the assumption that in spite of the low vapour pressure there is a significant amount of naphthalene molecules around the sample. Thus, performed measurements with aniline and pyrene are not reliable, however, they support our conclusions based on toluene and naphthalene studies.

2.4 The role of the dipole moment

In the previous section it was found that some organic molecules dope graphene (toluene, aniline) and others do not dope (naphthalene, pyrene). The π-π interaction was ruled out as a possible doping mechanism. Then, to understand the origin of graphene selectivity to organic molecules, let us point out the differences between these two groups of dopants. Toluene and aniline are benzene derivatives, where one of the hydrogen atoms is replaced by methyl group, CH_3, and phenyl group, NH_2, respectively. The presence of additional groups attached to the benzene ring leads to an asymmetry in the structure and, therefore, to a finite dipole moment. Dipole moments of toluene and aniline molecules are 0.36 D and 1.53 D, respectively [45]. Both naphthalene and pyrene have symmetric structure and have zero dipole moments.

Interaction between graphene and asymmetric organic molecules can be associated either with a finite dipole moment or with a chemical activity of methyl and phenyl groups. To explore these assumptions further the doping effect of water vapour was measured. The water molecule has a simple structure and does not contain any chem-

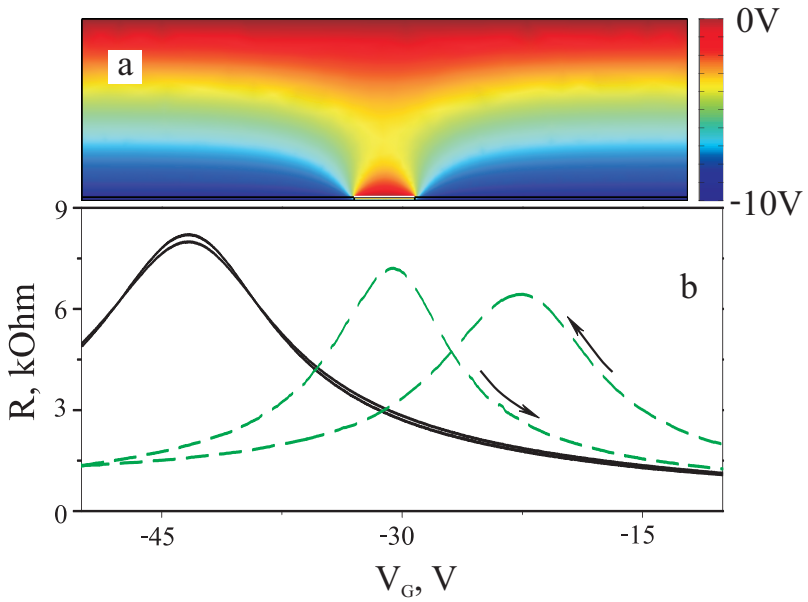

Figure 2.5: (a) Colour plot of the calculated distribution of the potential in the vicinity of the graphene flake (thick white line near the bottom) and doped silicon gate (bottom of the figure) with applied $V_G = -10\,\mathrm{V}$. The size of the box is $50\,\mu$m by $15\,\mu$m. The top boundary of the box is grounded. (b) Water doping effect measured on sample AG1D1F1. Dashed lines show hysteretic behaviour of the sample after doping. Arrows indicate the direction of changing V_G.

ically active organic groups (although water can be active by itself). Also, the dipole moment of water, 1.85 D, is higher than that of either toluene or aniline. Thus, if there is no effect of water on graphene one will be able to conclude that the dipole moment is irrelevant in the studied phenomenon.

The experimental procedure was exactly the same as for organic dopants. As a source of vapour, high purity water purchased from Sigma Aldrich was used (residues concentration $\lesssim 0.005\,\%$ [48]). Resistance as a function of gate voltage before and after water exposure is shown in Fig. 2.5(b). The shift of the resistance peak after doping is clearly seen. In spite of the fact that water appears to dope graphene with holes, not electrons, the character of the effect is similar to that of toluene. Both molecules cause the hysteresis of the same kind: the peak in $R(V_G)$ is shifted in the direction opposite to the direction of sweeping V_G. For example, during the measurement of the right hysteretic peak in Fig. 2.5(b), V_G was swept from positive to negative voltages (direction of sweeping is to the left), whereas this peak is shifted to the right with respect to the other hysteretic peak, i.e. towards positive V_G.

Similarities between doping effects of water, toluene and aniline suggest that the

finite dipole moment of the dopant plays an essential role. Dipole molecules are very sensitive to the surrounding electric field. In fact, an applied V_G creates a uniform electric field between the graphene flake and the gate. Furthermore, due to the geometry of the flake-gate capacitor, the electric field also extends above the flake. To estimate the strength of the "stray" fields we calculated the distribution of the potential near the sample*, Fig. 2.5(a). The field above the graphene within 100 nm distance was found to be ~ 15 times smaller then that under the graphene, which is strong enough to influence the reactivity of toluene molecule when, for example, $V_G = -10\,\mathrm{V}$ is applied [49]. Thus, experimentally observed doping effect on graphene of toluene, aniline and water (dipole molecules only) in addition to the fact that the graphene is indeed surrounded by "stray" field, suggests that the mechanism of doping by these molecules should be related to the interaction between their dipole moments and electric field created by the gate voltage.

2.5 Electrochemical doping

2.5.1 Timescale of the effect and hysteretic behavior.

It has been established that toluene changes the resistance of graphene and that this effect should be significantly influenced by the electric field present above the sample. However, during exposure to toluene the sample resistance changes even if there is no electric field in the system ($V_G = 0$), Fig. 2.3. This means that the interaction between graphene and dipolar dopants cannot be explained by electrostatic forces only.

To study the doping effect by toluene in more detail let us go back to Fig. 2.3. It is seen, first of all, that toluene changes the resistance and the timescale of the effect is hours. Second of all, three distinct intervals in time dependence can be distinguished. Over the first interval, $t_I \simeq 10^3\,\mathrm{sec}$, R is almost constant. This initial delay between adding the dopant and the most significant change in R is attributed to the time which toluene molecules require to diffuse through helium†. The largest change in R happens during the second interval, $t_{II} \simeq 4 \cdot 10^3\,\mathrm{sec}$, which will be discussed below.

*Potential distribution was calculated in FEMLab by solving 2D Laplace equation taking into account the graphene density of states. However, the calculations suggest that the quantum capacitance of graphene is negligible at gate voltages higher than 0.1 V in amplitude and graphene in this case can be replaced by a metal with infinite DOS.

†A typical distance between sample surface and source of the dopant is $5 - 10$ cm.

Finally, the third interval t_{III}, beyond $7 \cdot 10^3$ sec, corresponds to either saturation in $R(t)$ dependence or to a drift of the resistance (as for the sample shown in Fig. 2.3) which can be associated with a constant increase in the number of adsorbed molecules.

As described in Sec. 2.3, toluene shifts the resistance peak towards negative gate voltages, Fig. 2.4(a). It also causes the hysteresis, so that the exact position of the maximum in $R(V_G)$ depends on both the direction and the rate of sweeping V_G. This hysteretic behaviour can be ascribed to a particular time delay τ in the system.

Generally, two types of time delay can be distinguished. The first type is caused by lag in the measurement circuit. For example, low-pass filters are commonly used in experimental setup in order to smooth random spikes, coming from the gate voltage source, and avoid damage to the sample. These filters can cause the delay in applied V_G. For example, a typical value for the filters used in our measurements is $RC = 100\,\text{kOhm}\cdot 2.2\,\mu\text{F} \simeq 0.2\,\text{sec}$. It will be seen in Sec. 2.5.3 that this value is negligible in comparison with a characteristic time $\sim 4000\,\text{sec}$ of the studied effect. Also, measuring equipment (for instance lock-in amplifiers) has a similar filtering of the output signal. (Characteristic time of the filters is set by the time constant of the lock-in amplifier and is usually less than 1 sec.) In both cases the recorded resistance is not a characteristic of the sample at the time of the record t_0, but at the time $t_0 - \tau$. This type of delay results in a hysteresis, where the right hysteretic peak would appear when the gate voltage was being swept from negative to positive V_G, and vice versa. This is opposite to what is seen after toluene doping.

The second type of delay is a result of both the non-zero time lag in the reaction of the sample to an external perturbation (in our case the gate voltage) and the existence of such a reaction. For example, hypothetically, the level of the doping can depend on the absolute value of the applied gate voltage. Therefore, changing V_G in this case would cause an additional transfer of electrons between graphene and dopant molecules. The transfer process could be determined by a particular mechanism with a corresponding intrinsic time delay, and eventually would result in a delay in the sample response to the changing V_G. Let us assume that such a mechanism exists for the case of toluene doping. It can be shown that the hysteresis seen in Fig. 2.4 can be associated with this mechanism. During the sweeping of V_G from the right to the left, the number of transferred electrons is continuously adjusting with changing gate voltage and the Dirac point position is continuously moving to the left. This means that at the very

left point where $V_G = -30\,\mathrm{V}$ the position of the Dirac point is shifted to the left with respect to the position observed during the sweep (during the sweep from positive to negative V_G the Dirac point was seen at $\sim -10\,\mathrm{V}$). Therefore, the Dirac point position seen during the sweep from negative to positive V_G is not at $\sim -10\,\mathrm{V}$ anymore but shifted to $\sim -24\,\mathrm{V}$. (A more detailed explanation of the toluene doping effect will be given later in Sec. 2.5.8.) Thus, the second type of time delay cannot be reduced by decreasing the sweeping rate of V_G, on the contrary it will be enhanced (the slower the sweeping rate the larger the response of the system).

Later it will be shown that the doping of graphene by toluene can be indeed ascribed to a particular mechanism leading to a time delay of the second type.

2.5.2 Molecular doping mechanism

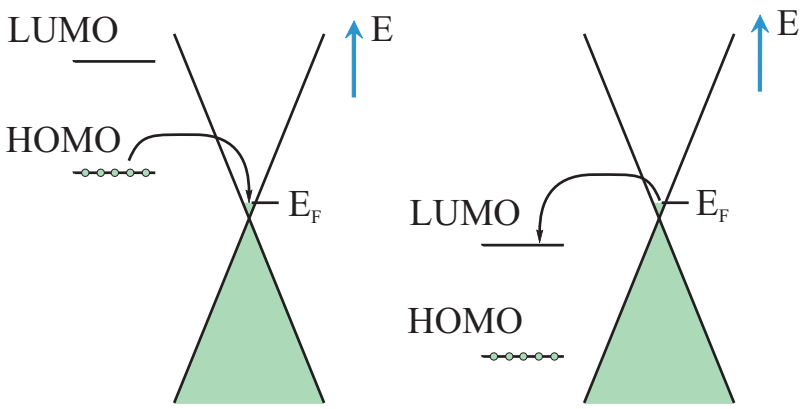

Figure 2.6: Transfer of electrons during molecular doping is shown schematically for two cases. Left: dopant donates electrons. Right: dopant accepts electrons.

Although it is already clear that doping by toluene is not a simple process (interaction between dipole moment and electric field, hysteresis), it is still worth examining the hypothesis that toluene molecules use the simplest possible way to donate carriers to graphene: molecular doping. In this section this phenomenon will be described and the main characteristic features of it will be pointed out.

The term "molecular doping" in this thesis is defined as the direct transfer of electrons between the Fermi level of graphene and either highest occupied molecular orbital level of dopant (HOMO level) or lowest unoccupied molecular orbital level (LUMO level). If the HOMO level of the dopant is higher than the Fermi level of graphene, then it is energetically favourable for electrons to tunnel from the dopant to

graphene, Fig. 2.6. Similarly, if the LUMO level of the dopant is lower than the Fermi level of graphene, then electrons tunnel from graphene to the dopant. Although in both cases the transfer of electrons is energetically favourable, the electrons still have to tunnel through or jump over the potential barrier between graphene and dopant molecules. Therefore, if the thermal excitation energy is lower than the height of this barrier, the doping will be limited by the tunneling mechanism only and in some cases practically absent. Finally, if the graphene Fermi level lies in between the HOMO and LUMO levels no exchange of electrons occurs.

Doping of graphene by potassium atoms is a well understood example of molecular doping [25]. As seen in Fig. 1.9, the dependence of the graphene conductivity, σ, on the gate voltage is shifted towards negative voltages after each dose of the potassium doping indicating the transfer of electrons to graphene. Using density functional theory (DFT) calculations it was shown that the HOMO level of potassium is indeed higher than the graphene Fermi level [50], which results in the doping by electrons and agrees with the experiment. Calculations also suggested that each potassium atom donates 1 electron, thus, knowing the number of adsorbed atoms on the sample surface one can estimate the number of donated electrons, and vice versa.

Graphene band structure provides a direct method for evaluating the concentration of transferred carriers. Namely, the maximum in $R(V_G)$ dependence (or minimum in conductivity dependence) appears exactly at the charge neutrality point (Dirac point), where the average concentration of carriers is zero. By doping graphene one adds extra amount of carriers and, therefore, shifts the position of the neutrality point. Then, knowing the capacitance between graphene flake and a gate, the voltage shift of the maximum can be converted into the number of transferred carriers. For example, Fig. 1.9 shows the $\sigma(V_G)$ dependences for different stages of the exposure of the sample to potassium. The initial position of the minimum was $V_{D1} \simeq -9\,\mathrm{V}$ and it shifted to $V_{D2} \simeq -23\,\mathrm{V}$ after 6 seconds of doping. In our typical graphene device (see Sec. 1.2.1) the relation between concentration of electrons n and gate voltage reads $n(V_G) = 7.2 \cdot 10^{10} \cdot (V_G - V_D)\,\mathrm{cm}^{-2}\mathrm{V}^{-1}$*, Sec. 1.2.2, where V_D is the position of the Dirac point.

*Negative concentration means that there are holes in the channel, not electrons.

Therefore, for the change in concentration of electrons during the doping we have

$$\Delta n = n_2(V_G) - n_1(V_G) = 7.2 \cdot 10^{10} \left((V_G - V_{D2}) - (V_G - V_{D1})\right) = \\ = 7.2 \cdot 10^{10}(V_{D1} - V_{D2}) \simeq 10^{12}\, cm^{-2}. \tag{2.1}$$

Positive value of Δn means that the electrons were added to the channel, which is in agreement with the calculations presented in Ref. [50].

Now, let us turn back to toluene. DFT calculations showed that the HOMO(LUMO) level of toluene lies 1.1 eV below (3.9 eV above) the Fermi level of graphene [50, 51], and, therefore, no direct transfer of electrons is possible. Moreover, molecular doping is a permanent effect* and it does not change unless the dopant is removed from the surface; while the effect of toluene reveals an unusual hysteresis, which is likely to be caused by changing the doping level with changing V_G, Sec. 2.5.1. Thus, it is concluded that the toluene effect cannot be ascribed to a simple molecular doping mechanism. In addition, water was also found to be unable to donate carriers via molecular doping mechanism [52], which strengthens the analogy between water and toluene doping effects. There have been no similar studies for aniline.

2.5.3 Characteristic times

In Fig. 2.7(a) the time dependence of the normalised change of resistance, ΔR_N, of sample AG4D4 is shown. The annealed sample was measured in helium atmosphere, where, ideally, the resistance is expected to be constant in time (if V_G is fixed). After $\sim$ 2 hours measuring $R(t)$ dependence at $V_G = 0\,\mathrm{V}$ (black line) the gate voltage was rapidly swept to $-30\,\mathrm{V}$ and the time dependence was measured again (red line). Then, in the same manner V_G was sequentially changed to 0 V, to 30 V and back to 0 V measuring $R(t)$ dependences at each voltage for 1 hour. As seen, the resistance was found to be stable at $V_G = -30\,\mathrm{V}$ and 0 V (although insignificant drifts are often present during the measurements). However, after switching to $V_G = 30\,\mathrm{V}$, the resistance started to increase indicating a parasitic effect which has no or little relation to the main effect of toluene (no toluene had been introduced yet at this stage). This increase in R can be ascribed to doping by residual contamination left on the inner surface

*In theory molecular doping also can depend on V_G if the Fermi level is shifted by the gate voltage close to the position of the HOMO(LUMO) level. However, in transport measurements this is practically not possible.

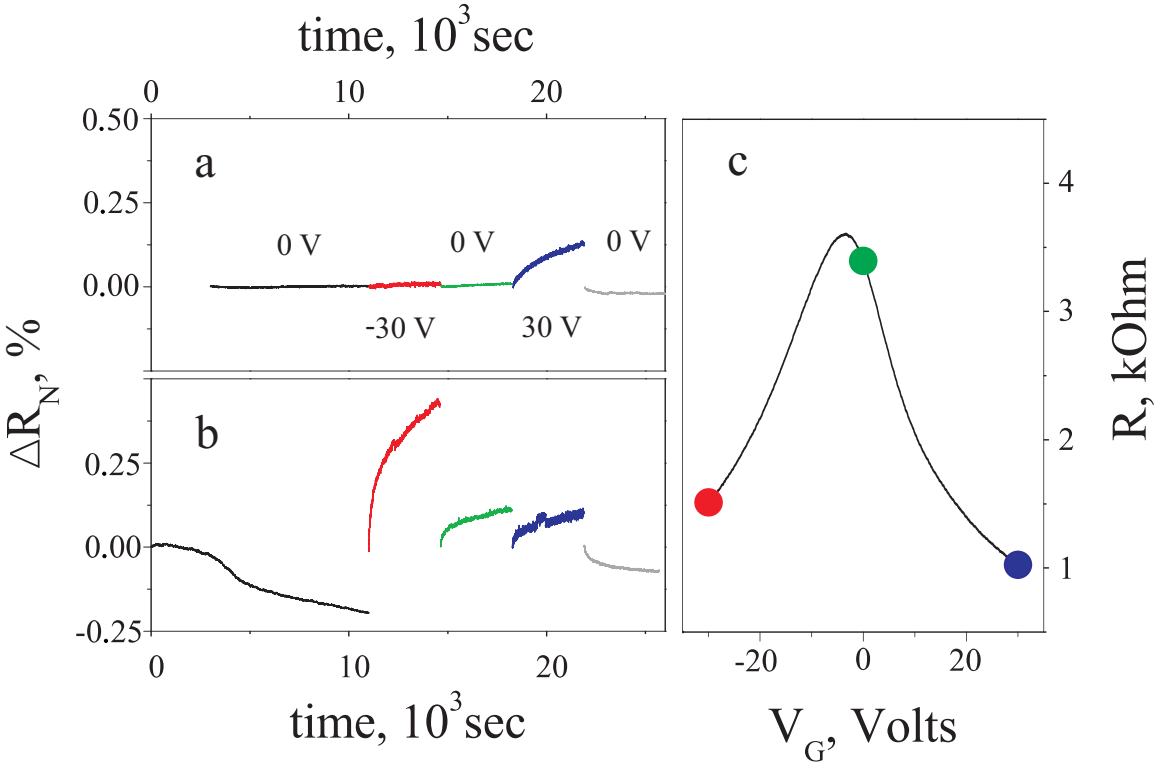

Figure 2.7: Normalised change of resistance, ΔR_N, measured as a function of time (a) in helium and (b) in toluene vapour, after rapid changes in the gate voltage: from $V_G = 0\,\mathrm{V}$ to $-30\,\mathrm{V}$, to $0\,\mathrm{V}$, to $30\,\mathrm{V}$ and back to $0\,\mathrm{V}$ (sample AG4D1). Panel (c) shows $R(V_G)$ dependence measured before doping by toluene. Gate voltages, where the time dependences were measured, are indicated by coloured points.

of the chamber. In spite of the fact that the chamber was baked in oven at 100 °C before measurements, there is a chance that some contamination is still left. Also, after baking the chamber was open to the atmosphere at some stages, which opens access for atmospheric water. Moreover, it has been shown in Sec. 2.4 that water dopes graphene with holes and shifts the maximum in $R(V_G)$ dependence to the right. Therefore, staying on the right side of the $R(V_G)$ peak one should see the increase of the resistance during the doping by water - exactly what we see at $V_G = 30\,\mathrm{V}$. Thus, we have found that the sample is stable in helium environment, except for positive gate voltages which trigger the doping of graphene by residual molecules specifically sensitive to $V_G > 0$ (most likely water).

Time dependence of ΔR_N of sample AG4D4 during toluene exposure is shown in Fig. 2.7(b). Initially, the sample was stabilised at zero gate voltage for 3 hours. This time is enough for toluene molecules to reach graphene surface and dope it. When the sample was doped, $R(t)$ dependence was measured staying at different gate voltages, in

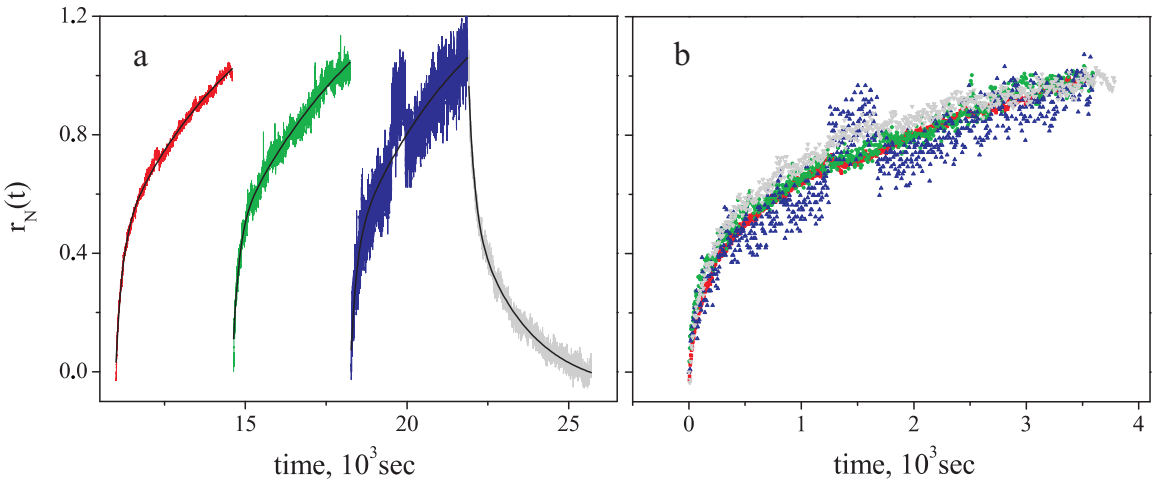

Figure 2.8: (a) Renormalised time dependences, $r_N(t) = \Delta R_N(t)/(R_{max} - R_{min})$, from Fig. 2.7(b) measured at $V_G = -30\,\mathrm{V}$, $0\,\mathrm{V}$, $30\,\mathrm{V}$ and $0\,\mathrm{V}$. The black curves show fits by Eq. 2.2. (b) Data as in (a) but shifted in time to $t = 0$. Grey curve ($V_G = 0\,\mathrm{V}$) is plotted upside down.

exactly the same way as described in the previous paragraph. Now let us compare the observed results with expected behaviour in the case of molecular doping. Once the sample is doped by a molecular doping mechanism, the level of doping (or number of donated/accepted electrons) is fixed. Therefore, at any gate voltage the resistance of the sample should be stable in time, which is clearly not the case for toluene doping. As seen in Fig. 2.7(b), immediately after setting a new V_G the sample resistance changes significantly, up to $\sim 45\,\%$.

Assuming that the shape of $R(V_G)$ dependence is not changed significantly by toluene, the change of the resistance can be transformed into the shift of Dirac point position (which is directly related to the level of doping as was shown in Sec. 2.5.2). First, the experiment was started at $V_G = 0$ V, on the right side of the $R(V_G)$ peak, close to the Dirac point, Fig. 2.7(c). During the initial doping the resistance was decreased by $\sim 20\,\%$ (Fig. 2.7(b), black curve), which means that the position of the Dirac point was shifted towards negative gate voltages by $\sim 5\,\mathrm{V}$ indicating doping by electrons. At this stage the Dirac point was at $V_G \simeq -10\,\mathrm{V}$. Second, V_G was swept to $-30\,\mathrm{V}$. Massive increase of R here indicates a $\sim 10\,\mathrm{V}$ shift of the Dirac point to the left - electron doping is larger than the initial doping at $V_G = 0\,\mathrm{V}$. Applying the same analysis to other points in V_G one can find the following effect: negative voltages "help" toluene to dope, whereas positive voltages induce an opposite effect - it diminishes or even reverses the doping. Thus, it has been established that the doping by toluene not

V_G,V	τ_1,sec	τ_2,sec
−30	200	4050
0	170	4720
30	180	4000
0	180	1730

Table 2.1: Characteristic times, τ_1 and τ_2, of the doping process, obtained as parameters in a fit by Eq. 2.2, are given at different gate voltages.

only depends on the gate voltage but also can be reversed.

Now let us focus on the character of time dependence of the doping process. Surprisingly, in spite of the fact that the magnitude of the resistance change depends on the gate voltage where it was measured, the change rate remains the same. This is clearly seen in Fig. 2.8(b), where renormalised curves from Fig. 2.7(b), $r_N(t) = \Delta R_N/(R_{max} - R_{min})$, are all shown on the same plot. These dependences can be fitted by a simple two-exponential decay formula

$$r_n(t) = r_0 + A_1 \exp\left(-\frac{t}{\tau_1}\right) + A_2 \exp\left(-\frac{t}{\tau_2}\right), \tag{2.2}$$

where r_0, A_1, A_2, τ_1 and τ_2 are constants. There are two characteristic times of the doping process: short time $\tau_1 \simeq 200\,\text{sec}$ and long time $\tau_2 \simeq 4300\,\text{sec}$ (the values of τ_1 and τ_2 for different curves are given in Table 2.1).

One can notice that the fit of the grey curve (see Fig. 2.8(a), $V_G = 0\,\text{V}$) gives $\tau_2 \simeq 2000\,\text{sec}$. This discrepancy can be explained by the fact that the exponential dependence, described by Eq. 2.2, is actually expected for the number of donated electrons, not for the resistance itself. Therefore, the dependence of the resistance on concentration can contribute to the measured $R(t)$ dependence and result in a large error in determining τ_2. Furthermore, this effect can also be related to the existence of the short time τ_1 in the fit. As it will be shown later, dependence of the Dirac point position on time can be fitted with a single exponent decay with a characteristic time of the same order as τ_2. Thus, only τ_2 is relevant to the studied effect and is obtained here as $\simeq 4000\,\text{sec}$ with a factor of 2 accuracy.

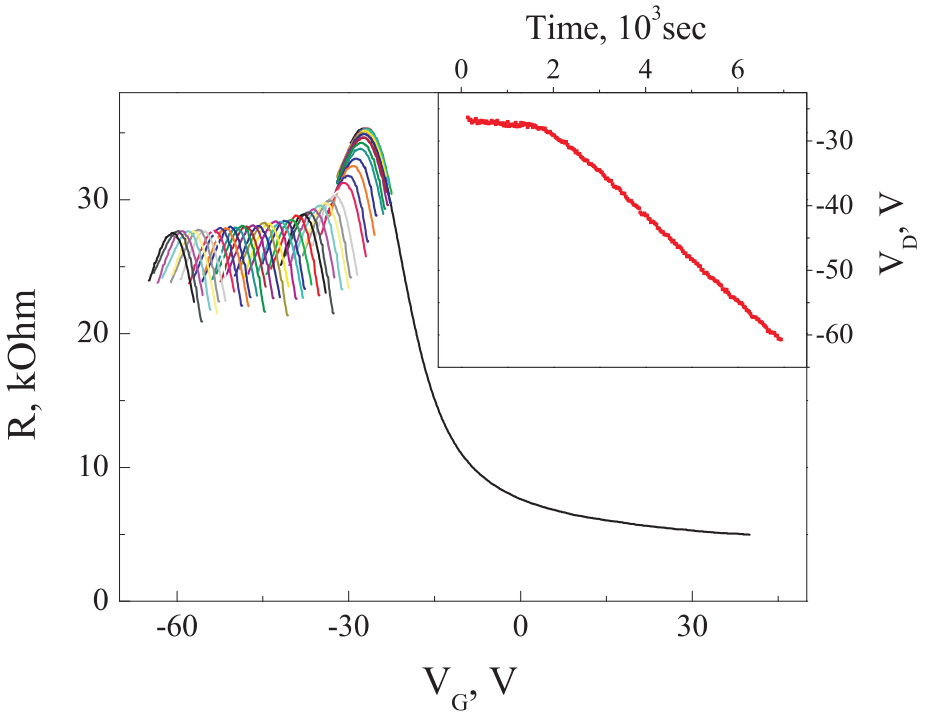

Figure 2.9: Resistance as a function of the gate voltage measured every 40 minutes during the doping by toluene (sample AG3D10). Initial $R(V_G)$ dependence is given as a black curve in the range $[-30;40]$ V. Inset: The position of the Dirac point, V_D, as a function of time.

2.5.4 Enhancement of the doping by electric field

It has already been established from $R(t)$ curves, that the level of doping depends on the gate voltage, Sec. 2.5.3. One can see this directly by monitoring the position of the Dirac point during the doping. This was done in the following experiment. First, sample AG3D10 was annealed and the Dirac point position was found to be at $V_G = -27\,\mathrm{V}$. Immediately after adding the vessel with toluene inside the chamber, the gate voltage was rapidly swept from $0\,\mathrm{V}$ to $-27\,\mathrm{V}$. After that the gate voltage was continuously swept in the range $\pm 4\,\mathrm{V}$ around the Dirac point throughout the whole experiment. Therefore, practically the position of the neutrality point was measured every 8 minutes* (although in Fig. 2.9 every fifth curve is shown, which means that the time interval between them is 40 minutes). Since the initial position of the Dirac point was negative and toluene shifts it further towards negative V_G, the gate voltage was below $-24\,\mathrm{V}$ during the whole experiment.

The results of the experiment are shown in Fig. 2.9. One can see that the resistance

*Time required to measure a single $R(V_G)$ dependence is determined by the voltage range, $\pm 4\,\mathrm{V}$, and the sweep rate, $1\,\mathrm{V}$ per minute.

peak constantly shifts to the left with no sign of saturation, which leads to two conclusions. First, this is consistent with the effect found in Sec. 2.5.3: negative V_G increases the level of doping. Second, the absence of saturation can be easily understood. The experiment started at negative gate voltage ($-27\,\mathrm{V}$). Applied negative voltage caused an additional doping by toluene and, therefore, shifted the Dirac point further to the left. During the measurements V_G was swept in $\pm 4\,\mathrm{V}$ range around the Dirac point, which means that as soon as the Dirac point shifts, the average applied V_G increased in magnitude (although stayed negative). Increase of the gate voltage again caused additional doping, and so on. This bootstrapping of the doping process provides a nonsaturable transfer of electrons from toluene to graphene.

For each measured $R(V_G)$ curve the position of the Dirac point, V_D, was found and plotted as a function of time, Fig. 2.9, inset. The plot shows, that there is an initial delay where V_D changes insignificantly. The same delay of the same order of magnitude was observed in Sec. 2.3 and was associated with a time, required by molecules to diffuse through helium. After the delay, the $V_D(t)$ dependence is almost linear with the slope $\sim 0.4\,\mathrm{V/min}$ or ~ 24 V/h, which gives us the rate of doping under given experimental conditions. This value is about 5 times higher than the rate of the doping in our usual experiments, where $R(V_G)$ dependence was measured once in an hour in a symmetric range of V_G*. Thus, it has been found that the doping can be enhanced significantly by applying a negative gate voltage. Moreover, no saturation point was revealed down to $-60\,\mathrm{V}$ (higher voltages were not used due to a high probability of the dielectric breakdown, especially in the vicinity of the toluene vapour).

2.5.5 Doping dependence on the gate voltage

In a previous subsection, it has been shown that the zero field equilibrium between toluene and graphene, reached by donation of electrons to the channel, can be easily changed by applying a gate voltage. The bias between the gate and graphene causes imbalance in the electron density and leads to an additional transfer of carriers until a new equilibrium is reached. The experiment described in Sec. 2.5.3 revealed the fact that this new equilibrium actually exists, as the resistance was saturating in time after a change of V_G. By a quantitative analysis the characteristic times of the process, but

*Symmetric range of the gate voltage is used to minimize the effect of the voltages of different signs.

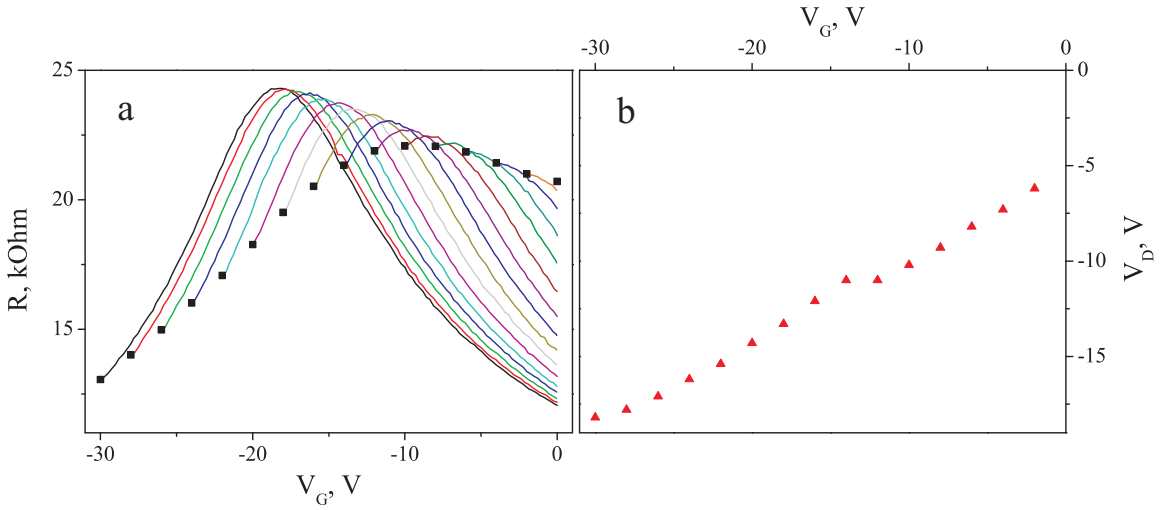

Figure 2.10: (a) Resistance of the graphene sample AS1D1 after 1 hour waiting at different gate voltages (black points). Curves show quick sweeps from a waiting point (where the saturated resistance was recorded) to $V_G = 0\,\mathrm{V}$. (b) The Dirac point position of the $R(V_G)$ curves shown in (a) as a function of the starting gate voltage.

not the magnitude of the effect, were extracted.

To deduce how many electrons have been transferred over the course of establishing equilibrium, one needs to know the initial and the final positions of the Dirac point. The equilibrium position is strictly determined by the fixed gate voltage. Therefore, to reach equilibrium V_G needs to be kept constant, but to find the position of the resistance peak, one has to measure $R(V_G)$ dependence and sweep V_G. This self-closed problem cannot be resolved, unless $R(V_G)$ dependence is measured within the time interval $\Delta t \ll \tau_1 < \tau_2$. Then, during the time Δt the change in the doping, as well as the dirac point position, will be negligible and can be treated as constant.

In Fig. 2.10(a) the results of the experiment, where the position of the Dirac point at different gate voltages was measured without changing the level of the doping, are shown. First, an annealed sample was doped by toluene at $V_G = 0\,\mathrm{V}$. Then, V_G was swept to $-30\,\mathrm{V}$ and stopped for 1 hour in order to reach the equilibrium level of the doping. After that, the saturated value of the resistance (shown in the figure by black points) was recorded and $R(V_G)$ dependence was measured with $1\,\mathrm{V/s}$ sweeping rate*. Then, gate voltage was swept to a new point, stopped for another hour, resistance was recorded again, $R(V_G)$ dependence was measured and so on.

*At high rates of the sweeping the gate voltage one has to use a small integration time on the lock-in amplifier in order to avoid delays in the circuit. This causes fluctuations of the signal with the period equal to the product of the sweep rate and the time constant, which can be seen under careful examination of Fig. 2.10(a).

In the end of the experiment there was a set of $R(V_G)$ dependences (or practically a set of the Dirac point positions) corresponding to a set of the equilibria (each equilibrium is determined by a specific gate voltage). With 1 V/s sweep rate and sweeping at most from -30 V to 0 V, the time of measurement of the Dirac point position was less than 30 seconds, and, therefore, less than any of the characteristic times of the doping process (Sec. 2.5.3). This means that the doping level did not change during the sweeping of V_G and, consequently, measured Dirac point positions indeed reveal the number of transferred electrons at a particular gate voltage.

Figure 2.10(b) shows the position of the maxima of the curves from panel (a) as a function of the starting gate voltage. The plotted dependence is almost linear, which implies a linear relation between the gate voltage applied and the number of transferred electrons. This means that in the presence of toluene vapour by tuning V_G one can achieve any required doping level up to $2 \cdot 10^{12}$ electrons per cm^2. Furthermore, the experiments described in Sec. 2.5.4 show that there is no limit in the doping level down to $(60 - 27)7.2 \cdot 10^{10} \simeq 2.4 \cdot 10^{12}\,\mathrm{cm}^{-2}$ (which results in the curve similar to that in Fig. 2.10(b), but continuing further down to -60 V without saturation). However, this doping is driven by the gate voltage and as soon as the gate voltage is changed back to zero, the doping vanishes. The role in the gate dependence of the doping of the interaction between the dipolar dopants and "stray" electric field above the flake remains unclear. Thus, at this stage toluene cannot be used as a permanent dopant, for example, for producing a p-n junctions, although, as we will see below, the pumping out of the toluene vapour can fix the doping level to some extent (Sec. 2.5.6).

2.5.6 Effect of pumping and annealing

A typical $R(V_G)$ dependence of graphene sample after doping by toluene implies a hysteretic behaviour with two peaks separated by $10-60$ V *, Fig. 2.4. Experimentally, this behaviour is seen in the presence of toluene vapour in the vicinity of the sample. During exposure, toluene evaporates from the vessel until the pressure of gaseous toluene reaches its saturation limit. (At 25 °C the vapour pressure of toluene is 3.8 kPa [45].) This environment provides an inexhaustible source of toluene molecules, which can be easily involved in the doping process. Therefore, it is reasonable to assume that

*The actual value depends on the gate voltage range and on the sample sensitivity to toluene. Sensitivity presumably depends on the roughness of the graphene surface and cleanliness of it.

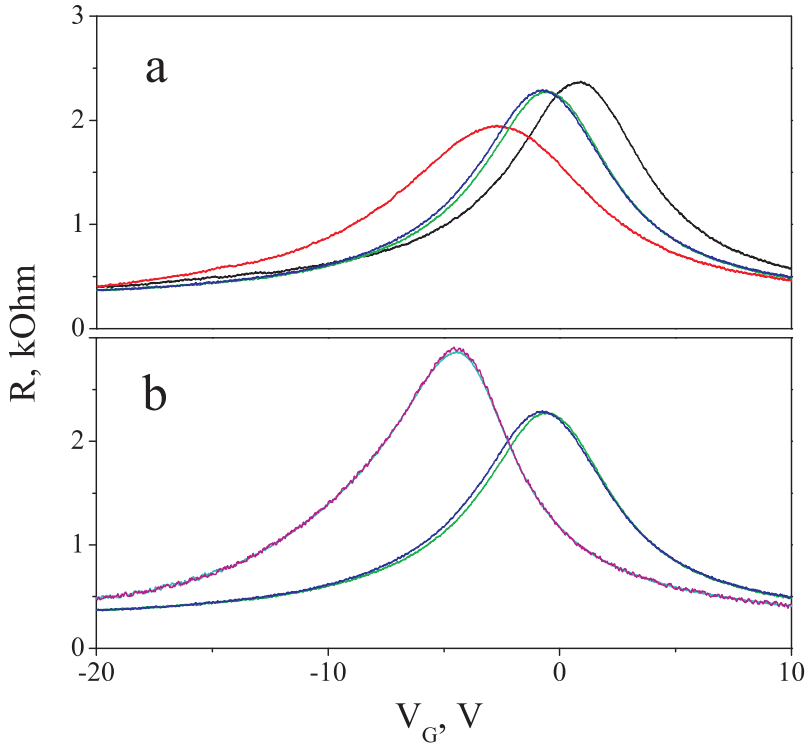

Figure 2.11: (a) Resistance of sample G22D8 doped by toluene as a function of the gate voltage before (black and red curves) and after (blue and green curves) pumping the chamber. (b) $R(V_G)$ dependence after pumping (as in (a), right peak) and after 140 °C annealing (left peak) in vacuum. Two curves for each stage of the experiment are plotted to show the hysteretic behaviour of the sample.

observed hysteresis is caused by the presence of toluene molecules available for doping. The actual mechanism causing the hysteresis should be closely related to the origin of the doping and will be discussed later.

One can estimate the number of transferred electrons from toluene to graphene by the shift of the Dirac point in $R(V_G)$ dependence during the doping. Typical value of the shift is $\sim 20\,V$, thus, giving the number of transferred electrons to be $\sim 20 * 7.2 \cdot 10^{10} \sim 10^{12}\,\mathrm{cm}^{-2} = 10^{-4}\,\mathring{A}^{-2}$. Assuming that a single toluene molecule donates a single electron and knowing that the surface area of the toluene molecule is $\sim 5{*}5\,\mathring{A}^2 = 25\,\mathring{A}^2$, the surface coverage of the graphene by toluene can be estimated as $25/10^4 = 0.0025$, that is $\sim 0.3\%$. This suggests that the saturation of the doping seen in the experiment is not caused by the limited surface of the graphene flake available for interaction with the dopant, but by some other mechanism, which is also controlled by the gate voltage.

The sealed chamber, where all the experiments were performed, allows removal of the toluene vapour by pumping (after removing the liquid from the chamber there is

still a vapour of toluene) and therefore the ability to examine the relation between the hysteretic behaviour and the environment of the sample. In Fig. 2.11 different stages of the experiment are shown. Sample G22D8 was doped by toluene and, as a result, exhibited a typical hysteresis in $R(V_G)$ dependence, panel (a). Then, the toluene source was removed from the chamber*, and the chamber was pumped down to 10^{-2} mbar. The $R(V_G)$ dependence after pumping reveals no hysteresis, Fig. 2.11(b), instead, the resulting resistance peak appears roughly in the middle between the two initial hysteretic peaks.

From previous experiments it is known that toluene doping is strongly affected by the gate voltage, Secs. 2.5.4 and 2.5.5, and that the hysteresis reflects the ability of the doping level to adjust with changing V_G. It is reasonable to assume that this ability is associated with the presence of the source of new toluene molecules, which can donate extra electrons to graphene. By pumping the chamber one removes the source of toluene and suppress the adjustability of the doping level. The Dirac point position after pumping is determined by two factors: the gate voltage at which the toluene was removed and the average doping level (average is taken with respect to different gate voltages). If during the pumping $V_G = 0\,\mathrm{V}$, which means that the doping level is not affected by the gate voltage, the Dirac point appears in the middle between two hysteretic peaks, as it shows the average doping of level exactly. However, if $V_G \neq 0$, then the doping level immediately before pumping corresponds to the applied V_G (Sec. 2.5.5), and, therefore, it will remain the same also after pumping. This conclusion was confirmed experimentally, although the real position of the Dirac point was observed to behave with some deviations from what was expected. Surprisingly, the $R(V_G)$ dependence after pumping was found to be quite stable. This proposes a method of doping graphene permanently by any amount of electrons within a certain range, where the doping level is determined by the gate voltage applied during the removal of the dopant from the sample environment.

All the measurements described in this thesis were performed on preannealed samples at 140 °C (unless stated otherwise). Such a treatment is known to remove partially the contamination, particularly atmospheric water, which is absorbed on the graphene surface during the fabrication [53]. Since toluene is also a contaminant and its boiling

*Overpressure of helium insured that the sample was not contaminated by the atmosphere during this procedure.

point is 111 °C in normal conditions [45] (close to that of water), one might assume that it can be removed, at least partially, by the same annealing procedure. However, the results do not indicate that this is the case. Fig. 2.11(b) shows that after annealing the resistance peak does not shift back to its original position, where it was before doping by toluene. Moreover, the level of the doping increases.

There are two possible reasons for the increase of the doping with temperature. First, the doping is a process with a characteristic potential barrier, and an electron has to either tunnel through this barrier or jump over it in order to dope graphene. The barrier determines a maximum distance from the graphene surface, at which the molecules can still donate a carrier. This distance, in turn, determines the amount of molecules involved in the doping, and is proportional to the reactivity of toluene (more reactive molecules can donate an electron from greater distances). The reactivity of toluene can depend on temperature (if, for example, the donation is thermally activated, or the tunneling is not resonant), so that by increasing the temperature one enhances the reactivity of toluene, and consequently, increase the doping level. By decreasing the temperature, one weakens the reactivity, and the tunneling barrier is no longer passable for electrons from distant donors, which makes the doping fixed and stable, as observed in experiment. The second possibility is that high temperature enhances the mobility of toluene molecules on the graphene surface and they start to rearrange themselves, geometrically choosing more energetically favourable positions. Rearrangement can lead to a better access of toluene to the surface and can increase the number of active donors, which, again, enhances the reactivity of toluene. However, based on our observations it was not possible to determine which of the two mechanisms is realised*.

The role of the temperature can be investigated by measuring $R(V_G)$ dependence at different temperatures. In fact, our setup allows sample measurement at temperatures up to 140 °C, although the SiO_2 can be easily damaged at such temperatures due to electrical breakdown, especially in the presence of toluene vapour. Therefore, the only possible way to study the temperature effect is to measure the initial $R(V_G)$ dependence, thermally cycle the sample to high temperatures, and measure $R(V_G)$ again. One of the samples doped by toluene was annealed at 200 °C in the different setup with constant

*Possibly, the mapping of the surface of the graphene can reveal the rearrangement of the molecules on top of it, thus, distinguishing between the two mechanisms. Also, studying the temperature dependence of the reactivity of the toluene can presumably indicate the difference between them.

flow of H_2/Ar mixture through the chamber. Interestingly, after annealing the Dirac point was restored to its initial position, where it was before doping (this experiment was not reproduced). Thus, it was found that annealing at 200 °C removes the doping and restores the Dirac point position, while heating the sample to 140 °C increases the doping by toluene. To find the transition temperature, above which the toluene can be annealed, and whether the atmosphere is important, one needs to carry out more experiments of a similar kind.

2.5.7 The third reactant

Since the molecular type of doping was excluded in Sec. 2.5.2, the interaction between graphene and toluene only cannot explain the observed effect. Therefore, one has to assume that the doping process involves a third substance. There are several possible candidates due to uncleanliness of the fabrication procedure: solvent and developer residues, PMMA, gold and chromium atoms and, finally, atmospheric water and any other contamination which comes from the open environment to both surfaces of the graphene flake.

Gold and chromium atoms are known to group in clusters during the evaporation, which then form a thin film serving as a contact. Therefore, the concentration of the individual atoms (which do not form a cluster) on the graphene surface is believed to be not sufficient to play a substantial role in the doping. PMMA is a more likely candidate since toluene is known to be a solvent for it. Toluene vapour can detach the polymer chains of PMMA from each other, cause their rearrangement on the surface and lead to a doping by PMMA. Moreover, the literature provides indications that PMMA dopes graphene [54, 55]. The role of PMMA was checked by using PMMA-free samples, Sec. 1.2.3. The toluene effect on these samples was found to be qualitatively the same as on usual samples, which rules out the interaction between toluene and PMMA. The results obtained on both PMMA-free and usual samples are presented in the figures in this chapter. (All the characteristics including the fabrication technique are given for all samples in App. A.)

All the samples before exposure to toluene were annealed at 140 °C. This means that it is highly unlikely to have water molecules on the top surface of the graphene device. The presence of water trapped between the graphene and the substrate is

also ignored, unless one can assume that molecules, which do not tunnel through the graphene (or creep along the flake until they reach the edge) during annealing, will tunnel through it during the doping and interact with toluene. Thus, water is also ruled out as a candidate for explaining the toluene doping.

In conclusion, the particular substance involved in the toluene effect as a third component was not determined, although there is still evidence that it exists (since the interaction between graphene and toluene cannot explain the doping). Also, one cannot exclude the possibility that this role is played by additional contamination from the random impurities either from the solvents or from the environment.

2.5.8 Electrochemical reaction

Experimental evidence

Up to this point, several experimental facts have been established about the doping effect by toluene (and, possibly, all toluene-like molecules, such as aniline or water). First, exposure of graphene to toluene results in a doping by electrons. Second, the doping process has its own characteristic times $\tau_1 \simeq 200\,\text{sec}$ and $\tau_2 \simeq 4000\,\text{sec}$. Third, the number of transferred electrons strongly depends on the gate voltage applied during the doping, although at $V_G = 0\,\text{V}$ the doping is still finite. Fourth, the hysteresis, appearing after doping, vanishes when the toluene vapour is removed from the chamber. Finally, heating the sample up to 140 °C increases the doping, while annealing at 200 °C removes it.

The characteristic time τ_2 must be linked to a mechanism that slows down the doping process. Since the toluene is a common organic solvent and characteristic times of many chemical processes are close to that of the toluene doping, one can surmise that the origin of the toluene effect is a chemical reaction between graphene, toluene and some source of contamination (see Sec. 2.5.7). Furthermore, the dependence of the doping on the gate voltage and influence of the electric field on the toluene reactivity suggest that this reaction is electrochemical in nature. Toluene donates electrons, and the only possible way for toluene to lose an electron is oxidation. It oxidises to a radical, which, being a highly reactive ion, interacts with various residues on the graphene surface. Therefore, there are potentially many possible reactions that can follow oxidation, as many different residues are available for the interaction. This means

that it is impossible to say which particular reaction the radical actually undergoes (without any further analysis of the reaction products), and it is likely that there are many of them. However, it is reasonable to assume that the toluene effect is described by an effective electrochemical reaction with properties that are averaged among all the possible reactions. As will be seen, this approximation fits our results reasonably well.

Electrochemical cell

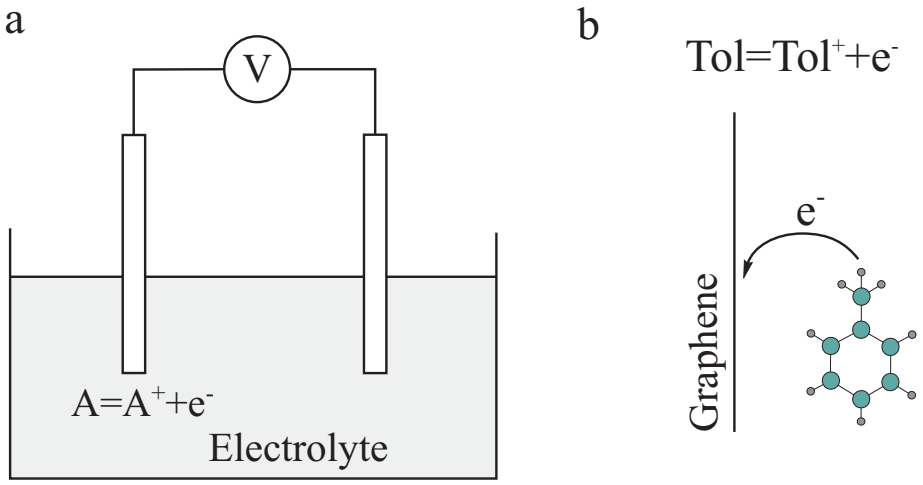

Figure 2.12: (a) An electrochemical cell shown schematically. (b) Toluene doping. Toluene and its radical are designated by Tol and Tol^+.

Usually, electrochemical reactions are studied within a so-called electrochemical cell [56], which in the simplest case consists of two electrodes separated spatially by an electrolyte, Fig. 2.12(a). A separate reaction is attributed to each electrode as it occurs exactly at the interface between the electrode and electrolyte. By applying a voltage bias between electrodes one can pass the current through the system and induce the electrochemical reactions at the interfaces. If the current flows from electrolyte to electrode, the reaction is called oxidation, since the electrode substance becomes oxidised during the process. In the opposite case the process is called reduction. Schematically the interface reaction (in the simplest case) can be presented as follows

$$A \rightleftarrows A^+ + e^-, \tag{2.3}$$

where A/A^+ is known as a redox couple, i.e. two species which can be converted into

each other by a reduction/oxidation reaction.

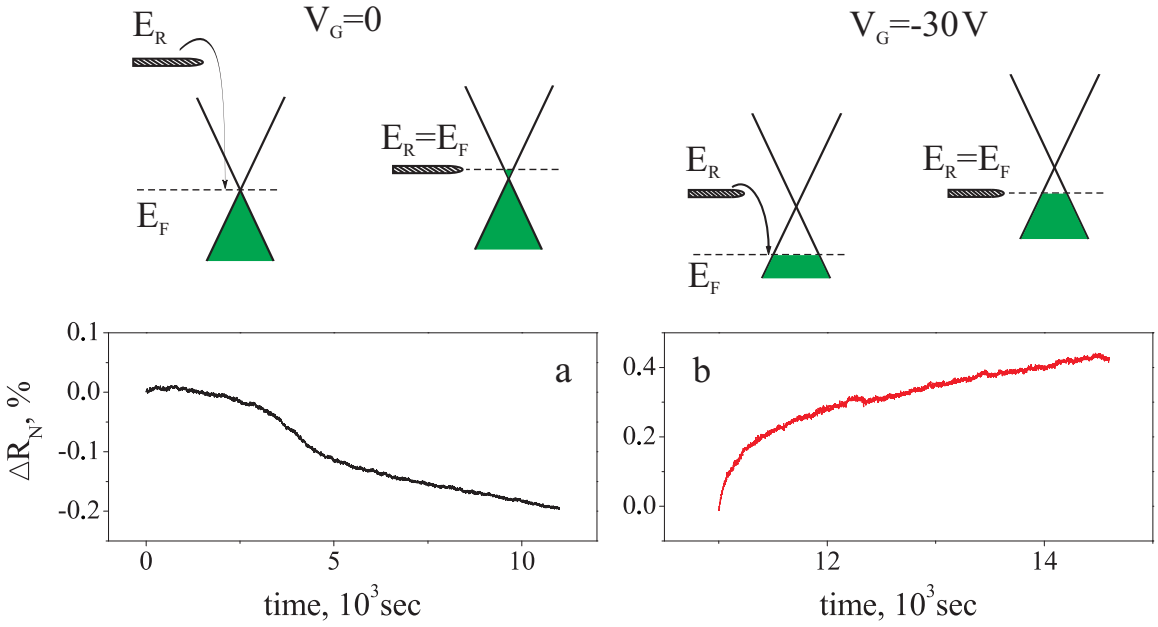

Figure 2.13: The same data as in Fig. 2.7(b). Two energy diagrams show the relative position of the Fermi level with respect to the redox level before and after measurements for each $\Delta R_N(t)$ dependence.

Thermodynamically, the reaction 2.3 can be described by a redox potential E_R given by the Nernst equation:

$$E_R = E_R^0 + \frac{RT}{zF} \ln(\frac{a_A}{a_{A^+}}). \tag{2.4}$$

Here E_R^0 is a standard redox potential, which is constant for each individual redox couple; R and F are the universal gas constant and Faraday constant, respectively; T is absolute temperature in the system; z is the number of transferred electrons during a single reduction/oxidation event (in our example of the reaction in Eq. 2.3, z equals 1); finally, a_A and a_{A^+} are reactivities of the correspondent species.

Reactivity is proportional to the number of molecules available for reaction, which makes the redox level dependent on the concentration of the species. Initially, when there are no molecules of the type A^+, the reduction level nominally is at infinity, which is higher than the Fermi level E_F of electrons in the electrode. The positive difference between the reduction level and Fermi level drives the forward reaction in Eq. 2.3. This decreases the reactivity of A, increases the reactivity of A^+ and, therefore, decreases the reduction level. Thus, the forward reaction continues until the reduction level is

aligned with the Fermi level, and the equilibrium is reached. It is crucial to understand that the redox couple at this stage can both donate to and accept electrons from the electrode depending on the relative difference between the energy levels.

In our case, the electrochemical cell consists of one electrode only - graphene, Fig. 2.12(b). The most probable redox couple is toluene and its radical, Tol/Tol^+ and the doping reaction is driven purely by the change in the energy difference between the Fermi level in graphene and the redox level of the couple Tol/Tol^+.

Let us now reconsider the doping process stage by stage. When toluene is introduced into the chamber it first diffuses through the helium, as concluded in Sec. 2.3. As soon as molecules reach the graphene surface they start to react with nearby contaminants and donate electrons until the redox level and the Fermi level in graphene coincide, Fig. 2.13(a). The energy diagrams show that in the beginning of the reaction the redox level is much higher then the Fermi level, $E_R \gg E_F$, which explains the finite doping even at $V_G = 0\,\mathrm{V}$. Also, at this stage E_R is very sensitive to the concentration of Tol^+ and, consequently, to the number of transferred electrons (since the concentration of Tol^+ is equal to the number of transferred electrons, Eq. 2.3). This results in a significant decrease in E_R and almost no change in E_F during the initial stage of the doping. When the gate voltage is abruptly changed from $0\,\mathrm{V}$ to $-30\,\mathrm{V}$, electric fields introduce an energy difference between E_R and E_F levels ($E_R > E_F$), which again triggers the forward reaction and converts more toluene molecules into its radical. The redox level is now less sensitive to the perturbations and does not change significantly, while the shift of the Fermi level compensates the difference in the levels. This leads to a large doping of graphene, which is seen as a massive change in the resistance ($\sim 45\%$), Fig. 2.13(b). Changing V_G towards positive voltages induces the difference of the opposite sign, $E_R < E_F$, and causes the reverse reaction, when the radical converts back into toluene.

The forward reaction is easy to initiate since the redox level is almost fixed and by applying a negative gate voltage of appropriate magnitude one can shift the Fermi level down, and dope graphene with any number of electrons*. This is confirmed by the experiments discussed in Secs. 2.5.5 and 2.5.4, where the level of doping was seen to have no saturation with increasing magnitude of negative V_G. The backward reaction

*The only limitation is the number of toluene molecules. If all the toluene is converted to its radical, doping stops. Practically, it is not possible to reach this limit without breaking the dielectric.

is, however, limited due to the finite amount of available toluene radical. (Initially its concentration is zero.) Therefore, in an ideal case, one can transfer all the electrons back to the redox level by converting all the Tol^+ back into Tol, although, it would require infinitely high positive V_G according to Eq. 2.4. Experimentally, moderate positive gate voltages (in the range between 30 and 60 V) were observed to almost recover the position of the Dirac point to its initial value (the difference was less than 5 V).

Observation of a threshold.

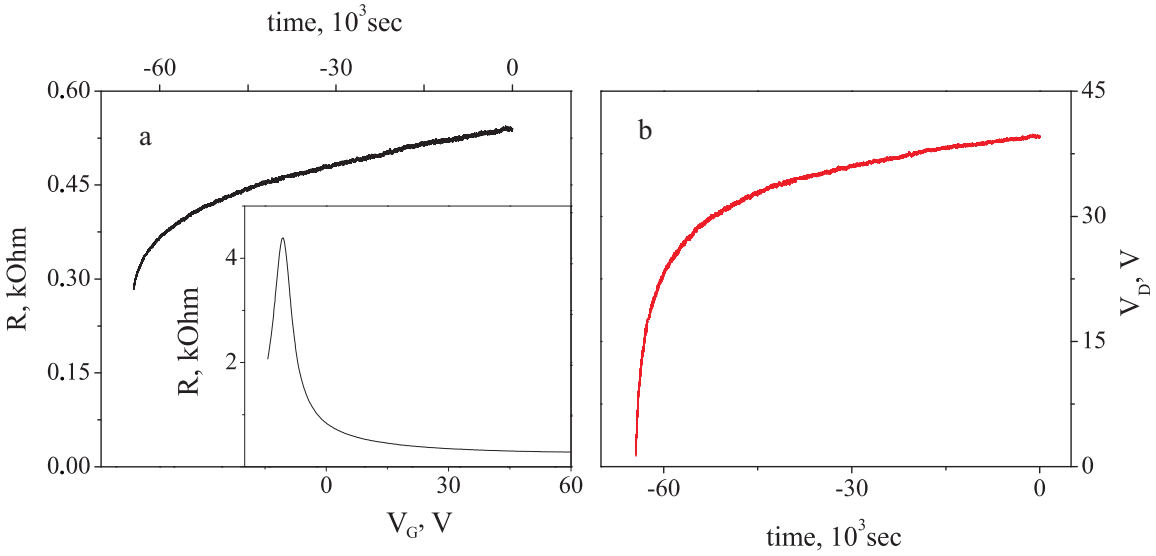

Figure 2.14: (a) Resistance of sample AG4D4 as a function of time at $V_G = 60$ V in helium atmosphere. Inset shows $R(V_G)$ dependence before the measurement of $R(t)$. (b) The position of the Dirac point as a function of time obtained from the data in (a).

To confirm that the doping effect by toluene is explained by an electrochemical reaction, the toluene effect at large positive gate voltages was investigated. First, a possible contribution from the background drift of the sample was estimated. The resistance of annealed sample AG4D4 as a function of V_G was measured in vacuum, Fig. 2.14(a), inset. The Dirac point was found to be at -10 V. Then, the chamber was filled with helium, gate voltage was swept to 60 V and $R(t)$ dependence was measured. Fig. 2.14(a) shows that an applied positive gate voltage causes a drift of the resistance peak towards positive V_G. (Similar effect was observed earlier, and a possible explanation was discussed in Sec. 2.5.3.) Assuming that the shape of $R(V_G)$ dependence does not change during the measurements, one can transform the $R(t)$ dependence into the

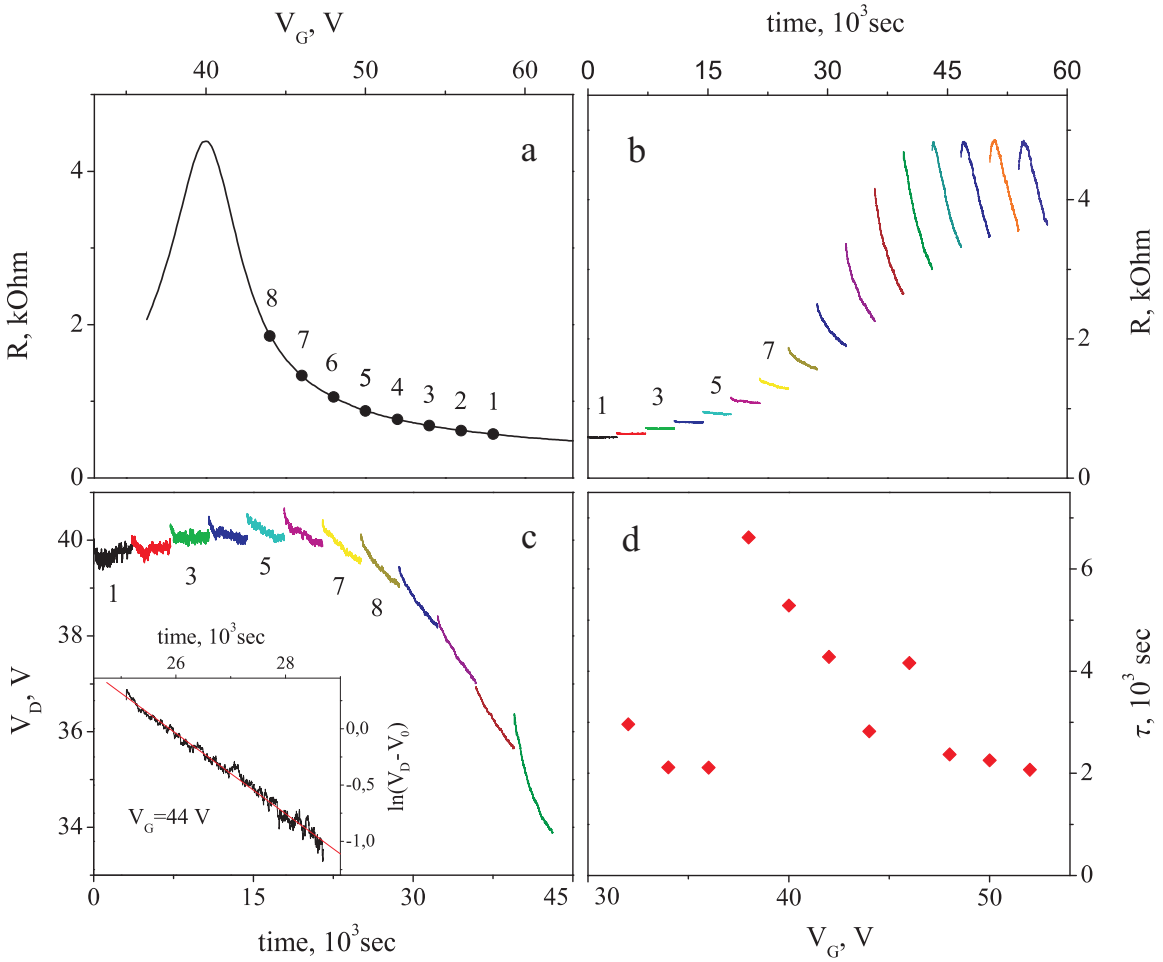

Figure 2.15: (a) $R(V_G)$ before the main experiment. Numerated points show the positions where $R(t)$ dependences were measured. (b) The resistance as a function of time at different V_G. (c) The position of the Dirac point during the experiment obtained from the data in (b). Inset shows the fit by Eq. 2.5 of $V_D(t)$ dependence at $V_G = 44\,\mathrm{V}$. (d) Characteristic times obtained from different fits in (c). Sample AG4D4.

dependence of the Dirac point position, $V_D(t)$. The resulting curve in Fig. 2.14(b) shows that the Dirac point drifted from 0 V to 40 V during $65 \cdot 10^3$ sec*. This gives us a rather high rate of the drift, about 2 V/h, although one should note that this value is determined by the large initial shift of V_G, therefore, smaller steps in gate voltage should cause slower drift. Moreover, in the next experiment with toluene the increase of the resistance was not observed, which allows us to ignore the background effect.

The stabilised sample at $V_G = 60\,\mathrm{V}$ was then exposed to toluene. The resistance dependence on time was measured for 1 hour at different gate voltages. V_G was changed abruptly with a 2 V step starting from 58 V, Fig. 2.15(a) (the points in V_G are num-

*The fact that V_D starts shifting from 0 V, and not from −10 V, tells us that the initial shift happened during the sweeping of V_G from 0 V to 60 V

bered). The $R(t)$ dependences are shown in Fig. 2.15(b). These results were then transformed into $V_D(t)$ dependence, Fig. 2.15(c), in the same way as for Fig. 2.14(b). As one can see, initially, at high V_G, the change of the resistance with time was negligible and the position of the Dirac point was nearly constant. At $V_G = 48\,\mathrm{V}$ (the 6th point in the V_G sequence) the resistance change during the measurement became observable, and increased further with decreasing the gate voltage. This suggests that there is a threshold position of the Fermi level (corresponding to 48 V), which separates two different regimes of the doping. In the first regime, when $V_G > 48\,\mathrm{V}$, the doping from the redox level is negligible, although the shift of the redox level is much larger than that of the Fermi level (as discussed above). In the second regime, $V_G < 48\,\mathrm{V}$, the redox level becomes less sensitive to V_G and does not shift significantly in comparison to the Fermi level. The threshold position is clearly seen in Fig. 2.15(c), where the Dirac point starts to change considerably not only with time, but also with changing V_G. An experimental observation of the threshold between two different doping regimes provides further evidence of the fact that the toluene effect can be explained by an electrochemical reaction.

The position of the redox level at the point where it crosses the Fermi level can be estimated for our case, although the obtained value will be of a low importance since it can vary in a rather broad range of energies for electrochemical reactions. Toluene starts to dope graphene at the threshold position of the redox level where $V_G \simeq 48\,\mathrm{V}$ and $V_D \simeq 40\,\mathrm{V}$, Fig. 2.15(c). Thus, the energy difference between the redox level and the Dirac point is $31\sqrt{|48-40|} \simeq 100\,\mathrm{meV}$ (see Sec. 1.2.2 for the formula reference).

Finally, the inset to Fig. 2.15(c) shows the fit to the $V_D(t)$ dependence (curve number 8) with the formulae

$$V_D = V_0 + A \cdot \exp -\frac{t}{\tau}, \tag{2.5}$$

where A and V_0 are constants, and τ is a characteristic time of the process. The fact that $V_D(t)$ dependences can be fitted by an exponential decay with a single characteristic time suggests that the necessity of two characteristic times, when $R(t)$ dependences were fitted, is coming from an additional dependence of the resistance on $(V_G - V_D)$ (see Sec. 2.1). Characteristic times, τ, for different $V_D(t)$ curves, Fig. 2.15(d), are all within the range between 2000 sec and 7000 sec. This suggests that the long time τ_2 is

indeed relevant for the toluene effect, whereas the short time τ_1 is a result of a parasitic effect.

2.6 Conclusions

In this chapter it has been shown that the $\pi - \pi$ interaction between graphene and dopants has no effect on the graphene electronic properties, in spite of the fact that this interaction results in an attraction between them. The dipole moment of the dopant was found to play a crucial role in the doping, since all the molecules tested that had a finite dipole moment have been seen to dope graphene, although the exact mechanism of the interaction between the dipolar molecules and graphene has not been understood. Finally, here for the first time a new type of doping was observed experimentally and described: electrochemical doping. It has been shown that toluene undergoes an electrochemical reaction in the vicinity of graphene, which serves as an electrode. Similarities between toluene, aniline and water allow us to conclude that water and aniline effects also can be explained by electrochemical reactions. This may finally clarify the origin of the doping of graphene by water, which has been a debatable question since the first observation of the effect. Molecules with zero dipole moments (naphthalene, pyrene) were found not to dope graphene possibly indicating that they are less chemically active than dipolar dopants.

Chapter 3

Random telegraph signals and flicker noise in graphene

3.1 Introduction

The phenomenon of flicker noise (also known as $1/f$ noise, or low-frequency noise) has been intensively studied for over 5 decades [57, 58]. Its importance in the electronics industry cannot be overstated, since this type of noise is one of the limiting factors for many device applications, particularly at low frequencies. Graphene nowadays is considered to be a promising candidate for replacing silicon in modern technologies, and, therefore, the investigation of flicker noise in graphene is crucial for further development in this direction. Moreover, in Si MOSFETs the flicker noise was shown to contain information about the impurity states near the conductive channel, which suggests that the noise can provide an additional insight into the scattering processes in graphene and help to reveal the dominant scattering mechanism which limits the carrier mobility.

Measurements of the flicker noise in both monolayer and bilayer graphene devices have been reported in Refs. [59–64]. Bilayer graphene, in contrast to monolayer graphene, was shown to have a suppression of the noise near the Dirac point [59]. Later, monolayer graphene was observed to exhibit behaviour similar to bilayer with some dependence on the method of fabrication [64]. (In Ref. [64] the temperature dependence of the noise was also measured.) With the development of techniques to produce double-gated graphene devices, the flicker noise was investigated in double-

gated bilayer samples [60,61,63], with an attempt to relate the noise with a band gap. However, in spite of the fact that the articles mentioned above contain information about the flicker noise in different graphene structures in various conditions, they are mostly inconclusive in the sense that they cannot explain the origin of the noise. Thus, the work described in this chapter attempts to link the observed effects between each other and study them in more detail.

Graphene transistors allow one to explore physics at various concentrations of holes and electrons. At high carrier concentrations charged defects are essentially screened by the carriers, while these defects are a possible source of the trapped states for hopping electrons. Therefore, suppression of the scattering due to screening leads to a suppression of fluctuations of the mobility of the carriers and results in a decrease of the magnitude of the resistance fluctuations. In contrast, at low concentrations the sensitivity of the carriers to the charged scatterers is enhanced, which results in an increase of the noise magnitude. The most interesting and complicated behaviour of the noise is expected at the Dirac point, where the resistance is determined by the hole-electron puddle percolation network [65], which provides additional mechanisms of the resistance fluctuations (for example, fluctuations in the percolation pattern [21]).

In this chapter the investigation of the flicker noise in supported* monolayer graphene devices will be presented. The flicker noise will be shown to be more sensitive to different scattering potentials than other transport properties of graphene. The noise behaviour is found to be affected by water doping and annealing. The evolution of the flicker noise with temperature will also be presented including its splitting into separate random telegraph signals at low temperatures.

3.2 Experimental techniques

Standard measurements of the low-frequency noise consist of the Fourier transform of the time dependence of the signal (in our case voltage drop on the sample), which is most commonly done by a spectrum analyser. The model used in our experiments, SRS 387, allows one to measure both the time dependence and Fourier transform of the signal over a broad frequency range, from 0.001 Hz to 33 kHz. All the spectra

*Most experiments were done on graphene on SiO_2/Si substrates, although the noise was also measured in devices supported by Si_3N_4/Si substrates.

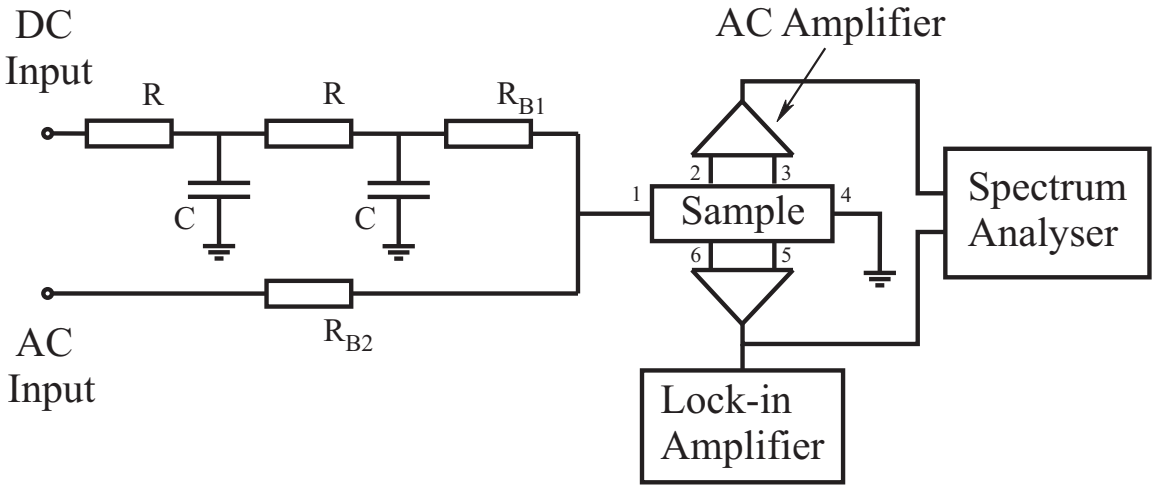

Figure 3.1: The measurement circuit is shown schematically. Filter resistances and capacitors are designated by R and C, respectively (typical values are 100 kOhm and 2.2 μF). R_{B1} and R_{B2} are ballast resistors providing the constant current regimes in DC and AC parts of the circuit. Contacts of the sample are numbered.

shown in this chapter were measured over the frequency range 1 Hz to 400 Hz with the accuracy 1 Hz. The Fourier transform provides general information about the noise and, therefore, is often used for determining the type of noise, whilst the direct measurement of the time dependence reveals the details of individual fluctuators and allows one to study the origin of the noise at a basic level. An alternative to a spectrum analyser is a lock-in amplifier (models 7265, 7225 and 5210 were used), which measures an amplitude of the fluctuations at a given frequency within a bandwidth determined by the time constant. Thus, it cannot be used for measuring the full spectrum and gives a noise spectral density effectively averaged over a certain bandwidth. However, in comparison to the spectrum analyser, the lock-in amplifier is a more convenient instrument, and, therefore, was used for most of our experiments. In our measurements the reference frequency was chosen to be ~ 30 Hz, and the time constant was set to 10 ms providing 12.35 Hz bandwidth.

The measurement circuit is schematically shown in Fig. 3.1. First, there is a mixer of alternating and direct signals (shown in the left part of the figure), which supplies the circuit with constant alternating (AC) and direct (DC) currents*. The AC part of the circuit is used for measuring the resistance of the sample and the DC part for

*The constant current regime is chosen due to the comparatively low resistance of typical graphene devices (high resistive samples, which can be produced by functionalisation of the graphene surface, were not measured in this work). The limitations on the ballast resistance in this regime are $R_{B1}, R_{B2} \gg R_{Sample}$

measuring noise. The low-frequency filters on the DC input are employed in order to prevent damage to the sample due to random spikes from the voltage source. Second, the mixed current is applied to the sample through the source contact (contact 1 in the figure), while the drain contact, number 4, is earthed. Contacts 2,3,5 and 6 are called potential contacts and are used for measuring the drop of the potential on the sample. Four-terminal measurements, which require 4 contacts on the sample, allow one to suppress the contribution from the contact resistance (resistance between the contact and the graphene flake) and are always used, unless otherwise specified. Third, AC preamplifiers are used to increase the signal by 100 times before applying it to the spectrum analyser or to the lock-in amplifier. For six-terminal devices it is possible to use a cross-correlation technique (as shown in Fig. 3.1), which implies the correlation between the signals from different pairs of the potential contacts. By means of this technique one can exclude the internal noise of BNC cables (which are used for all electrical connections between the equipment, filters and sample), preamplifiers, and contacts. Finally, the oscillator and ADC outputs of the lock-in amplifier are used as sources of AC and DC currents, respectively.

The phenomenon of the flicker noise is observed only when there is a finite direct current passing through the sample (the current is applied through the DC part of the circuit). On the other hand, the resistance of the sample is measured when the AC current is applied. Therefore, in order to exclude the contribution to the noise from the AC current (which is seen as a peak in the noise spectra at the oscillator frequency), the resistance and the noise were always measured separately. Also, both AC and DC currents can cause overheating of the sample and result in a nonlinear behaviour. To avoid this effect, the currents were adjusted correspondingly to the temperature in the system, and the range of used currents was confirmed by linear I-V characteristics of the resistance and the expected scaling of the normalised noise spectral density in the linear regime, $S_V \simeq V^2$.

Low temperature measurements of the noise were performed in a Heliox TL cryostat and a helium dewar with temperature ranges of $0.3\,\mathrm{K} - 200\,\mathrm{K}$ and $4.2\,\mathrm{K} - 300\,\mathrm{K}$, respectively. The cryostat was located inside a screened room in order to diminish the contribution to the noise from external electrical circuits including the power circuit. The dewar was used both inside and outside the screened room.

All the samples, used in this work, were confirmed to be monolayer graphene flakes

by optical contrast measurements (initial stage of fabrication, Sec. 1.2.1), Raman spectroscopy and/or measurement of the plateaus in the quantum Hall regime.

3.3 Scaling of the noise with frequency

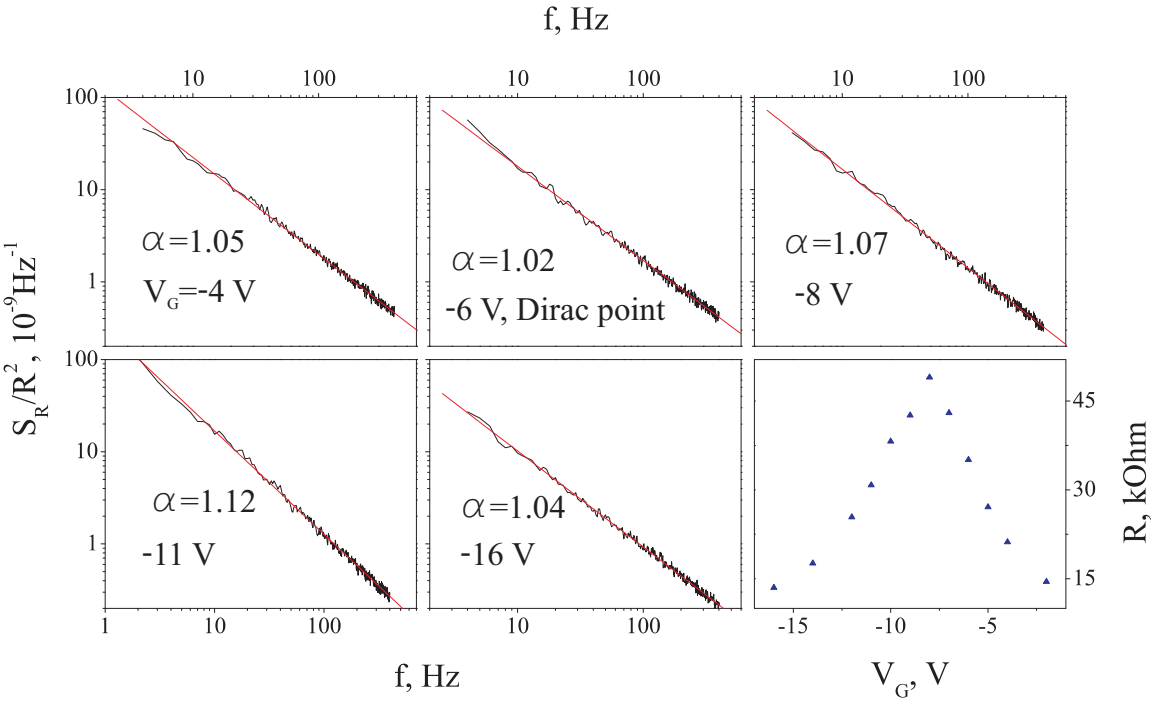

Figure 3.2: Normalised spectral density of the noise, S_R/R^2 , as a function of frequency at different gate voltages at $T = 70\,\mathrm{K}$ for sample FG9C4F1. Red lines show the fit with a $1/f^\alpha$ dependence. The $R(V_G)$ dependence for the sample is given in the right bottom panel.

As a first step in the flicker noise measurements, one has to confirm that the scaling of the noise magnitude is indeed $1/f$. In Fig. 3.2 the normalised noise spectral power, S_R/R^2, as a function of frequency, f, is shown at different V_G. All the spectra of fluctuating voltage difference between potential contacts were collected by the spectrum analyser. The constant DC current, I_{DC}, applied during the measurements was equal to $0.75\,\mu$A. As seen in the figure, the noise dependences at all gate voltages (corresponding to different concentrations) can be fitted with an $1/f^\alpha$ dependence, where $\alpha = 1 \pm 0.2$. Moreover, in all the graphene samples, at all concentrations and temperatures above $\sim 20\,\mathrm{K}^*$, the scaling of the noise with frequency can be successfully fitted with

*This limiting temperature is determined by particular distribution of the noisy defects with energy, and, therefore, can vary from sample to sample.

the same function. Thus, the frequency behaviour of the noise in graphene at low frequencies is described by the flicker noise phenomenon. Also, in spite of the fact that the resistance of graphene at low and high carrier concentrations is determined by different mechanisms, the scaling of the noise in these regions is still the same. However, as will be seen in the next section, this is not the case for the magnitude of the noise.

3.4 Room-temperature effects

3.4.1 Lock-in amplifier and spectrum analyser comparison

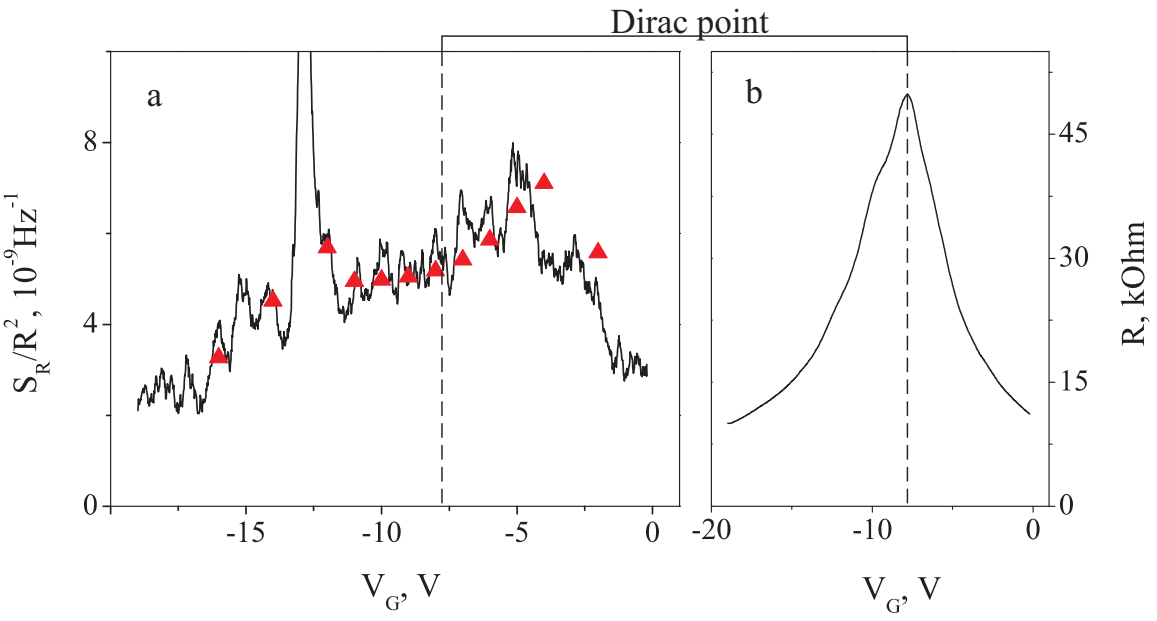

Figure 3.3: (a) S_R/R^2 as a function of the gate voltage measured at 30 Hz by the lock-in amplifier (black curve) and the spectrum analyser (red triangles) at $T \simeq 70$ K for sample FG9C4F1. (b) $R(V_G)$ dependence of the same sample at the same temperature.

By taking the value of the fitting functions in Fig. 3.2 at one particular frequency, one can compare the noise magnitude at different gate voltages. S_R/R^2 as a function of V_G at 30 Hz is shown in Fig. 3.3(a). It is seen that the flicker noise behaves non-monotonically with changing concentration and experiences a maximum on each side of the dependence with respect to the Dirac point. This behaviour will be discussed in more detail below.

Experimentally, it is more convenient to use the lock-in amplifier for noise measurements, although it is a less accurate instrument. In fact, the passband of the lock-in

amplifier is much wider than that of the spectrum analyser, and, therefore, the former does not give a noise value at a particular frequency, but averages the signal over a rather broad frequency range, Sec. 3.2. This averaging introduces an error into the measured value of the noise spectral density, and the size of the error is determined by the particular shape of the lock-in amplifier filters and by the noise dependence on f (the error is minimal if S_R is linear in f, which is clearly not the case for the flicker noise). To test the reliability of the results obtained with the lock-in amplifier, the $S_R/R^2(V_G)$ dependences measured by both instruments under the same experimental conditions on sample FG9C4F1 were compared. Fig. 3.3(a) shows that within the experimental error the lock-in amplifier and the spectrum analyser give identical results, thus, the flicker noise can be reliably measured by the lock-in amplifier.

3.4.2 Flicker noise as a function of gate voltage

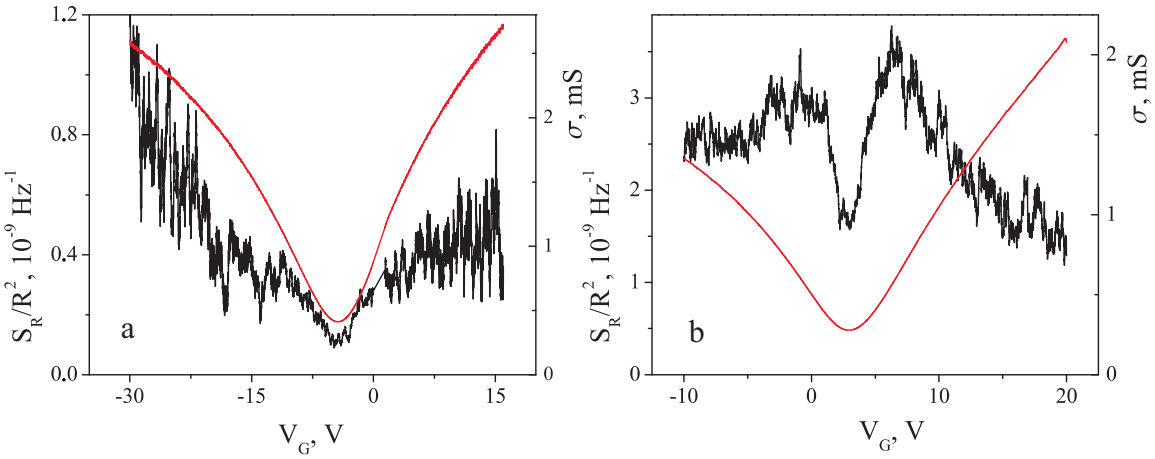

Figure 3.4: The normalised noise spectral density at 30 Hz (black curves) and conductivity, σ, (red curves) as functions of the gate voltage measured in (a) sample G16D3F1 after annealing at 140 °C, and (b) sample RP1.

Flicker noise has been thoroughly investigated in conventional semiconductor devices, where the magnitude of the noise was found to monotonically increase with decreasing carrier concentration [57]. However, our experiments on graphene show drastically different behaviour. At small carrier concentrations, n, the noise magnitude was observed to increase with increasing n, and, therefore, to form a minimum at the Dirac point. At large n the noise either continued to increase, Fig. 3.4(a)*, or

*The unusual behaviour of the noise in sample G16D3F1 around $V_G = 0$ V is explained by a

reached a maximum and, then, decreased with n, Fig. 3.4(b). In this thesis the former type of behaviour will be referred to as V-type behaviour and the latter as M-type behaviour (or V- and M-type samples).

As seen in Fig. 3.4, the conductivity dependences of both samples (red) are quite similar (except for a small difference in their shapes), whereas the noise behaviour (black) significantly differs in both shape and magnitude*. Both samples were measured under similar experimental conditions, which suggests that this difference is caused by intrinsic effects. Furthermore, their mobilities were close to each other and were equal to $\sim 11000\,\mathrm{cm}^2/\mathrm{Vs}$ (mobilities are calculated at room temperature and concentration $n \simeq 10^{12}\,\mathrm{cm}^{-2}$). Mobility is an average property of the carriers in graphene and contains information only about the average strength of the scattering potential. It is impossible to extract from the mobility either the type of the scatterers or their number. This suggests that the scattering potentials may vary from sample to sample, which is also a possible explanation of difference in the noise behaviour in M- and V-type samples. Moreover, in Fig. 3.4 one can notice that the sublinear behaviour of $\sigma(V_G)$ in sample G16D3F1 is much more pronounced than in sample RP1, which can be interpreted as a signature of short-range scattering in sample G16D3F1 [27].

In Si MOSFET structures the flicker noise is associated with random tunneling of electrons between the conductive channel in the Si and nearby impurity states in the SiO_2 [57, 58]. These impurities form the scattering potential for carriers, which determines the conduction through the channel. Therefore, this is an example of a system where the flicker noise and conductance originate from the same source. In this respect graphene is likely to be similar to Si MOSFET structures, since the graphene is supported by SiO_2. Thus, it is reasonable to assume that in graphene there is a direct relation between the shape of the $S_R/R^2(V_G)$ dependence and the type of scattering potential.

The dependence of the flicker noise on the gate voltage can be categorised into two groups: M-type and V-type as seen in Fig. 3.4. For most of the samples the noise

defective voltage source. After switching the polarity the source changed the applied voltage abruptly from 0 V to ~ 1.4 V and continued to increase it. Therefore, to obtain a smooth dependence (both noise and conductivity) the part of the curve had to be shifted in V_G by the same amount. The missing section was filled with a straight line.

*Actually, it is incorrect to compare directly the values of S_R/R^2 of different samples. Instead, the equivalent quantity is $S_R/R^2 \cdot LW$, which is the noise magnitude multiplied by the surface area of the sample. However, the area of sample G16D3F1 is close to that of sample RP1 and, therefore, the comparison without normalisation by the area is valid for these particular samples.

Sample	Mobility, cm^2/Vs	Noise shape p	Noise shape n	Sample	Mobility, cm^2/Vs	Noise shape p	Noise shape n
RP1	10300	M	M	G24D3	5300	V	–
RP1*	5800	V	M	G24D3*	8400	M	M
G16D3F1	5000	M	–	AG1D1F1	6500	M	M
G16D3F1*	11500	V	V	AG1D1F1*	7900	V	M
GB7N4D	12200	M	M	G13DC3F1	14300	M	M
GB7N4D*	10800	V	–	FG10C3F2	4600	M	M
				G24D2	4500	V	V

Table 3.1: Classification of all samples by the shape of their noise dependence on gate voltage. For samples S5, S6* and S7 the shape of the behaviour in the p region was impossible to classify because of the large fluctuations of the noise spectral density during the measurements.

behaviour was found to be different for p- and n-regions, which can be explained by asymmetry in scattering of holes and electrons by the same potential. Therefore, p- and n-regions were categorised independently.

Table 3.1 lists the measured samples in a systematic way, such that the major differences between M- and V-type samples can be compared. As seen from the table, M-type behaviour was mostly exhibited by samples before annealing and was modified into V-type behaviour after annealing, irrespective of the change in mobility. As a typical example, the switching between M- and V-type is shown for sample G16D3F1 in Fig. 3.5(a). Annealing at temperatures above 100 °C is usually associated with the removal of water from the graphene surface. Water molecules adsorb on graphene from the atmosphere during fabrication and affect the scattering of the carriers, which is observed as a change in the $R(V_G)$ dependence of the sample [54, 66–68]. Thus, one can conclude that the M-type behavior of the noise results from the water-like contamination on the surface, while the V-type behaviour comes from defects in graphene or impurities in the SiO_2 substrate which cannot be removed by annealing.

To test the relation between the $S_R/R^2(V_G)$ dependence and the presence of the water contamination on the sample surface, the measurements of the noise were combined with doping by water*. The actual experimental procedure included several steps. First, the sample was annealed at 140 °C in vacuum in order to avoid any contamination from the atmosphere. Atmosphere contamination is mainly from water, however, there is a chance that along with water there are other contaminants, which can be removed by annealing. Then, it was doped with water vapour and the noise

*High purity water was purchased from Sigma Aldrich [48].

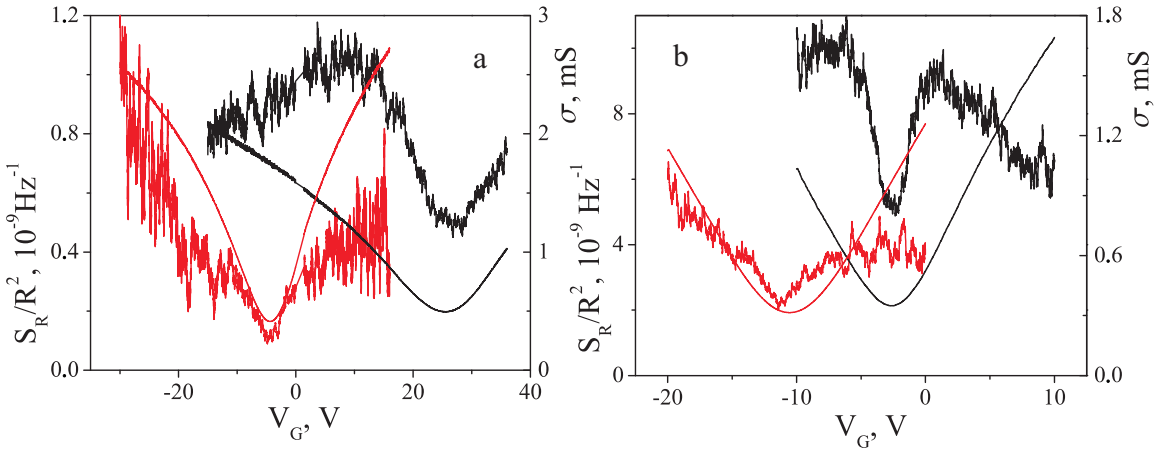

Figure 3.5: (a) $S_R/R^2(V_G)$ and $\sigma(V_G)$ for sample G16D3F1 before (black) and after (red) 140 °C annealing. (b) $S_R/R^2(V_G)$ and $\sigma(V_G)$ for sample GB7N4D after water doping (black) and after 140 °C annealing (red). In (b) noise after annealing is scaled up by a factor of 4.

was measured. Finally, the sample was annealed a second time and the noise measured again. The results are shown in Fig. 3.5(b). It is seen that the water-doped sample exhibited M-type behaviour, which changed to V-type behaviour after annealing at 140 °C. Moreover, the magnitude of the noise changed more than tenfold during annealing, while the conductance changed only by a factor of 2. This indicates two important facts. First, water is a significant source of noise. Second, the flicker noise and conductance are determined by different mechanisms (for this particular sample). Thus, it was shown experimentally that the M-type behaviour of the flicker noise can be attributed to the scattering potential coming from water (or water-like) impurities, whereas V-type behaviour can be associated with defects from SiO_2 or graphene itself, which cannotbe removed by 140 °C annealing.

3.4.3 A simple theoretical model

The relation between the M-type behaviour of the flicker noise and the presence of water molecules on the sample surface has been experimentally established in the previous section. However, in order to understand the mechanism that underlies this relation, one needs to consider a simple theoretical model within a framework of the Drude formula for the resistance of graphene*. The resistance is a function of carrier concen-

*One should note that the Drude formula is not applicable in the vicinity of the Dirac point due to vanishing density of states, and the theoretical model for noise has the same region of applicability.

tration, n, and mobility, μ. Mobility, in turn, is determined by the concentration of the scatterers, N, and the carrier concentration, n. Therefore, the resistance, as well as the resistance fluctuations δR, can be considered as a function of n and N. Then, δR reads

$$\delta R(n, N) = \frac{\partial R}{\partial n}\delta n + \frac{\partial R}{\partial N}\delta N, \tag{3.1}$$

where δn and δN are fluctuations of n and N, respectively. The noise spectral density S_R is proportional to $(\delta R)^2$ and, therefore, is given by

$$S_R \propto (\delta R)^2 = \left(\frac{\partial R}{\partial n}\delta n\right)^2 + 2\frac{\partial R}{\partial n}\frac{\partial R}{\partial N}\delta n\delta N + \left(\frac{\partial R}{\partial N}\delta N\right)^2. \tag{3.2}$$

One can see from Eq. 3.1 that, formally, there are two contributions to the noise. The first contribution is coming from the dependence of the resistance on n, and, therefore, represents the fluctuations associated with changing n. In this thesis it will be referred to as the concentration contribution*. The second contribution is determined by the dependence of R on N, and is attributed to the fluctuation in the number of scatterers (impurities). This contribution will be referred to as the impurity contribution.

If concentration fluctuations and impurity fluctuations are correlated, then the second term in Eq. 3.2 does not vanish after averaging, and both contributions have to be considered together. An example of a physical process where the changes in n and N depend on each other, is a trapping of the channel carriers in SiO_2. Electrons randomly tunnel between the conductor and the trap states causing fluctuations in both n (number of carriers in the channel is changed by 1 in a single tunneling event) and N (electron tunnels to the positively charged trap and neutralises it, which also changes N by 1). The multipliers $(\delta n)^2$, $(\delta N)^2$ and $(\delta n\delta N)$ are independent of n and, in the case of an exponentially broad distribution of the characteristic times of the tunneling events, give a $1/f$ scaling with frequency after averaging over all possible fluctuations, Sec. 3.5.2.

The function $\partial R/\partial n$ can be deduced from the $R(V_G)$ dependence, since the relation between n and V_G is known, Sec. 1.2.2. In fact, sweeping the gate voltage changes only the concentration of carriers and keeps the number of scatterers constant, and,

*In the literature, a similar contribution was often referred to as the concentration contribution, although the resistance was assumed to be a function of (n, μ) instead of (n, N). The difference between the two is more mathematical than physical and does not change either the logic of the derivations or the conclusions.

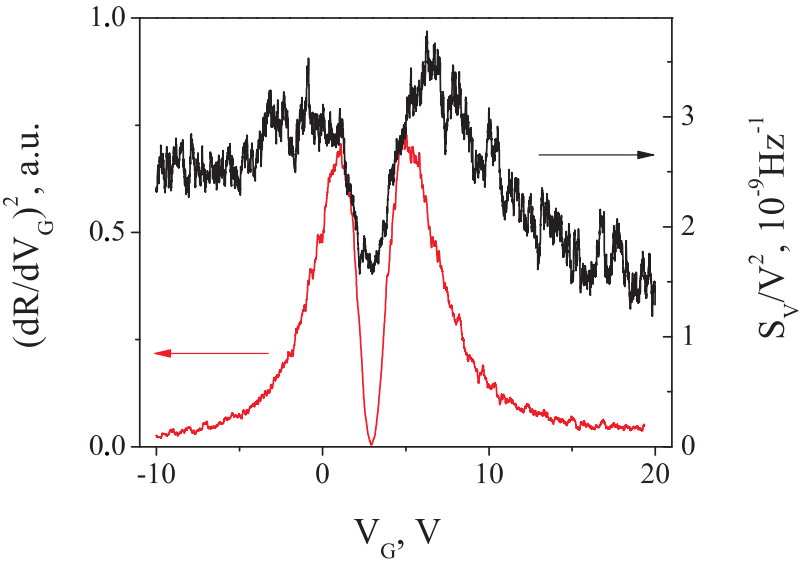

Figure 3.6: The normalised resistance derivative, $(dR/dV_G)^2/R^2$ (red curve), and measured noise, S_R/R^2 (black curve), are shown as functions of the gate voltage for sample RP1.

therefore, the partial derivative $\partial R/\partial n$ can be obtained from the full derivative of the resistance with respect to V_G. Finally, the multiplier $\partial R/\partial N$ from the impurity contribution is deduced from the particular model of the scattering potential and will be discussed later.

In Fig. 3.6 the concentration contribution, $(dR/dV_G)^2/R^2$, and the measured noise are shown. At first, one can see that the shapes of both curves are alike (which is true only for M-type samples), although there are significant differences in the behaviour. Namely, while the value of the derivative is zero at the Dirac point (simply because of the maximum in the $R(V_G)$ dependence), the measured noise exhibits a finite value. Also, the maxima in the $(dR/dV_G)^2/R^2$ dependence always occur within ± 7 V range from the Dirac point, whereas the maxima in noise can appear 20 V away from this point, Fig. 3.5(a). Thus, the measured behaviour of the flicker noise cannot be fitted by the concentration contribution alone, which points out the importance of the impurity contribution, especially for V-type samples, in which the maxima in $(dR/dV_G)^2/R^2$ do not even occur.

The impurity contribution to the flicker noise is given by the dependence of R on N, which, in turn, is determined by the dominant scattering mechanism. Here, two types of scatterers will be considered: short-range and long-range impurities. All the other known types of scatterers result in $R(n)$ dependences similar to that for

either short- or long-range impurities, Sec. 1.3.2. It is known that the long-range scattering potential results in a graphene resistance which is inversely proportional to the carrier concentration [28], while the short-range potential gives a resistance which is independent of concentration [7]. In both cases the resistance is proportional to N, such that the derivative $\partial R/\partial N$ has the same functional dependence on n as the corresponding contribution to the resistance. In general, both types of scatterers are present in the sample, although it is possible that one of them prevails over the other. Also, as was shown experimentally in Sec. 3.4.2, the mechanisms that determine the resistance and noise can be unrelated. For instance, if the resistance is given by a long-range scattering mechanism, but the noise is coming from a short-range mechanism, then the impurity contribution to the noise, S_{imp}, reads as

$$\frac{S_{imp}}{R^2} \propto \left(\frac{\delta R_{srs}}{R_{lrs}}\right)^2 = \left(\frac{\partial R_{srs}}{\partial N_{srs}}\delta N\right)^2 \frac{1}{R_{lrs}^2} \propto n^2. \tag{3.3}$$

In the opposite case, if long-range scatterers are the source of the noise, and the resistance is determined by short-range scatterers, the impurity contribution has the form

$$\frac{S_{imp}}{R^2} \propto \left(\frac{\delta R_{lrs}}{R_{srs}}\right)^2 = \left(\frac{\partial R_{lrs}}{\partial N_{lrs}}\delta N\right)^2 \frac{1}{R_{srs}^2} \propto \frac{1}{n^2}. \tag{3.4}$$

These two extreme cases show, first, that the behaviour of the noise is crucially dependent on the details of the scattering potential, and, second, that various behaviours (including M-type and V-type) can be explained by the interplay between long- and short-range scatterers.

In a more realistic case, where the resistance is determined by both mechanisms, yet the noise is given by the short-range potential only, the impurity contribution reads as

$$\frac{S_{imp}}{R^2} \propto \frac{1}{(R(V_G))^2} \propto (\sigma(V_G))^2. \tag{3.5}$$

This equation implies the proportionality between the noise magnitude and the squared conductance. Fig. 3.7(a) shows the measured S_R/R^2 as a function of σ^2. It is seen that away from the Dirac point (where the Drude formula is applicable) the straight line fits the measured dependence well. Therefore, in this particular sample Eq. 3.5 is obeyed, which suggests that the source of the V-type noise dependence is a short-range disorder.

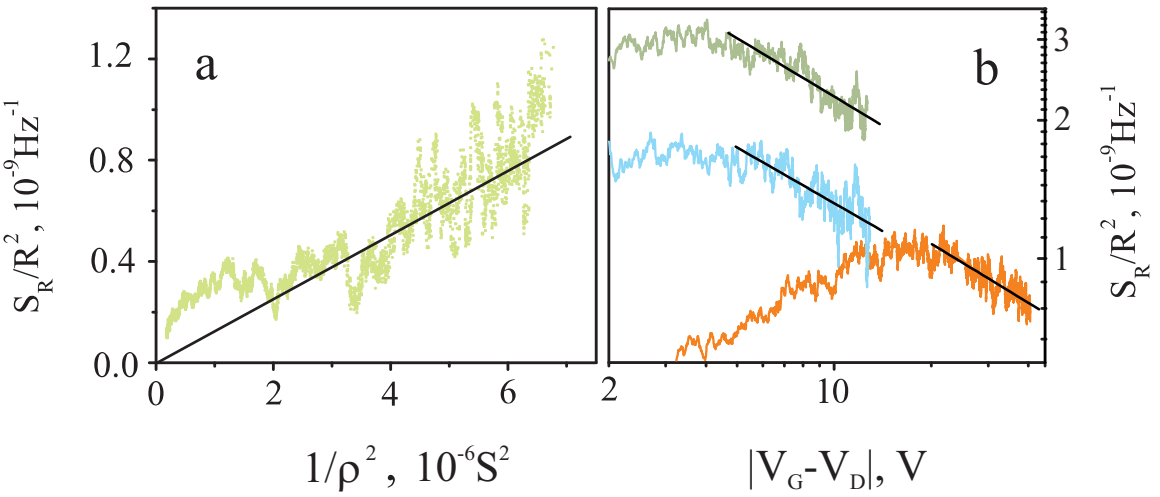

Figure 3.7: (a) Normalised noise as a function of $1/R^2 \propto \sigma^2$. The straight line shows the fit by Eq. 3.5. (b) S_R/R^2 as a function of $|V_G - V_D|$ for three different samples in logarithmic scale. The fit $S_R/R^2 \propto n^{-0.4}$ is shown as straight lines.

In Fig. 3.7(b) S_R/R^2 for three different M-type samples is shown as a function of $|V_G - V_D|$ (where V_D is the Dirac point position). One can see that the noise dependences can be fitted with a power low dependence $n^{-0.4}$. The fitting was accomplished in a very limited range of V_G and, therefore, is not reliable. However, since the noise magnitude at large carrier concentrations decreases with n, it still suggests that the M-type noise behaviour is more likely to be explained by the long-range scattering potential rather than short-range, Eqs. 3.4 and 3.3.

In conclusion, using the simple theory described above it has been demonstrated that the V-type and M-type noise behaviours can be explained by the interplay between fluctuating short-range and long-range scattering potentials. Annealing of the sample was found to change the behaviour of the noise from M-type to V-type and, therefore, change the dominant fluctuating scattering mechanism. Doping by water was shown to increase the noise by an order of magnitude, and yet to have almost no effect on the mobility. This means that scattering potentials which determine noise and resistance, can be uncorrelated. Moreover, the samples after doping by water exhibited M-type noise behaviour, further demonstrating that the water is a source of fluctuating long-range potential. It is also worth noting that the results on the water doping discussed in Sec. 2.4 agrees with the measurement presented in this chapter. In particular, the hysteresis appearing after water doping is seen in both $R(V_G)$ and noise dependences, although it is not shown in this chapter as the sweeps only in one direction are shown.

3.5 Temperature dependence of the flicker noise

3.5.1 Experimental results

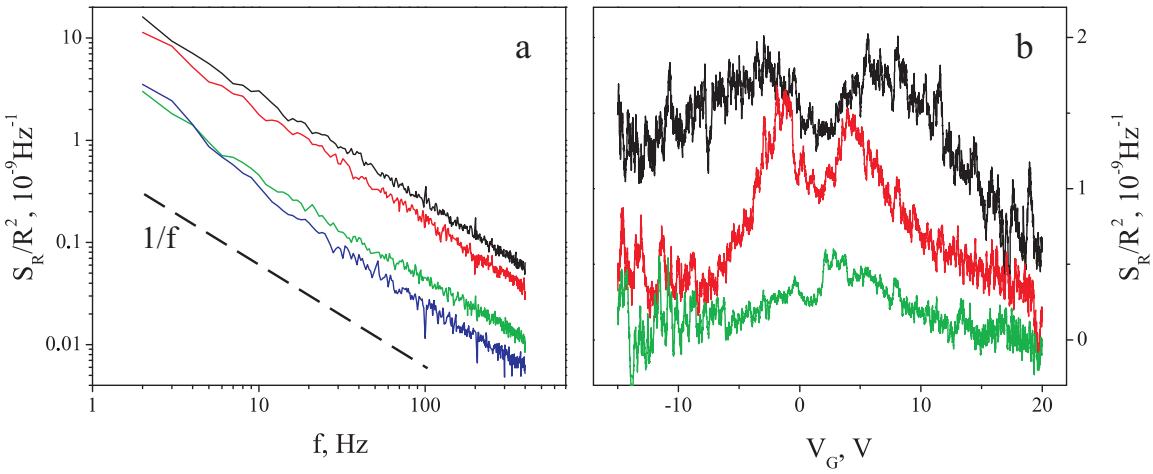

Figure 3.8: (a) Normalised noise spectra for sample G24D3 measured at different temperatures. From top to bottom: 220 K, 100 K, 60 K and 25 K, $V_G = -15$ V. $1/f$ dependence is given as a dashed line. (b) S_R/R^2 as a function of the gate voltage at 30 Hz for sample G24D3 at temperatures 220 K, 100 K and 60 K (from top to bottom). Dirac point position is about 2.5 V.

One of the possible origins of the flicker noise in graphene is switching of the electron position between the conductive channel in the graphene flake and impurity states in the SiO_2 substrate or absorbed surface molecules. The switching process can be either resonant tunneling through a barrier, or hopping caused by a thermal fluctuations, or some mixture of the two. The particular mechanism of the electron jumps can be deduced from the temperature dependence of the flicker noise, since the tunneling is independent of the temperature, while the hopping is a thermally activated process. In this section the measurements of the low-frequency noise in the temperature range from 20 K to 300 K will be presented and the possible explanation of the noise behaviour will be discussed.

Fig. 3.8(a) shows the normalised noise spectra at different temperatures for sample G24D3. One can see that the $1/f$ scaling of the low-frequency noise is preserved at all temperatures, although at 25 K the spectrum starts to deviate at frequencies under ~ 20 Hz (the blue curve in the figure). This deviation is a signature of the splitting of the spectrum into a set of lorentzians (each lorentzian corresponds to an individual fluctuator, Sec. 1.4.2), and will be discussed in Sec. 3.6.

Dependences of the noise magnitude on the gate voltage at different temperatures are shown in Fig. 3.8(b) for the same sample as in panel (a). At the highest temperature (220 K, black curve) the sample is seen to exhibit the M-type behaviour which is preserved also at 100 K. However, at 60 K the maxima are no longer clearly observed. This dramatic difference between the noise dependences at 60 K and 100 K suggests that the M-type behaviour is determined by the thermally activated mechanism. Fig. 3.8(a) confirms this interpretation as the noise magnitude significantly increases from 60 K to 100 K. In order to understand which mechanisms can introduce such a temperature dependence the following theoretical model will be considered.

3.5.2 Theoretical description of the temperature dependence of flicker noise

In Ref. [34] a unified model of the flicker noise in MOSFET structures was considered. Here, a similar theoretical analysis for graphene will be described. As seen in Sec. 3.4.3, the fluctuations of the resistance can be presented through the partial derivatives with respect to the concentrations of carriers and impurities. Assuming that the traps in SiO_2 are the main source of fluctuations one can conclude that the fluctuations δn and δN are no longer unrelated, since a single jump of the electron between trap and graphene involves both changes in n and N.

For convenience, the function that determines the relation between δn and δN is defined as β:

$$\delta n = \beta \delta N. \tag{3.6}$$

In general, β is a function of temperature and both n and N; in the literature on MOSFETs it is referred to as a coupling coefficient. This coefficient basically gives the change in the carrier concentration if the number of scatterers is changed by 1. In our case, it is reasonable to assume that β is virtually equal to ± 1 depending on the charge of the trap when its electronic state is filled. For example, if an unoccupied trap is neutral, then the jump of the electron on to the trap decreases the carrier concentration by unity, $\delta n = -1$, and increases the number of scatterers by unity, $\delta N = 1$. Therefore, $\beta = \delta n / \delta N = -1$. However, for now β shall be left in the equation.

After substitution of β into Eq. 3.2 $(\delta R)^2$ reads

$$(\delta R)^2 = \left(\frac{\partial R}{\partial n}\beta + \frac{\partial R}{\partial N}\right)^2 (\delta N)^2 . \tag{3.7}$$

This equation gives the contribution to the noise from a singe fluctuating trap state, and in order to deduce the full noise spectral density one needs to integrate the equation over all the states:

$$S_R = \left(\frac{\partial R}{\partial n}\beta + \frac{\partial R}{\partial N}\right)^2 S_N, \tag{3.8}$$

where S_N is the spectral density of the fluctuations in N and is given by the integral [34]

$$S_N = \frac{1}{W^2 L^2}\int_{E_v}^{E_c} dE \int_0^W dy \int_0^L dx \int_0^D dz\, 4N(E,x,y,z) f(1-f)\cdot \\ \frac{\tau(E,x,y,z)}{1+\omega^2\tau^2(E,x,y,z)}. \tag{3.9}$$

Here $N(E,x,y,z)$ is a distribution of the scatterers' states in space and energy; the integral is taken over the whole volume of the dielectric substrate underneath the graphene flake, so that W and L are the width and the length of the sample, respectively, and D is the thickness of the oxide (300 nm); E_V and E_C are the boundaries of the bandgap in SiO_2; $\tau(E,x,y,z)$ is a characteristic time of the fluctuation; $f = (1+\exp((E-E_F)/kT))^{-1}$ is the occupancy function of the scatterer state and E_F is the Fermi level in graphene.

For simplicity, it is assumed that the scatterer's states are distributed uniformly over the oxide in both space and energy domains. Also, taking into account that $f(1-f)$ is essentially a delta function around the Fermi level, one can rewrite the integral as follows

$$S_N = \frac{kT}{W^2 L^2}\int_0^W dy \int_0^L dx \int_0^D dz \left(4N(E_F,x,y,z)\frac{\tau(E_F,x,y,z)}{1+\omega^2\tau^2(E_F,x,y,z)}\right). \tag{3.10}$$

Here, it is seen that the noise magnitude is proportional to the temperature. However, the actual mechanism of the electron switching between graphene and impurities can also be dependent on T and is hidden in the characteristic time. For the resonant tunneling mechanism τ is temperature independent, and integration over the oxide thickness results in a $1/f$ dependence of the noise magnitude. However, if the switch-

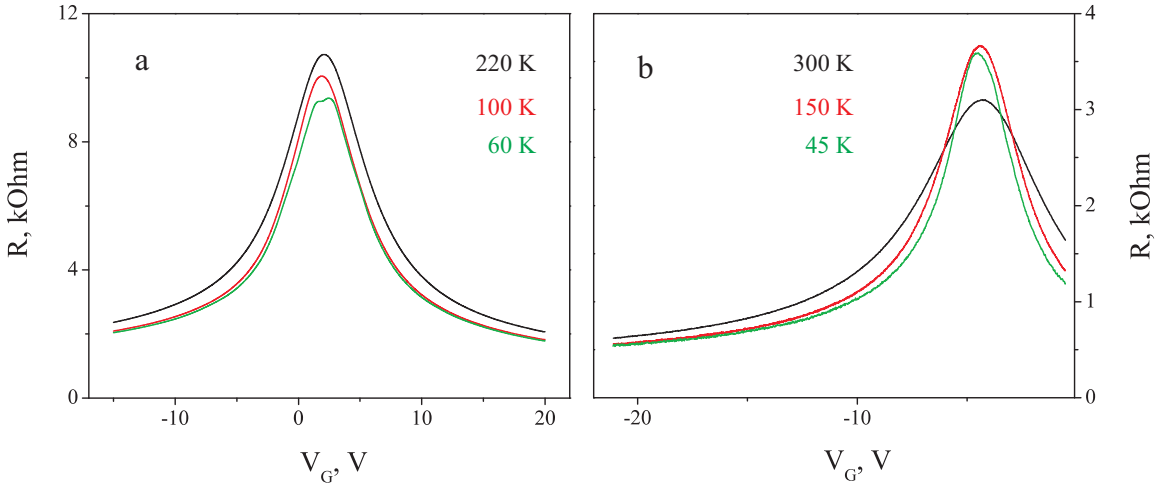

Figure 3.9: $R(V_G)$ dependences for (a) sample D24D3 at temperatures 220 K (black), 100 K (red), 60 K (green), and (b) sample G16D3F1 at temperatures 300 K (black), 150 K (red), 45 K (green).

ing is determined by thermal hopping, then the integration over all possible hopping pathways (with different heights of the energy barrier) gives an additional power in the T dependence along with a $1/f$ scaling, so that $S_N \propto T^2/f$.

Now it is clear that there are three points in Eq. 3.8 where the temperature dependence enters the expression for noise. First, the multiplier kT comes from the integration over the bandgap and represents the fact that the number of active traps is proportional to T, Eq. 3.10. Second, for the case of thermal hopping a multiplier of T/f appears due to the averaging over various barrier heights. Finally, the resistance itself can depend on T, which leads to temperature-dependent derivatives $\partial R/\partial n$ and $\partial R/\partial N$. Theoretically, the latter one can be determined by several mechanisms. It can come from phonons, which results in $R_{ph} \propto T$. Also, screening of charged scatterers by transport electrons can depend on T resulting in temperature-dependent scattering. In addition, $R(T)$ dependence comes from the thermal excitation of the carriers, when the Fermi energy is less than kT (close to the Dirac point) [69].

To estimate the temperature-dependent contribution to the resistance experimentally, $R(V_G)$ dependences were measured at different T, Fig. 3.9. In panel (a) it is seen that at all gate voltages the resistance increases with temperature, which suggests phonons as a main temperature-dependent contribution. In panel (b) one can see a similar behaviour at large V_G, yet near the Dirac point the transport is determined by thermally excited carriers (increase of R with decreasing T). All the samples that

have been measured can be ascribed to either of the two types of $R(T)$ dependences presented in Fig. 3.9, and in both types the change in the resistance does not exceed 15 %. This means that the change in the normalised noise due to these mechanisms is less than 60 %*, which suggests that $S_R(T)$ cannot be explained by this contribution alone. It is also confirmed by the fact that no correlation between the $R(T)$ behaviour and the noise behaviour (M- or V-type) was found in our samples.

In principle, one can try to exclude the linear contribution ($\propto kT$) by dividing the measured noise dependences by temperature. However, the obtained results do not fall onto one curve and do not reveal any simple dependence on T. Further work needs to be done on this subject.

3.5.3 An example of fitting M-type dependence of the noise

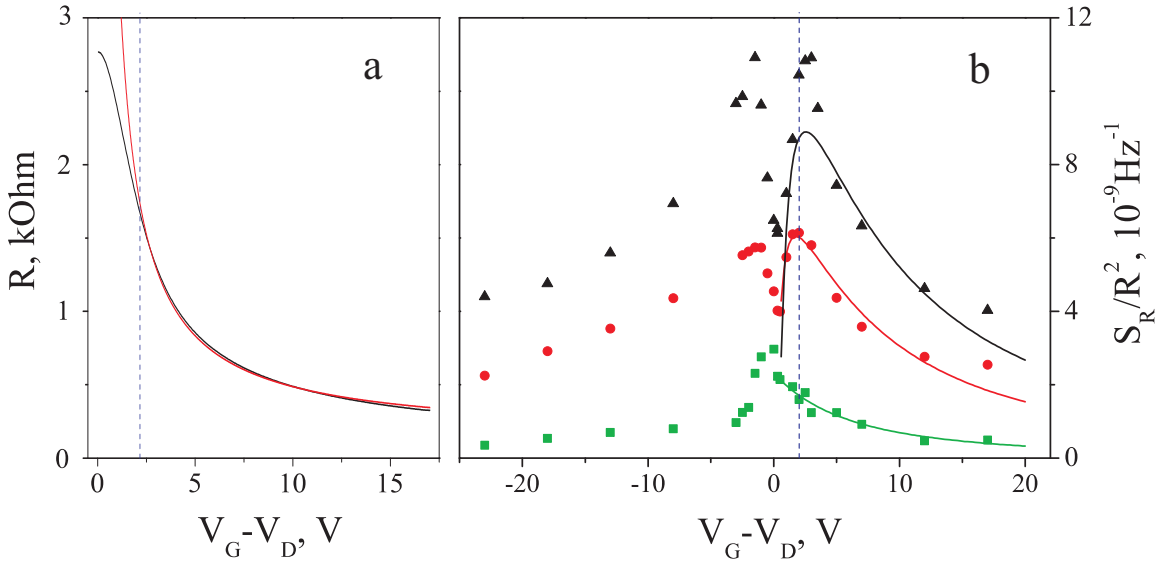

Figure 3.10: (a) Resistance as a function of $V_G - V_D$ (V_D is the position of the Dirac point) for sample SL6 (black). Red curve shows the fit of the resistance by Eq. 3.11 in the range limited by the dashed line. (b) Measured S_R/R^2 dependences on $V_G - V_D$ for sample SL6 at temperatures 140 K (black points), 100 K (red points) and 60 K (green points). Analytical fit of the noise to Eq. 3.12 is shown by lines.

As was mentioned in Sec. 3.4.3, the interplay between long- and short-range scattering mechanisms can explain various noise behaviours, and in this subsection an example of the fit of M-type dependence will be discussed. A model for the $R(V_G)$ (or equivalently $R(n)$) dependence is required in order to extract from it the first factor in

*$S_R/R^2 \propto (\partial R/\partial n\beta + \partial R/\partial N)^2/R^2$.

T,K	A,a.u.	B,a.u.	C,a.u.	D,a.u.
60	3.82	45.8	$3.15 \cdot 10^{-14}$	12500
100	3.59	48.6	$3.14 \cdot 10^{-10}$	258
140	3.78	51.8	$2.00 \cdot 10^{-9}$	150

Table 3.2: The values of the fitting parameters used in Fig. 3.10. The fitting formulas for resistance and noise are $R = A + B/V_G$ and $S_R/R^2 = C(-B/V_G + D)^2/(AV_G + B)^2$. Therefore for the parameters used in Eqs. 3.11 and 3.12 we have $\gamma \propto A$, $\kappa N \propto B$, $S_N \propto C$ and $N\beta \propto 1/D$.

Eq. 3.8. The most common way to describe the graphene resistance in the presence of both types of scatterers is to use the Matthiessen rule, Sec. 1.3.2,

$$R = \frac{L}{W}\frac{1}{ne\mu} = \frac{L}{W}\frac{1}{ne}\left(\frac{1}{\mu_{srs}} + \frac{1}{\mu_{lrs}}\right) = \frac{L}{W}\frac{1}{ne}(\kappa N + \gamma n), \tag{3.11}$$

where κ and γ are parameters, assumed here to be independent of both N and n, although they can be functions of T. After substituting this expression for the resistance into Eq. 3.8 the normalised noise reads

$$\frac{S_R}{R^2} = \left(-\frac{L\kappa N}{Wn^2e}\beta + \frac{L\kappa}{Wne}\right)\frac{S_N}{\left(\frac{L\kappa N}{Wne} + \frac{L\gamma}{We}\right)^2} = S_N\kappa^2\frac{\left(-\frac{N}{n}\beta + 1\right)^2}{(\kappa N + \gamma n)^2}. \tag{3.12}$$

Eqs. 3.11 and 3.12 can be used to fit independently the $R(V_G)$ and $S_R/R^2(V_G)$ dependences, where the fitting parameters are S_N, κ, N and γ ($\beta = \pm 1$).

The fitting procedure is the following. Firstly, the resistance dependence on the gate voltage was fitted with Eq. 3.11 and the parameters κN^* and γ were found for each given temperature†, Fig. 3.10(a). Found parameters were substituted into Eq. 3.12 and, then, the equation (separate equation for each T) was used to fit the noise dependences with parameters S_N and κ (or N). As a result, the whole set of parameters at all temperatures was obtained. In Fig. 3.10(b) it is seen that the peculiar transition of the noise dependence from M-type at 140 K to peak-type at 60 K can be mimicked by our fitting equations. (Noise dependence that has a shape of a single peak is referred to as a peak-type dependence.) However, the main fitting feature of the noise reveals itself at the edge of the fitting range, which makes the fit unreliable. Moreover, the

*Resistance depends on the product of κN, which makes it impossible to determine these parameters separately from fitting $R(V_G)$ only.

†The change of $R(V_G)$ with T for this particular sample was negligible, which results in almost T-independent parameters κN and γ.

actual parameters have to be temperature dependent in order to result in the shown analytical noise behaviour. Namely, κ was found to increase with decreasing T, while κN was almost temperature independent, such that N must increase with T. It was found not to be possible to ascribe the obtained $\kappa(T)$ and $N(T)$ functions to any of the known physical mechanisms. This diminishes the reliability of the described fit even further.

Thus, it has been shown that the M-type noise dependence can be mimicked analytically, although the produced fit cannot be used for a strict and concise description of the flicker noise behavior in graphene.

3.6 Random telegraph signals (RTS) in graphene nanoribbon

3.6.1 $1/f$ spectra as a sum of lorentzians

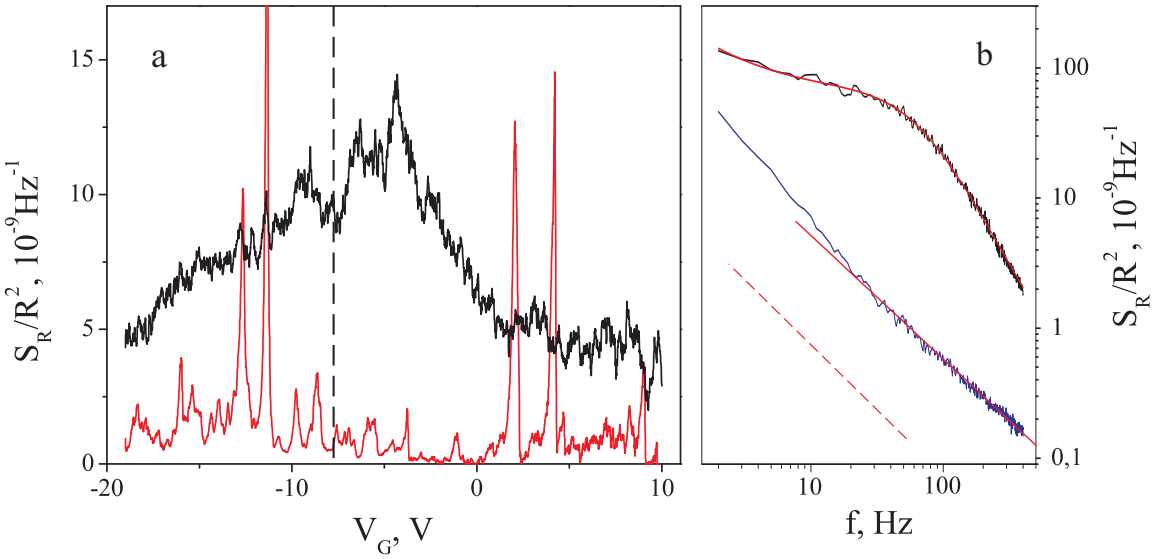

Figure 3.11: (a) S_R/R^2 as a function of the gate voltage at 115 K (black) and 8 K (red) at 30 Hz for sample FG9C4F1. The position of the Dirac point is shown by a dashed line. (b) Normalised noise spectra at 8 K for two gate voltages -6.7 V (black) and -4.7 V (blue). The black dependence is fitted by the sum of $1/f$ noise and a single lorentzian. The blue dependence is fitted with $1/f^{\alpha}$ ($\alpha \simeq 0.94$). Red dashed line shows $1/f$ scaling.

At high enough temperatures, the distribution of the impurity states, which determines the noise, is effectively uniform in energy due to the fact that the energy

difference between adjacent levels is much smaller than kT. In contrast, at low T (below $\sim 20\,\mathrm{K}$) the noise dependence on the gate voltage reveals individual fluctuating occupancies of the electron states, which significantly distorts the $1/f$ dependence of the noise spectrum.

In Fig. 3.11(a) S_R/R^2 is shown as a function of V_G at 30 Hz for sample FG9C4F1 at two temperatures above and below the threshold. (At the threshold temperature the noise spectrum is split into individual lorentzians.). It is seen that at 115 K the noise changes gradually with V_G, while at 8 K it exhibits sharp peaks on top of a negligible background. Moreover, while the noise spectra at 115 K were found to obey $1/f$ scaling (not shown, but in principle one can produce a similar picture to Fig. 3.2), a clear signature of the presence of lorentzian contribution to the noise can be seen at 8 K, Fig. 3.11(b). In the middle between the fluctuating states, the noise behaviour is still close to the flicker noise, whereas when the Fermi level is near such a state, the noise spectrum can be fitted with combined single lorentzian and $1/f$ dependences.

It is worth noting that the width of sample FG9C4F1 was $\sim 250\,\mathrm{nm}$, which makes the transport through such a narrow graphene nanoribbon very sensitive to the scattering by nearby impurities. Therefore, fluctuations in the scattering potential causes significant fluctuations of the sample resistance which, thus, can be observed experimentally as will be shown in the next subsection.

3.6.2 RTS time dependence

RTS is usually seen as a switching of a physical parameter (for example, resistance) between two values, which correspond to two metastable states of the system. The most powerful method of studying this switching is to measure the time dependence of the parameter. In conventional semiconductor structures it was found that RTS time dependences contain information about the fluctuating states including their spatial position and the mechanism of the fluctuations (thermal hopping or resonant tunneling) [58]. Therefore, RTS in graphene can also help to understand the origin of the fluctuations, and to explain the temperature dependence of the flicker noise.

In Fig. 3.12 the time dependences of the voltage drop (which is proportional to the sample resistance) are shown at different positions of the Fermi level in graphene. It is seen that the sample switches with time between two states: high resistance “up” state

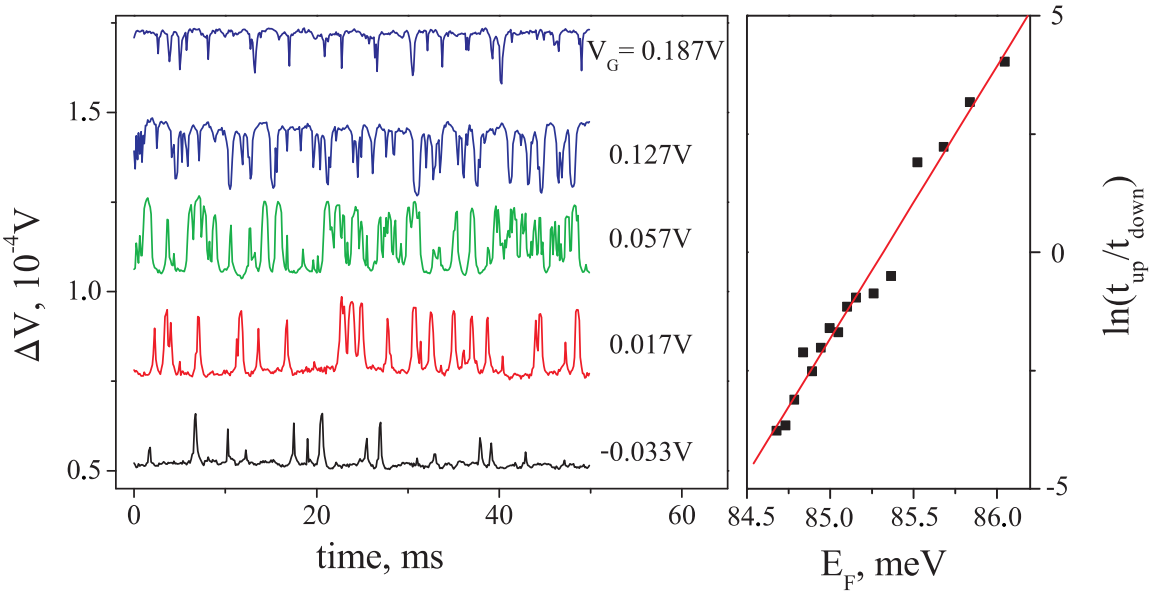

Figure 3.12: Left: voltage drop across the sample FG9C4F1 as a function of time (constant DC current regime) at different gate voltages. Temperature is 8 K. Dependences at different V_G are shifted vertically. Right: logarithm of the ratio t_{up}/t_{down} as a function of the Fermi energy in graphene. Red line shows a linear fit.

and low resistance "down" state. With changing gate voltage one changes the relative positions of the Fermi level in graphene and the impurity level. In turn, the probability for the electron to be either on the impurity level or in the conductive channel also changes. For instance, if E_F is above the impurity energy level, E_t, then with a high probability the trap state will be occupied. Therefore, the time which the electron spends on the trap level, t_{up}, is larger than that which it spends in the channel, t_{down}. Vice versa, if E_F is below the trap energy level, then the low resistive state ("down" state) is more probable.

For the system switching between two metastable states it is known that [58]

$$\frac{t_{up}}{t_{down}} = exp\left(\frac{E_t - E_F}{kT}\right). \tag{3.13}$$

Therefore, assuming that E_t is independent of E_F the plot of $\ln(t_{up}/t_{down})$ versus E_F has to give a straight line, as it is seen in Fig. 3.12(right). (The values of t_{up} and t_{down} were obtained by averaging the time which system spends in "up" and "down" states, respectively.) At the point where $\ln(t_{up}/t_{down}) = 0$ (at this position of E_F system spends equal amount of time in both states) the energy levels E_t and E_F coincide. Thus, E_t can be estimated as $\simeq 85.3$ meV. This estimate is quite accurate, although

the position of the impurity level depends on E_F, and can change by $\sim 10\,\mathrm{meV}$ over the range of E_F, Fig. 3.12.

It is possible to determine which state of the impurity (occupied or unoccupied) causes more scattering in the channel. Considering the example from Fig. 3.12, the "up" state of the system is more resistive, which means that the occupied state of the impurity results in a higher scattering rate rather than the unoccupied state. Assuming that in one of the states the impurity is neutral, one can conclude that in the "up" state it is negatively charged and in the "down" state it is neutral. On sample FG9C4F1 three different RTS were measured and analysed. Two of them were of the kind described above and the other one was of the opposite charge, which suggests that impurities of both signs of the charge are present.

In Fig. 3.12(right) the dependence $\ln(t_{up}/t_{down})(E_F)$ was fitted by a straight line. However, the fit range of the energies is small in comparison to its absolute value, which means that the fit cannotconfirm the linear dependence between the logarithm and the Fermi energy. Furthermore, from the slope of the fit one can deduce the temperature of the system, although obtained estimate $T \simeq 2\,\mathrm{K}$ is 4 times smaller than the value measured directly by the sensor. Thus, in order to describe the measured RTS correctly, the dependence between E_t and E_F has to be taken into account.

Most likely, the impurity states involved in the RTS are situated inside the bulk of SiO_2 [10]. Therefore, the applied voltage between the gate and the graphene flake shifts all the energy states inside the SiO_2 with respect to the Fermi energy in the graphene in proportionality to the distance between the position of the impurity and the graphene, Fig. 3.13. For example, when V_G is shifted up by ΔV_G, the energy level of the impurity is also shifted up by $\Delta E_t = e\Delta V_G \cdot l/D$. At the same time the Fermi energy in graphene is changed by $\Delta E_F = 0.03 \cdot \Delta(\sqrt{|V_G - V_D|})\,\mathrm{eV}$. Therefore the actual change in the energy difference $E_t - E_F$ is

$$\Delta(E_t - E_F) = e\Delta V_G \cdot l/D - 0.03 \cdot \Delta(\sqrt{|V_G - V_D|}). \tag{3.14}$$

Then, the actual dependence of the energy difference on the gate voltage reads

$$E_t - E_F = E_0 + eV_G \cdot l/D - 0.03 \cdot (\sqrt{|V_G - V_D|}), \tag{3.15}$$

where E_0 is a constant.

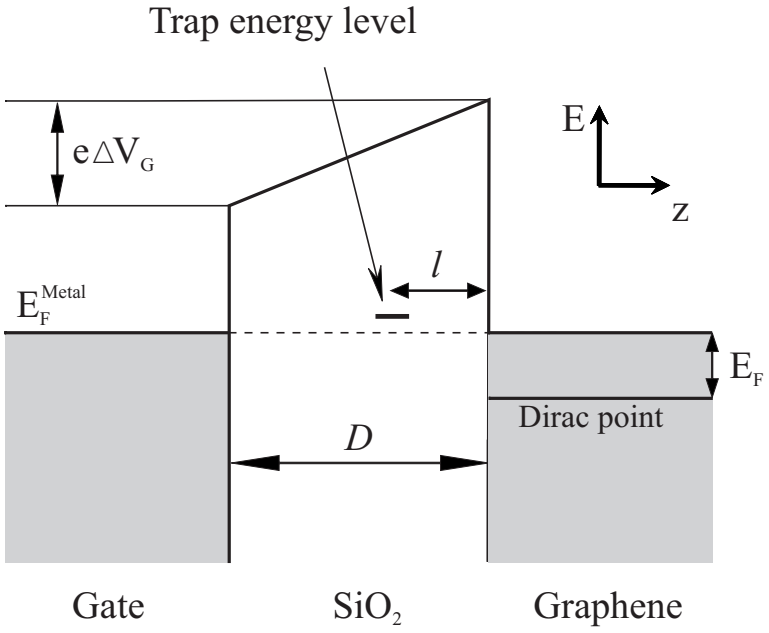

Figure 3.13: The relative position of the trap energy level, E_t, with respect to the Fermi level, E_F, in graphene is shown when V_G is applied.

To find the expression for the slope in Fig. 3.12(right) one needs to calculate the derivative of Eq. 3.13 with respect to the Fermi energy

$$\frac{d}{dE_F}\left(\ln\frac{t_{up}}{t_{down}}\right) = \frac{1}{kT}\frac{d}{dE_F}(eV_G \cdot l/D - 0.03 \cdot (\sqrt{|V_G - V_D|})). \tag{3.16}$$

Knowing that $V_G = V_D + (E_F/0.03)^2$ the derivative can be rewritten as follows

$$\frac{d}{dE_F}\left(\ln\frac{t_{up}}{t_{down}}\right) = \frac{1}{kT}(e\frac{d}{l}2\frac{E_F/eV}{0.03^2} - 1). \tag{3.17}$$

Thus, taking an average value of the Fermi energy, $E_F \simeq 85.3\,\text{meV}$, and knowing the temperature and SiO_2 thickness, $D = 300\,\text{nm}$, one can evaluate the distance l between the trap and the graphene flake to be about 8 nm.

It is known that tunneling that results in observable effects usually happens at distances of the order of 1 nm, which is much smaller than what was extracted from our experiments. This suggests that the most probable mechanism of the RTS in the graphene sample studied here is thermal hopping. For thermal hopping the characteristic time t^* is expected to be exponentially dependent on T as in a temperature-activated

*Characteristic time is determined as an average time between two successive switchings from the "down" state to the "up" state.

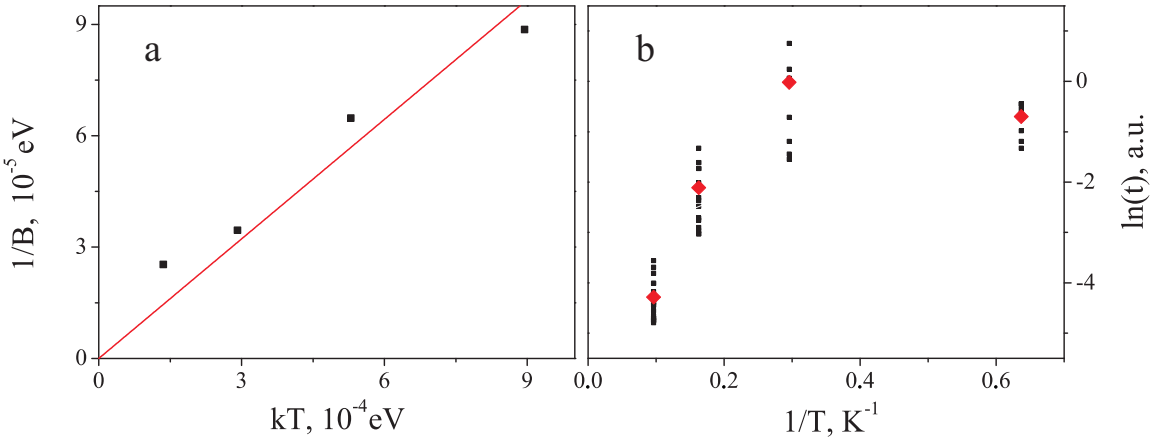

Figure 3.14: (a) Inverted derivative $1/B \equiv 1/\left(\frac{d}{dE_F}\left(\ln\frac{t_{up}}{t_{down}}\right)\right)$ as a function of temperature for a trap near the Fermi energy $E_F \simeq 50\,\text{meV}$. Red line shows the linear fit, $B \simeq 9.3/(kT/eV)$. (b) Logarithm of the characteristic time t of the trap as a function of the inverted temperature. Groups of black points represent estimated t at different relative positions of the Fermi level and the trap level. Red points are averages of the corresponding groups.

process. To test this dependence the following experiment was performed.

Firstly, it was confirmed that the observed RTS can consistently be described by Eqs. 3.13-3.17 at all given temperatures. Namely, the slope B of the dependence $\ln(t_{up}/t_{down})(E_F)$ was deduced (the same analysis as for Fig. 3.12) and, then, $1/B$ was plotted as a function of kT, Fig. 3.14(a). From a linear fit of the dependence of $1/B$ on temperature the distance between the impurity and the graphene flake was found to be $\sim 30\,\text{nm}$. The fact that the relation between $1/B$ and T is linear confirms the applicability of Eq. 3.17.

Secondly, the characteristic time t was obtained from averaging the time between two subsequent transitions from the "up" state to the "down" state for each measured RTS time dependence. The results are shown in Fig. 3.14(b) for different temperatures. Due to the small number of observed periods in a single measurement (usually $10-20$ periods), the error of the values of t is rather large, which is seen as groups of points corresponding to a single value of t. One can see that at higher temperatures (small $1/T$) t depends on temperature linearly (although the actual form of the dependence cannotbe deduced due to the small number of points and large error), while at small T (high $1/T$) it is roughly independent of temperature. This suggests that the actual mechanism of fluctuations is a combination of tunneling and thermal activation. At small temperatures, up to $\sim 3\,\text{K}$, the electron jumps are determined by resonant tun-

neling and are temperature-independent. At high T, thermal activation starts playing a significant role and introduces a dependence on T.

Thus, from the temperature dependence of the characteristic time and from the deduced position of the impurities one can conclude that the random telegraph signals in graphene (and, therefore, the flicker noise) are coming from the jumping of electrons between the channel and impurity states, and this jumping is associated with thermally activated hopping above $\sim 3\,\mathrm{K}$. Below 3 K resonant tunneling starts to play a dominant role.

3.7 Flicker noise in samples on Si_3N_4

It was found in Sec. 3.4.3 that short- and long-range scattering potentials have distinctive signatures in the flicker noise. This provides a powerful method of determining the type of scatterers in any graphene sample*. In the same section it was shown that water affects the flicker noise in a very pronounced way by introducing an M-type noise behaviour, which indicates water as a long-range scatterer. After removing the water, the behavior of the noise changes to the V-type indicating a remaining short-range scattering potential, which is either intrinsic to graphene or coming from the substrate. If the remaining noise is intrinsic, then it should be observed in any graphene sample produced in a similar way. Otherwise, it should vary from substrate to substrate. In this section the origin of the remaining noise will be addressed by measurements of the flicker noise in graphene on Si_3N_4.

Samples on Si_3N_4 were prepared using exactly the same fabrication technique as was used for usual samples, Sec. 1.2.1, with the only exception that 90 nm thick Si_3N_4 was used instead of 300 nm SiO_2 as a dielectric. It is known that the roughness of Si_3N_4 is less than that of SiO_2, and it is expected to have a lower number of impurities near the surface† since Si_3N_4 is experimentally observed to have higher breakdown voltage in comparison with SiO_2 (seen in our samples). The lower number of impurities is expected to result in a lower level of noise in these samples.

*As mentioned earlier it is possible to distinguish between short- and long-range potentials since their contributions to the resistance have distinctive dependences on carrier concentration. However, for example, ripples, which give $R \propto 1/n$, are indistinguishable from the long-range scatterers, which give the same $R(n)$ dependence.

†It is also possible that the impurities will be of a different kind.

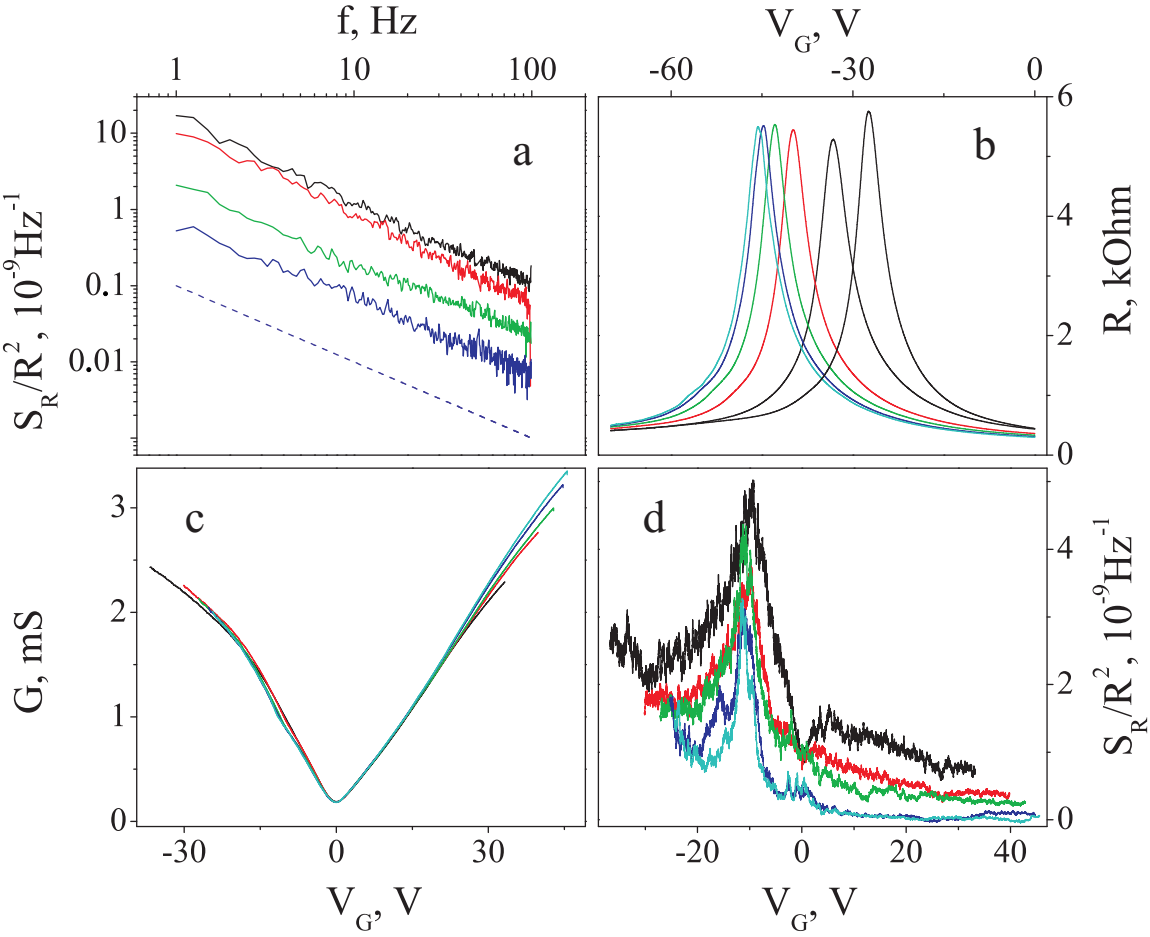

Figure 3.15: (a) S_R/R^2 spectra taken at $T = 30\,\mathrm{K}$ and at different gate voltages for Si_3N_4 sample AG9D1F1. From top to bottom: 0 V, 2 V (red), 9 V (green), 31 V from the Dirac point (blue). (b) $R(V_G)$ dependence for both directions of sweeping at $T = 260\,\mathrm{K}$ (black). Red, green, blue and cyan curves show left peak (direction of sweeping is towards positive V_G) of the hysteretic $R(V_G)$ dependences at temperatures 180 K, 120 K, 80 K and 47 K, respectively. (c) Conductance, G, and (d) normalised noise as functions of V_G at the same temperatures as in (b) with Dirac point shifted to $V_G = 0\,\mathrm{V}$ for each curve individually.

First, the noise spectra taken on Si_3N_4 samples were found to obey $1/f$ scaling*, Fig. 3.15(a), which means that at low frequencies in these samples the phenomenon of flicker noise is also observed (as in SiO_2 samples). Second, a peculiar feature of these samples was seen in resistance measurements. Namely, $R(V_G)$ dependences were found to have a significant hysteresis (more than 10 V even after 140 °C annealing), Fig. 3.15(b), which was seen to increase with decreasing temperature. Third, a nearly linear behaviour was observed in $G(V_G)$ curves indicating the dominance of the long-range scattering potential, Fig. 3.15(c). (On the holes side the linear dependence is

*The results are shown only for low temperatures. Experimentally it was found that the spectra remain $1/f$ at higher T.

preserved only at small concentration.) Also, the sample did not exhibit significant temperature dependence of the conductance in the 30 K−300 K range. Finally, the normalised noise was found to depend on the concentration in a similar way as for M-type samples.

Fig. 3.15(d) shows S_R/R^2 as a function of the gate voltage at different temperatures. The noise is seen to be very asymmetric (with respect to the Dirac point, $V_G = 0$ V) with a pronounced nonmonotonic behavior around the Dirac point. Analysing the electron side of the curves only, one can conclude that the noise behaviour is very close to M-type behaviour observed as a function of T in SiO_2 samples, Fig. 3.8. Starting from M-type dependence at $T = 260$ K the noise transformed into peak-type dependence at $T = 47$ K. According to the logic discussed in Sec. 3.4.3 this behaviour indicates water-like long-range scatterers (also seen as linear conductance), which are most likely to be impurities in Si_3N_4 rather than water, since the sample was annealed before measurements. The similarity between these scatterers in Si_3N_4 and water molecules is even stronger. Namely, similar to water-doped samples on SiO_2, Sec. 2.4, samples on Si_3N_4 also exhibited a large hysteresis in the $R(V_G)$ dependence, Fig. 3.15(b).

Focusing on the hole side of the noise dependences, a large peak around $V_G = -10$ V is seen. In contrast to the rest of the curve this peak is almost temperature independent, which possibly indicates that the origin of it is different from that of the M-type dependence. This peak does not originate from intrinsic properties of graphene as it is not observed in other samples, and, therefore, is caused, again, by the scatterers in Si_3N_4.

3.8 Conclusion

Flicker noise, particularly in graphene, is a rather complicated phenomenon due to the fact that it originates from many different mechanisms. It is closely related to the scattering, since the scattering determines resistance and the temporal resistance fluctuations are noise by definition. This means that it is possible that both noise and resistance originate from the same scattering mechanism. However, it is also possible to observe the opposite. For instance, noisy impurities can be situated deep inside the oxide. Then, whilst dominating the noise, these impurities have negligible effect on resistance due to the large distance between the scatterers and the conductive channel.

All these different realisations result in various observed behaviours of the flicker noise and its temperature dependence in graphene. The work presented in this chapter was dedicated to studying these different noise behaviours at a deeper level and to understanding their origin.

It was shown that at all carrier concentrations and at all temperatures above $\sim 20\,\mathrm{K}$, and even on samples exfoliated on different substrates, the scaling of the normalised noise spectral density with frequency is $1/f$. The flicker noise behaviour was found to be distinctive for different samples. Specifically, it turned out to be possible to divide all the samples into two main groups with M- and V-type behaviour. It was suggested that V-type samples result from a fluctuating short-range potential, while M-type samples were associated with long-range water-like scatterers. Furthermore, the temperature dependence of the flicker noise in M-type samples exhibited some transition from M-type dependence at high T to peak-type dependence at low T. Since M-type noise is related to water-like impurities, it was suggested that this transition can originate from the transition of the structure of such impurities, for example, crystallization of amorphous ice in the case of water.

At temperatures below $\sim 20\,\mathrm{K}$ the flicker noise spectrum splits into separate lorentzians on top of a negligible $1/f$-like background. These lorentzians are the signatures of individual two-state fluctuators (RTS). In the text an example of such a fluctuator was discussed, namely an impurity state, into which electrons from the conductive channel can tunnel. Studying these impurities it was found that they are situated $10 - 30\,\mathrm{nm}$ away from the graphene and that the mechanism of the electron jumps is thermally activated hopping at $T \gtrsim 3\,\mathrm{K}$. Below $\sim 3\,\mathrm{K}$ resonant tunneling starts to play a significant role. The fact that the noise occurs due to distant impurity states confirms the separate origin for noise and resistance (as was observed in the experiment with water-doped samples). Also, a thermally activated mechanism in RTS suggests a similar activation mechanism in the flicker noise, contributing to the picture of the noise temperature dependence (the theory described in Sec. 3.5.2 predicts $S_R \propto T^2$ in this case).

Samples on Si_3N_4 showed M-type behaviour of the flicker noise similar to that in water-doped samples on SiO_2. This fact, along with the observed hysteresis, leads to the conclusion that impurities in Si_3N_4 are water-like long-range scatterers. A peak on the hole side of the S_R/R^2 dependence on the gate voltage also indicates an additional

source of scattering coming from the substrate.

Chapter 4

Quantum transport in graphene structures at high magnetic fields

4.1 Introduction and sample description

Graphene is an attractive material for both applied and fundamental science. However, it is unlikely that it will be employed in electronic applications in its pure form. The main reason for that is the absence of the gap in the graphene band structure. This problem has been intensively debated in the literature and various solutions for opening a gap have been suggested. All these solutions imply the modification of graphene and producing more complex structures out of the initial material. Along with gap engineering, there are attempts to realise the transport of spin and valley index in graphene, which also require development of specific graphene devices. Thus, the investigation of different graphene structures is an important issue for potential applications of graphene.

Here the transport measurements accomplished on a bilayer/trilayer graphene structure will be presented (sample AG9D9F1). Such a device has not been yet investigated either experimentally or theoretically, although the properties of similar monolayer/bilayer structures were calculated in Refs. [70, 71]. Namely, in Ref. [70] the transmission coefficient through a boundary between monolayer and bilayer graphene was predicted to be angle and valley dependent, therefore potentially suggesting a way for controlling the valley currents. In Ref. [71] it was shown that at the interface one should expect the formation of a new set of Landau levels different from that in both

bulk regions.

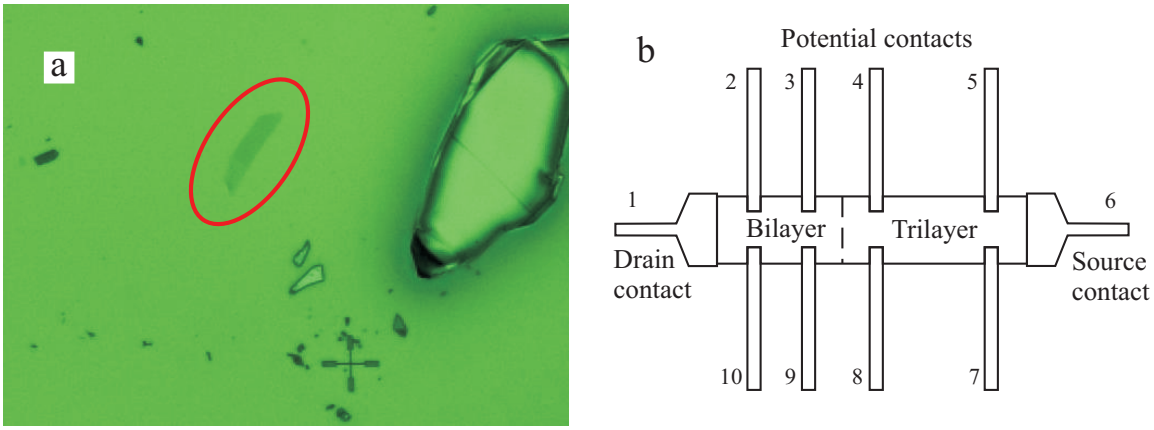

Figure 4.1: (a) Optical image of the sample (ringed). The top part of the sample (about 2/3 of the whole area) is darker then the bottom part, which indicates trilayer and bilayer parts, respectively. The spatial scale is given by a cross which is 10 μm wide. (b) Schematic view of the device with contacts.

The sample is similar to the standard graphene devices described in this thesis, Sec. 1.2.1, with the only difference that the flake consists of two adjacent regions of different thickness (essentially different number of layers), Fig. 4.1. The probability to find such a flake is rather small which explains the small dimensions (within 15 μm) and the fact that the measurements were done on a single sample. In Fig. 4.1(b) contacted device is shown schematically. Besides source and drain contacts there are 8 potential contacts, two pairs on each region. This geometry allows to separate the measurements of the longitudinal and transverse resistances of both bilayer (for example, between contacts 9-10 and 9-3) and trilayer (contacts 7-8, 8-4) parts, and also the longitudinal resistance of the interface (contacts 8-9). In this chapter the 2/3 layer number will be confirmed by different measurements including temperature dependence of the resistance at the Dirac point and transport in the quantum Hall regime. Raman spectra of the sample regions along with the optical contrast were also measured and gave signatures of bilayer and trilayer graphene (not shown here).

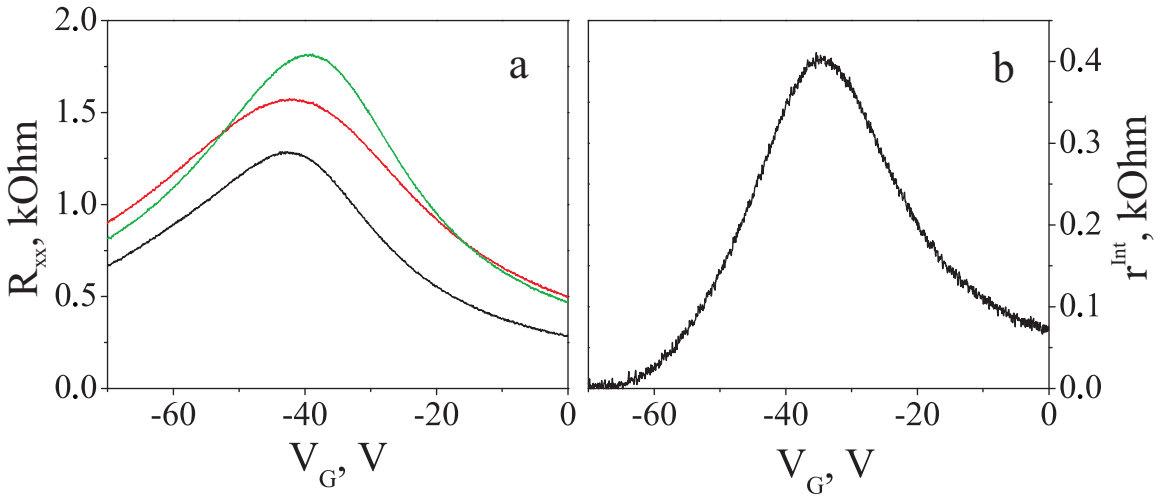

Figure 4.2: (a) Longitudinal resistance of bilayer, R_{xx}^{Bi} (black), trilayer, R_{xx}^{Tri} (red), and interface, R_{xx}^{Int} (green), parts of the graphene flake shown as functions of the gate voltage at $T = 255\,\mathrm{K}$. (b) Pure interface resistance r^{Int} is obtained by subtracting the contributions of bilayer and trilayer from the resistance of the interface part (plotted in panel (a)).

4.2 Temperature dependence

4.2.1 $R(V_G)$ dependence

In Fig. 4.2(a) $R_{xx}(V_G)$ dependences at $T = 255\,\mathrm{K}$ (the highest temperature the sample was measured at) for bilayer, trilayer and interface parts are shown. Each resistance is measured as a voltage drop between a corresponding pair of potential contacts divided by the current in the sample (constant-current regime). The Dirac points of both bilayer and trilayer parts occurred at the same gate voltage, $\sim -43\,\mathrm{V}$*, whereas the position of the maximum of $R_{xx}^{Int}(V_G)$ curve was at $\sim -39\,\mathrm{V}$. The shift in maximum position between R_{xx}^{Int} and bilayer/trilayer parts indicates the existence of the interface resistance r^{Int}, and suggests that it depends on the gate voltage (otherwise the $R_{xx}^{Int}(V_G)$ dependence would have a maximum at $\sim -43\,\mathrm{V}$).

In a given geometry the resistivities of the bulk bilayer and trilayer graphene can be directly obtained from the measured R_{xx}^{Bi} and R_{xx}^{Tri} by scaling by the aspect ratios. R_{xx}^{Int} contains three contributions. Firstly, there is a resistance coming from the interface, which is denoted as r^{Int}. Then, there are bilayer and trilayer parts of the flake enclosed within the potential contacts across the interface, therefore, contributing to

*The sample was annealed in helium atmosphere at 140 °C before measurements. Both Dirac points before annealing were around $V_G = 5\,\mathrm{V}$.

the measured resistance. Since the resistivities of bilayer and trilayer are known from measurements of other parts of the flake, one can extract r^{Int} by subtracting scaled R_{xx}^{Bi} and R_{xx}^{Tri} from R_{xx}^{Int} (the formula for r^{Int} is written explicitly below in Sec. 4.2.3). The resulting curve for the pure interface resistance is shown in Fig. 4.2(b). As one can see, the obtained resistance is indeed gate voltage dependent, and drops almost to zero at $V_G = -70\,\mathrm{V}$. Also, after subtraction the discrepancy between the Dirac point positions is even more pronounced (maximum is at $V_G =\sim -35\,\mathrm{V}$).

4.2.2 Theoretical expectations

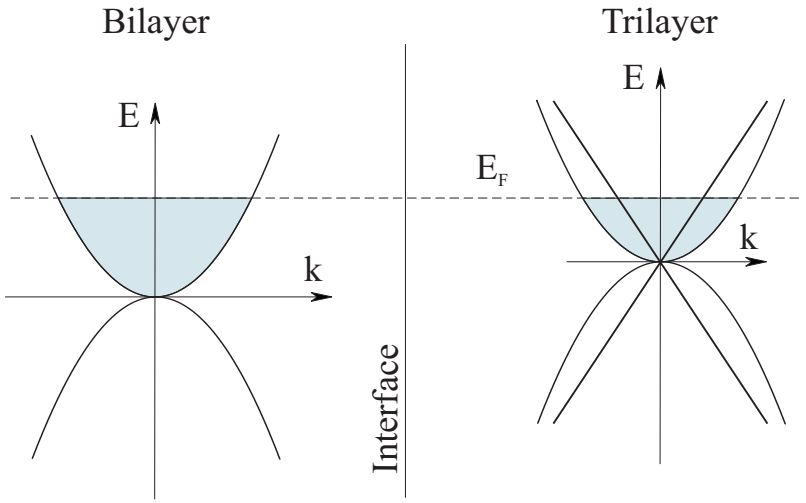

Figure 4.3: Band structures of the bilayer and ABA stacked (as an example) trilayer graphene are shown schematically. Coloured areas represent equal numbers of carriers in both regions of the sample under applied gate voltage.

Graphene sample studied here has a particular feature associated with the gate control of the carrier density in the sample. The electro-chemical potential in equilibrium has to be constant in the whole system and does not change through the boundary between bilayer and trilayer parts. The concentration of the carriers is determined by the gate and also has to be constant throughout the whole flake (if the quantum capacitance is assumed to be negligible). However, it is known that bilayer and trilayer graphene have different densities of states as functions of the Fermi energy (as their band structures are different). Therefore, at any given gate voltage, except the one where the Fermi level crosses the Dirac point in both regions (in this case $V_G \sim -42.5\,\mathrm{V}^*$), the Dirac points in bilayer and trilayer are separated in energy. Thus,

*Dirac points in the bilayer and trilayer turned out to be at the same gate voltage after annealing,

carriers at the Fermi level in different parts have different kinetic energies*, Fig. 4.3, and an electron that propagates from trilayer to bilayer through the interface has to experience an effective potential difference equal to the difference of the kinetic energies (similar to p-n junction). Furthermore, due to the fact that the carrier crossing the interface has to change the wave vector in order to stay at the Fermi level, the transmission coefficient through the interface should be less than unity. The interface region at low temperatures, when the energy of thermal fluctuations kT is smaller then the potential difference, is expected to be more resistive, thus, making the transport through the transition sensitive to temperature.

The model described above suggests that the resistance of the interface as a function of V_G should be symmetric with respect to the bulk Dirac point† and should have a minimum at the Dirac point, since at this position the kinetic-energy difference is minimal (zero). This is not confirmed by the experiment, Fig. 4.2, as one sees the opposite behaviour. Namely the interface resistance decreases with increasing gate voltage from the Dirac point and has a maximum close to, although not exactly at the Dirac point. This discrepancy suggests that either the interface resistance does not exist or its properties are not as simple as described above.

More complex behaviour of the interface can originate from different mechanisms. First, the band structure of ABA trilayer‡ graphene shown in Fig. 4.3 is an approximation. In reality the linear band can be shifted with respect to the parabolic band and in both bands there can be a gap [72]. This would introduce nonmonotonicity into the kinetic energy difference. Second, due to chiral nature of the carriers the propagation through the interface can have some specifics associated with Klein tunneling [36]. In fact, in a similar system with a monolayer/bilayer interface, the transmission coefficient was shown to be angle-dependent [70]. Third, the boundary between bilayer and trilayer parts is not a straight line. Instead, it has a random shape determined by the process of the flake deposition. As a result, the interface line consists of both armchair and zigzag edges tilted from the direction perpendicular to the current. Therefore, the

which happened in some sense by pure chance, since one would expect different sensitivity of the graphene to the dopants on the surface depending on the number of layers.

*Kinetic energy is defined as the Fermi energy, since it defines the k vector of the current carriers.

†From here on either of two Dirac points in bilayer or trilayer will be referred to as the Dirac point, since they coincide in the sample studied here.

‡ABA trilayer graphene is chosen only as an example. The same arguments are valid for any trilayer, as long as the density of states in trilayer differs from that in bilayer.

measured value of the interface resistance is averaged in both angle and type of the edge. Finally, the shape of the flake is not rectangular which also influences both the direction of current and the geometrical factors of the bilayer and trilayer contributions to the interface resistance.

No attempts to take into account all these effects have been made except for the corrections to the geometrical factors, as will be shown below in Sec. 4.2.3.

4.2.3 Temperature dependences

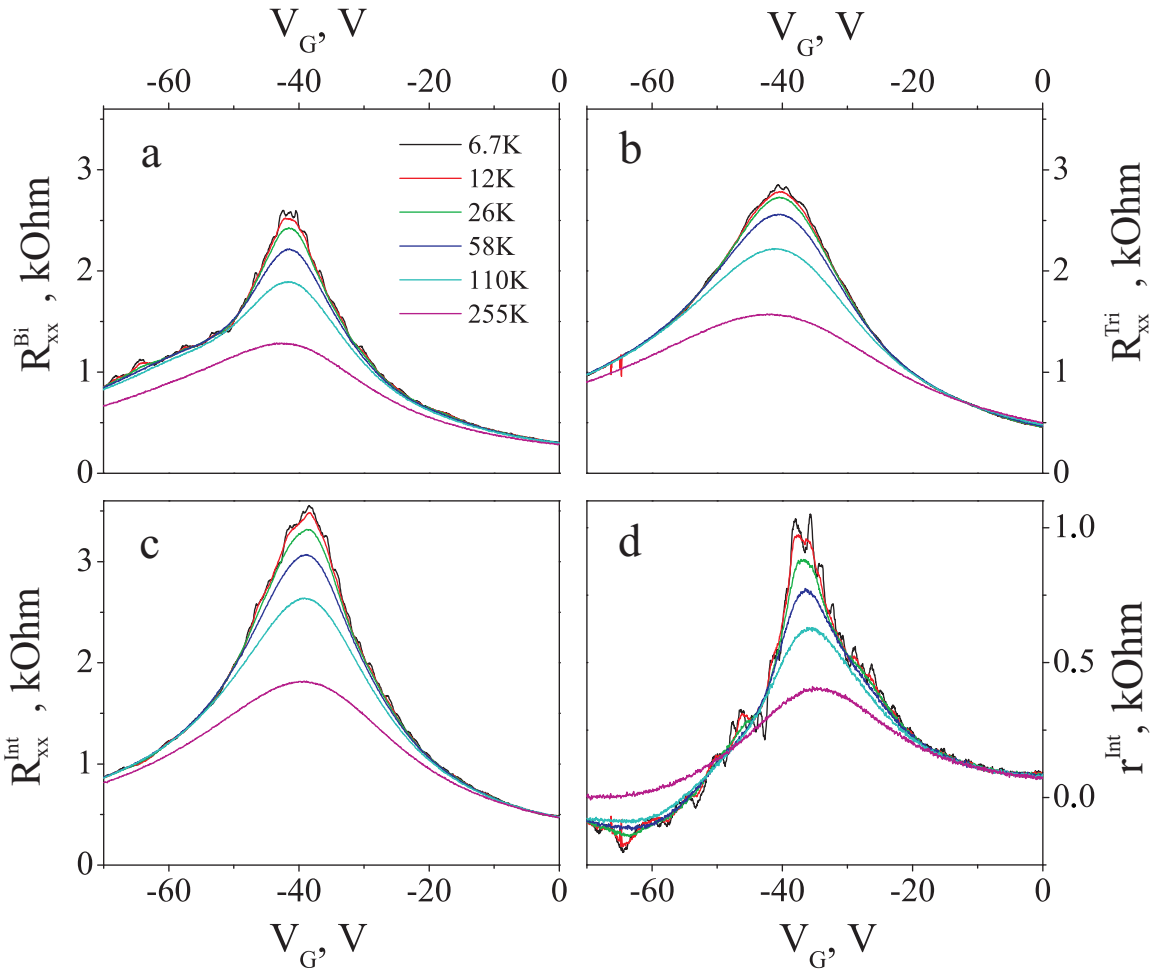

Figure 4.4: $R_{xx}(V_G)$ at different temperatures for (a) bilayer, (b) trilayer and (c) interface parts of the sample resistance. The set of temperatures is given in the legend. (d) Pure interface resistance, r^{Int}, after subtraction of bilayer and trilayer contributions. Subtraction coefficients are determined from actual geometry.

Panels (a), (b) and (c) in Fig. 4.4 show dependences on V_G of longitudinal resistances of bilayer, trilayer and interface parts at different temperatures*. R_{xx}^{Bi} and R_{xx}^{Tri} at their

*The measurements were carried out in a helium dewar. Therefore the maximum temperature

maxima are seen to vary significantly in the given temperature range, which is a clear signature of the multilayer supported graphene, Sec. 3.5.2 and [72, 73]. Monolayer graphene on a substrate usually exhibits less than 20 % change in the resistance at the Dirac point when the temperature varies within $4\,\mathrm{K} - 300\,\mathrm{K}$. The interface contribution to the resistance is seen to depend on temperature in a similar way.

There is also a peculiarity in all three resistance curves. While below 110 K the resistance on the hole side of the dependences is almost independent of T, between 110 K and 255 K it experiences a significant decrease seen as a shift of the 255 K curve downwards with respect to the 110 K curve. This jump can indicate either a temperature activated scattering mechanism in graphene or a sudden change in the contact resistance at one of the current contacts. Transport in graphene away from the Dirac point is unlikely to be temperature-activated, whereas an unstable contact is a common result of the fabrication procedure. (Circulation of the temperature and checking the reproducibility of the results would help to distinguish between the two, however, it has not been done.)

Following the same logic as in Sec. 4.2.1 the pure interface resistance was calculated with the formulae

$$r^{Int} = R_{xx}^{Int} - \frac{N'_{Bi}}{N_{Bi}} R_{xx}^{Bi} - \frac{N'_{Tri}}{N_{Tri}} R_{xx}^{Tri}, \tag{4.1}$$

where N and N' are the number of squares (ratio of the length to the width) in the corresponding parts of the flake. N denotes the homogeneous regions of the flake (between contacts $7-8$ and $9-10$), and N' denotes the homogeneous regions adjacent to the interface (between contacts $8-9$). Fig. 4.4(d) shows the obtained curves for a given set of temperatures. Except for the highest temperature $r^{Int}(V_G)$ dependence (which has been already shown in Fig. 4.2), the interface resistance turned out to become negative at $V_G \lesssim -50\,\mathrm{V}$, therefore indicating incorrectness of the factors in formula 4.1.

The main reason for this discrepancy is suggested to be an error in determining the geometrical factors, which are denoted by $\alpha = N'_{Bi}/N_{Bi}$ and $\beta = N'_{Tri}/N_{Tri}$. The factors are taken from the optical image of the flake with the contacts, Fig. 4.1, by averaging both longitudinal and transversal dimensions. The deviation of the real shape of the flake from rectangular along with the finite size of the potential contacts

255 K was determined by the temperature of the helium gas near the top of the dewar. The lowest achievable temperature is the temperature of liquid helium, 4.2 K.

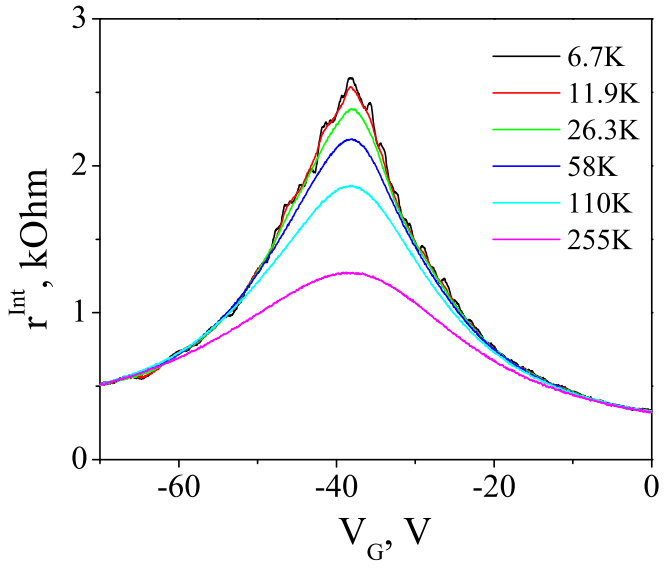

Figure 4.5: Interface resistance as a function of V_G at different temperatures. Geometrical factors were used as fitting parameters to obtain positive resistance in the while range of V_G.

result in a significant error in estimating values of both N and N'.

One should note that the uncertainty in geometrical factors α and β causes a rather large error in determining r^{Int}. Using the maximal values for α and β it is possible to obtain r^{Int} negative in the whole range of gate voltages. Also, the position of the maximum in $r^{Int}(V_G)$ dependences is changed in this case to $\sim -43\,\mathrm{V}$ (not shown here), thus, suggesting that we cannot resolve the difference between the positions of the maximum in the interface resistance and bulk bilayer and trilayer parts. However, the maximum in measured $R_{xx}^{Int}(V_G)$ is indeed shifted by $\sim 1.5\,\mathrm{V}$ from that in $R_{xx}^{Tri}(V_G)$ and $R_{xx}^{Bi}(V_G)$. Therefore, it is still concluded that this difference in maximum position is an experimental fact rather than a result of inaccurate data analysis.

Here the procedure for optimising the geometrical factors is proposed. r_{Int} has minima at the ends of the gate voltage range. Therefore, the resistance is likely to be positive in the whole range, if it is positive at the ends of this range. From Fig. 4.4 panels (a) and (b) it is known that R_{xx}^{Bi} and R_{xx}^{Tri} have jumps in their temperature dependences at $V_G = -70\,\mathrm{V}$. These jumps are 160 Ohm and 70 Ohm, respectively. It is also known that the same jump in R_{xx}^{Int} is 48 Ohm. Therefore, assuming that the

interface resistance r^{Int} at $V_G = -70\,\mathrm{V}$ does not change with temperature, one can rewrite Eqn. 4.1 as an equation for α and β

$$0 = 48 - 160\alpha - 70\beta. \tag{4.2}$$

The equivalent equation for the positive end of the gate voltage range is automatically satisfied, since all three terms in formulae 4.1, αR_{xx}^{Bi}, βR_{xx}^{Tri} and R_{xx}^{Int} at $V_G = 0\,\mathrm{V}$ do not depend on T.

Eq. 4.2 gives the linear relation between α and β. To determine them explicitly another relation is needed*. For instance, departing from the symmetry arguments one can assume the equality of the interface resistances at $V_G = -70\,\mathrm{V}$ and $V_G = -10\,\mathrm{V}$ (as the maximum of the $r_{Int}(V_G)$ dependence is at $\sim 40\,\mathrm{V}$). However, here another relation will be employed, since it will require less calculation and also give symmetric dependences with respect to the maximum. Namely, it is assumed that the ratio α/β is the same as that obtained from the optical image, i.e.

$$\alpha/\beta = 0.6/0.45 = 1.33. \tag{4.3}$$

The solution of the system of Eqs. 4.2 and 4.3 gives $\alpha \simeq 0.23$ and $\beta \simeq 0.17$. Finally, resulting curves for the interface resistance obtained with optimised geometrical factors are shown in Fig. 4.5.

It is seen that the $r_{Int}(V_G)$ dependences are more symmetric now and the value of the resistance does not go below zero. Moreover, the position of the maximum of the interface resistance is now almost independent of temperature, although this can be partially explained by symmetrisation. The obtained temperature dependence of the interface resistance does not exhibit any activation behaviour, as one should expect in the case of the transport between two regions with different Fermi energies.

The geometrical factors used for plotting r^{Int} in Fig. 4.5 turned out to be approximately 3 times smaller than those obtained from the optical image. Two reasons for the large error in determining α and β were mentioned above. Firstly, the non-rectangular shape of the flake gives an error in the width of the flake region. Secondly, the finite size of the contacts introduces an error in length. In fact, the widths of the flake regions

*The additional relations can also be taken from the fact that both α and β have to be positive. Then, Eq. 4.2 gives $\alpha \leq 48/160 = 0.3$ and $\beta \leq 48/70 \simeq 0.69$.

(bilayer, trilayer and the regions adjacent to the interface) are comparable to the width of the potential contacts. Therefore, for example, N_{Bi} has an error of $\sim 100\%$.

4.3 Quantum Hall regime

4.3.1 Change of the measurement scheme

In this section the measurements of the same sample (AG9D9F1) in the quantum Hall regime will be presented. For this regime low temperatures and high magnetic fields were achieved in the cryostat. This cryostat did not have an annealing setup in situ, and so the sample was transferred through the air from a dewar where it was annealed to the cryostat. As a result, the Dirac points of the bulk bilayer and trilayer graphene parts were shifted to the right from $\sim -42\,\mathrm{V}$ to $\sim -34\,\mathrm{V}$ most likely due to the doping by atmospheric water. Also, two contacts were damaged during this procedure. Namely, the drain contact (contact 1 in Fig. 4.1(b)) and potential contact on the bilayer part (contact 3) were not electrically connected to the flake after the transfer. Consequently, the drain contact was switched to the contact 2, which is a potential contact on the bilayer side of the flake. Thus, the measurement of the transverse resistance of bilayer was not possible any more. Contacts $7-8$ and $8-4$ were used to measure longitudinal and transversal resistances of trilayer, respectively, and contacts $8-9$ and $9-10$ were used for longitudinal interface and bilayer resistances.

4.3.2 Trilayer graphene in the Quantum Hall regime

Shubnikov-de-Haas oscillations

In Fig. 4.6(a) longitudinal resistivity ρ_{xx}^{Tri} and transverse conductivity σ_{xy}^{Tri} of trilayer graphene are shown as functions of magnetic field. As seen ρ_{xx}^{Tri} experiences Shubnikov-de-Haas oscillations starting from $\sim 4\,\mathrm{Tesla}$*. These oscillations are a signature of the quantisation of the 2D electron gas† in the sample and appearance of the Landau levels in the energy spectrum. The separation between the Landau levels is known to increase with increasing magnetic field, therefore, at some B this separation becomes

*The origin of the hump around 2 Tesla is unknown.

†The fact that the carriers are electrons is confirmed by the sign of the Hall coefficient, Fig. 4.6(b). Also, the measurements were carried on the electron side of $R_{xx}^{Tri}(V_G)$ dependence, namely at 0 V, when the Dirac point was negative.

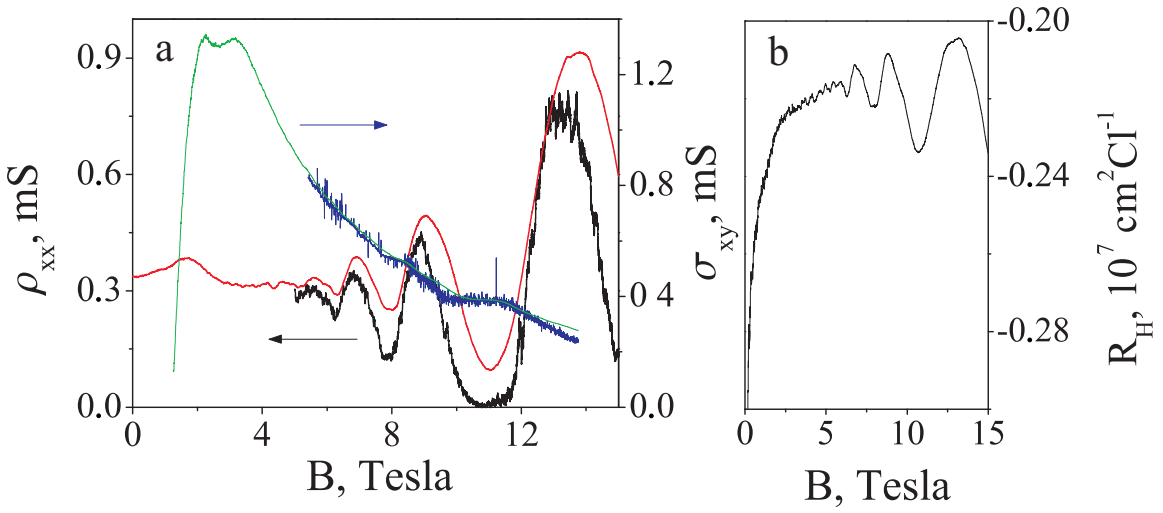

Figure 4.6: (a) Longitudinal resistivity, ρ_{xx}^{Tri} and transverse conductivity, σ_{xy}^{Tri}, of the trilayer graphene as functions of magnetic field at 4.1 K (red and green curves, respectively) and at 170 mK (black and blue curves). (b) $R_H \equiv R_{xy}^{Tri}/B$ (Hall coefficient) dependence on magnetic field.

larger than the dispersion of the levels due to the disorder and temperature and the quantisation becomes full. It is seen as a vanishing of the longitudinal component of the resistivity at 11 Tesla and 170 mK. At the same time the transverse conductivity experiences a plateau at $\sigma_{xy} = 0.388\,\text{mS} = 10e^2/h$ (as will be discussed it is one of the plateaus forming in trilayer graphene).

From the value of the Hall coefficient one can estimate the concentration of the carriers. In Fig. 4.6(b) it is seen that at small magnetic field (although big enough in order to avoid large error in determining both values of field and resistance) R_H is approximately equal to $-0.22 \cdot 10^7\,\text{cm}^2\text{C}^{-1}$. Therefore, concentration can be calculated as $n' = -1/R_H/e = 2.8 \cdot 10^{12}\,\text{cm}^{-2}$. This value can be compared with that extracted from the known capacitance between the flake and the gate and the voltage applied between them. The Dirac point was at $V_G = -34\,\text{V}$, which means that the concentration of carriers induced by the gate at $V_G = 0\,\text{V}$ is $n'' = 7.2 \cdot 10^{14} \cdot 34 = 2.4 \cdot 10^{12}\,\text{cm}^{-2}$ (Sec. 1.2.2). The difference in concentration values, which were obtained by two different methods, is $0.4 \cdot 10^{12}\,\text{cm}^{-2}$. Usually the discrepancy between n' and n'' is associated with the fact that Hall coefficient gives the number of conducting mobile carriers, while capacitor charge includes also localised electrons, which are trapped, for example, in the midgap states. However, this hypothesis suggests $n'' > n'$, which is opposite to the deduced values.

Integer QHE under a constant magnetic field

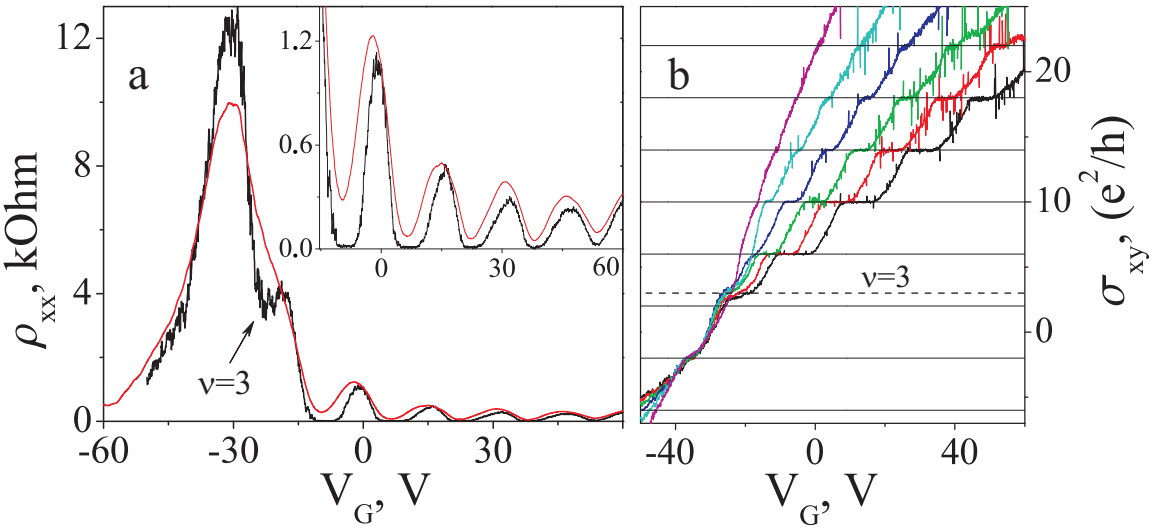

Figure 4.7: (a) Longitudinal resistance of trilayer graphene as a function of V_G at 13 Tesla, at $T = 4.1$ K (red) and 170 mK. Inset shows zoom in of the main plot. (b) Transversal conductivity dependence on V_G at 170 mK at different magnetic fields. From the right curve to the left: 15, 13, 11, 9, 7 and 5 Tesla. Horizontal lines show expected values for the plateaus in monolayer graphene. Dashed line shows the level with $\nu = 3$.

Alternatively, to observe the signatures of the formed Landau levels one can sweep the gate voltage keeping the magnetic field constant. The dependence of ρ_{xx}^{Tri} on V_G at 15 Tesla is shown in Fig. 4.7(a). The Fermi level in graphene, E_F, depends on the gate voltage, therefore by sweeping V_G one changes its position with respect to the Landau levels. When E_F is in between the Landau levels there are no conducting states in the bulk around it, and the current is carried only by the edge states, which have a strictly determined value of conductivity e^2/h per state. In this regime the transverse conductivity shows a plateau and the longitudinal resistivity and conductivity become zero. Vice versa, if the Fermi level is close to the Landau level, the states on the level contributes to the conductance and ρ_{xx}^{Tri} exhibits a maximum. Longitudinal resistivity is plotted for two temperatures, demonstrating the activation mechanism of the electrical conductance between the formed Landau levels. It is seen that ρ_{xx} depends on temperature not only around minima (indicating activation) but also around maxima. This can result from the shift of the whole dependence up/down with temperature. However, $\rho_{xx}(T)$ dependence around minima is stronger than that around maxima.

In Fig. 4.7(b) one can see $\sigma_{xy}^{Tri}(V_G)$ dependences with well developed at 15 Tesla

plateaus, which almost completely vanish at 5 Tesla. The plateaus are observed at filling factors $\nu \equiv hn/eB$ equal 22, 18, 14, 10 and 6. Also there are pronounced indications of further plateaus at $\nu \sim 3$ (at $T = 170\,\mathrm{mK}$ the minimum in ρ_{xx}^{Tri} is also seen, Fig. 4.7(a)) and $\nu \sim -2$. Except for the latter ones all the plateaus are in agreement with theoretical predictions for integer quantum Hall effect in trilayer graphene, [74, 75], as was also confirmed in Refs. [72, 76, 77]. It is worth mentioning that monolayer graphene has the same set of plateaus as trilayer with the difference at small ν, [3], i.e. for monolayer graphene there are two additional plateaus at $\nu = \pm 2$. Therefore, two measured plateaus at $\nu \sim 3$ and $\nu \sim -2$ can be suggested as plateaus that are absent in a trilayer but are present in the monolayer graphene quantum Hall effect. This would suggest that the measured flake is a monolayer. However, as will be discussed later, plateaus at $\nu \sim 3$ and $\nu \sim -2$ can be associated with the deviations in the ideal band structure of the trilayer graphene shown in Fig. 4.3. Also, one should expect the lowest plateaus to be the most pronounced since the distance between the Landau levels is the largest at this position of the Fermi level.

Fan diagram and integer filling factor lines

The most complete way to show the quantum Hall effect is to plot a fan diagram of the oscillations of the longitudinal resistivity as a function of the magnetic field and carrier concentration. In this diagram the minima in ρ_{xx} becomes valleys and maxima becomes hills, so that one can trace the evolution of the Landau level position with both B and n. Also, one can try to fit this plot with the lines of the constant filling factors as done in Fig. 4.8, where the fan diagram of the ρ_{xx}^{Tri} oscillations is shown.

In order to increase the clarity of the plot, the constant component was removed from the signal by differentiation of the resistivity with respect to the gate voltage. Also, the colour scale was assigned to the levels of the signal in a logarithmic scale in order to increase the contrast. Therefore, oscillating ρ_{xx}^{Tri} gives derivative oscillating around zero. In order to colourplot this derivative in logarithmic scale its value was shifted up by 1 (since by the absolute value it did not exceed 1). Thus, the line of the minimum in resistivity is seen in the diagram as a level with value 1 (red contour).

Between the Landau levels the filling factor is integer and at the same time ρ_{xx} experiences a minimum. It means that at these points the resistivity derivative changes sign from negative to positive with increasing n. In Fig. 4.8 the lines of integer filling

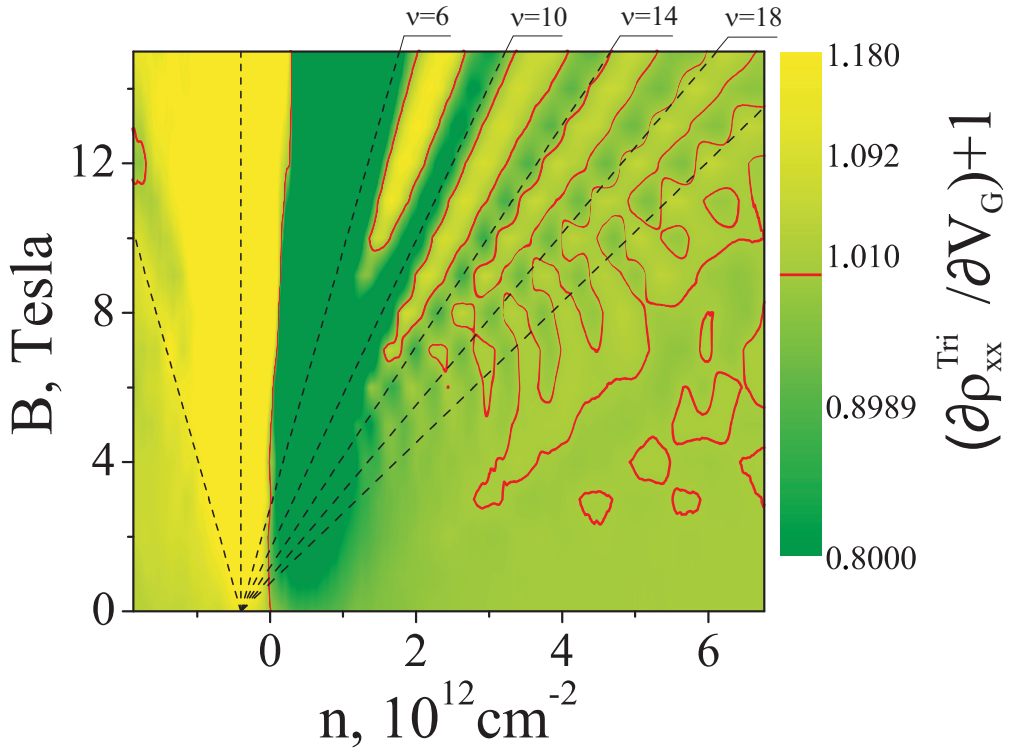

Figure 4.8: $\partial\rho_{xx}^{Tri}/\partial V_G + 1$ is shown in a fan diagram as a function of magnetic field and carrier concentration (the signal is shifted in its magnitude up by 1 in order to avoid negative values). Colour scale is logarithmic. Dashed lines show the lines of a constant filling factors $\nu = [-6, 6, 10, 14, 18, 22]$. Signals higher than 1.18 and lower than 0.8 are coloured as levels 1.18 and 0.8, respectively. Red contour shows the level with the value 1 (zero derivative).

factors that are expected to be seen in trilayer graphene are shown. The lines are in a good agreement with experimental data under the assumption that the real concentration of the carriers is shifted. This gives the discrepancy with the Dirac point position of $0.4 \cdot 10^{12}/7.2 \cdot 10^{10} \sim 5.6\,\mathrm{V}$, which is consistent with the shift obtained from the Hall coefficient as shown above.

Discussion and explanation

The structure of the Landau levels in trilayer is fully determined by the structure of the bands. In the simplest approximation, when only the nearest-neighbor intra- and interlayer hopping parameters γ_0 and γ_1 are taken into account, the bands of the trilayer graphene with ABA and ABC stacking orders* have a structure shown in Fig. 4.9.

To analyse the bands structure it is easier to start with ABA trilayer, since its band structure is a simple superimposition of the monolayer and bilayer subbands (in

*The definitions of the ABA and ABC stacking orders can be found in Ref. [75].

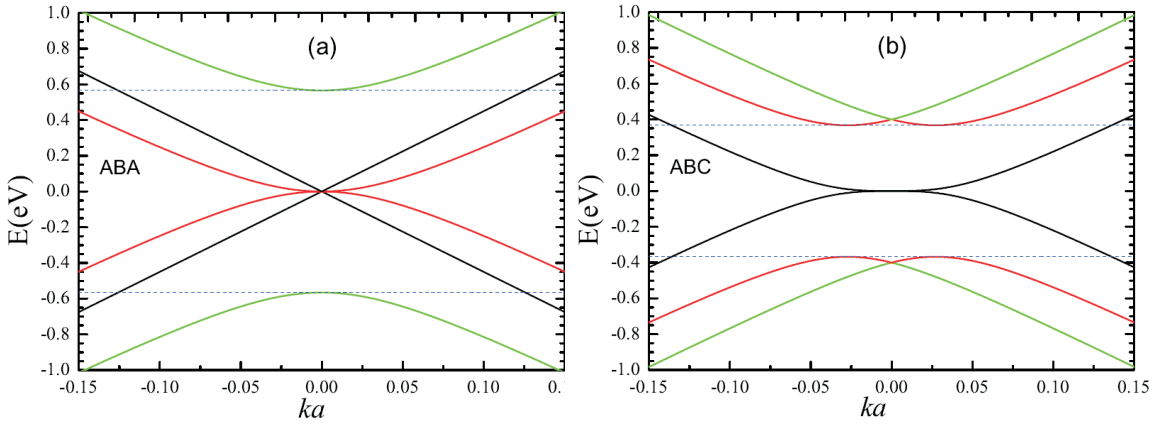

Figure 4.9: Low energy band structures of ABA- (left) and ABC- (right) stacked trilayer graphene analytically calculated with only two nearest-neighbor parameters $\gamma_0 = 3\,\text{eV}$ and $\gamma_1 = 0.4\,\text{eV}$. Adapted from Ref. [75].

the simple approximation described above). Thus, within this picture the monolayer and bilayer sets of the Landau levels can be considered independently from each other, except when they intersect at particular values of the magnetic field. This is possible, since for a monolayer the subband positions of the levels are proportional to $\sqrt{B}$, while for a bilayer subband it is $\propto B$, [3]. One of the crossing points is a Dirac point, where the 4-fold degenerate level from the monolayer subband is joined by the 8-fold degenerate level from the bilayer subbands. This results in a 12-fold degenerate zero Landau level in trilayer graphene, which, in turn, leads to a $12e^2/h$ jump in σ_{xy}^{Tri} when the Fermi level crosses the Dirac point. As shown in Ref. [74] the 12-fold degenerate zero levels and 4-fold degenerate levels of the higher orders are the common features for both ABA and ABC stacked trilayers.

In contrast, the ABC stacked graphene band structure cannot be presented as a superposition of monolayer and bilayer subbands. Instead, the Landau levels are formed as a single set of the levels with no intersection, [74, 75]. Therefore, the intersection of the Landau levels can be used as a method for determining the stacking order, as was done experimentally in Ref. [72], where the quantum Hall effect was studied in an ABA trilayer graphene. The crossing of the levels results in the increased density of states (DOS) at the crossing energy as seen in Fig. 4.10(b). Increased density of states, in turn, leads to the increase of the longitudinal resistivity (since in the quantum Hall regime $\rho_{xx} \propto \sigma_{xx} \propto DOS$). Therefore, the oscillations in $\rho_{xx}^{Tri}(V_G)$ should mimic the oscillations in the density of states. Thus, the abnormality in ρ_{xx}^{Tri} oscillations seen in

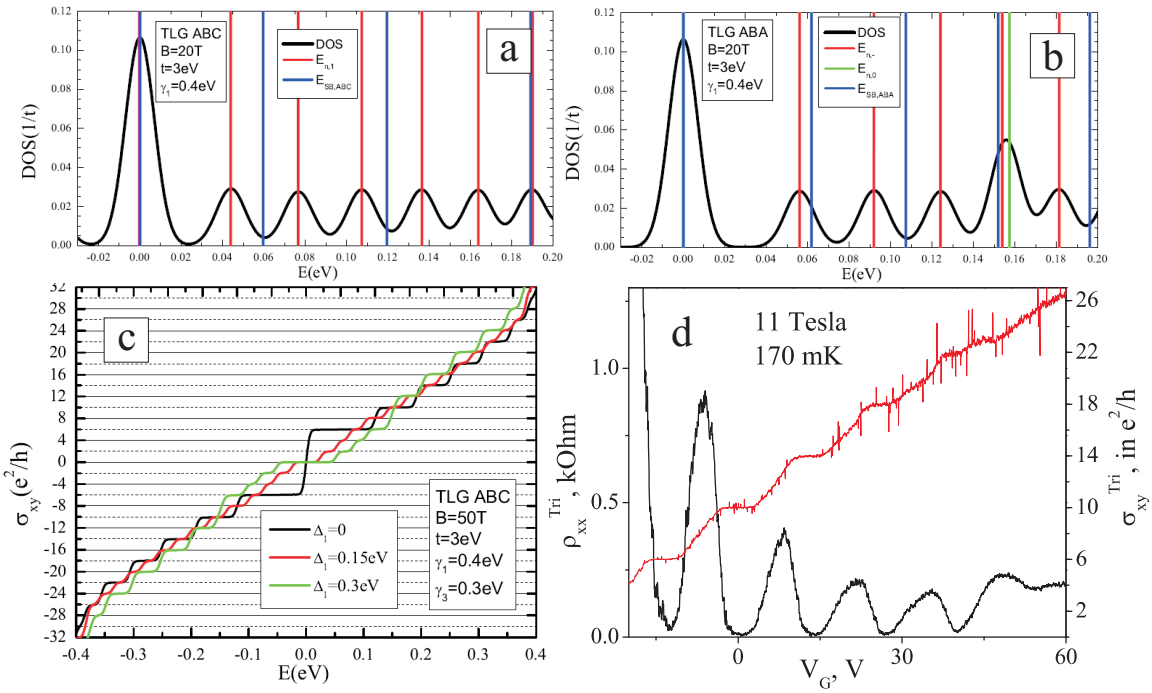

Figure 4.10: Calculated DOS of ABC (a) and ABA (b) trilayer graphene. (c) Transversal conductivity calculated for ABC stacked trilayer. (d) ρ_{xx}^{Tri} (black) and σ_{xy}^{Tri} (red) measured at $T = 170\,\mathrm{mK}$ and $B = 11\,\mathrm{Tesla}$. Panels (a),(b) and (c) are adapted from Ref. [75].

Fig. 4.10(d) ($T = 170\,\mathrm{mK}$) can be associated with intersecting Landau levels suggesting that the measured device is an ABA stacked trilayer. Intersections cannot be seen in the fan diagram in Fig. 4.8 due to low resolution of the data at 4.1 K.

In Ref. [72] it was also shown that the best fit of the results can be produced only with taking into consideration the hopping parameters $\gamma_2 - \gamma_5$ along with the potential difference between the layers δ. In turn, non-zero $\gamma_2 - \gamma_5$ and δ lead to a relative shift of the monolayer and bilayer subbands and to the opening of the gaps in their structure* (see also Ref. [78]) causing the asymmetric behaviour of the transport properties with respect to the Dirac point.

The calculations reported in Ref. [75] suggest that the plateaus in transversal conductivity at filling factors ± 6, ± 10, ± 14,.. is the signature of the quantum Hall effect in trilayer graphene for both stacking orders. However, a plateau at $\nu = \pm 18$ is present only in case of ABC stacked trilayer, Fig. 4.10(c) (at magnetic field below 50 Tesla and absence of transverse electric field). Since in our measurements this plateau is seen, Figs. 4.7 and Fig. 4.10(d), one should suggest that the device studied here is an ABC

*Although the gaps in bilayer and monolayer bands appear, the band gap in the whole structure does not open due to the overlap between the bands.

stacked trilayer, although the intersection of the Landau levels suggests the opposite.

In Ref. [77] by fitting the amplitude of the Shubnikov-de-Haas oscillations with changing temperature, the divergence of the cyclotron mass m_c near the Dirac point was shown. The divergence of m_c is a direct consequence of the cubic band, which is a characteristic of ABC graphene only. However, this method cannot be applied to the measured data shown here since there are only two points in the temperature dependence.

Another possible way to distinguish between ABA and ABC trilayers is to study the splitting of the zero Landau level, since one should expect the splitting to depend on the band structure. However, no progress towards this direction has been done, and, therefore no conclusion based on the character of the splitting can be made. The observed additional plateaus at filling factors 3 and 2 can be simply ascribed to the spin-splitting of zero Landau level (by analogy with monolayer graphene [79]), as was suggested in Ref. [77], where in a similar way the plateaus were observed at $\nu = \pm 3$ in ABC-stacked graphene.

Therefore, since two signatures observed in ρ_{xx}^{Tri} and σ_{xy}^{Tri} suggested the opposite orders of stacking in our sample and other method described above are not applicable, it is impossible to determine either it is an ABA or ABC trilayer. Nevertheless, the observed behaviour of the longitudinal and transversal conductivities demonstrates that the measured device is trilayer graphene.

4.3.3 Bilayer graphene in the quantum Hall regime

In the previous subsection the quantum Hall effect was investigated in trilayer graphene, which is a part of the two-component graphene structure discussed in this chapter. Here, similar studies will be described on the bilayer part of the sample. As mentioned earlier two contacts on this part were not electrically connected to the sample after the transfer procedure. Therefore, the measurement of the transverse component of the resistivity in the bilayer part became impossible in the given geometry leaving only longitudinal resistivity experimentally available.

The quantum Hall effect in bilayer graphene was reported and explained first in Ref. [15], where in contrast to monolayer graphene the carriers were shown to have a finite effective mass, yet still be chiral. The sequence of the plateaus in the quantum

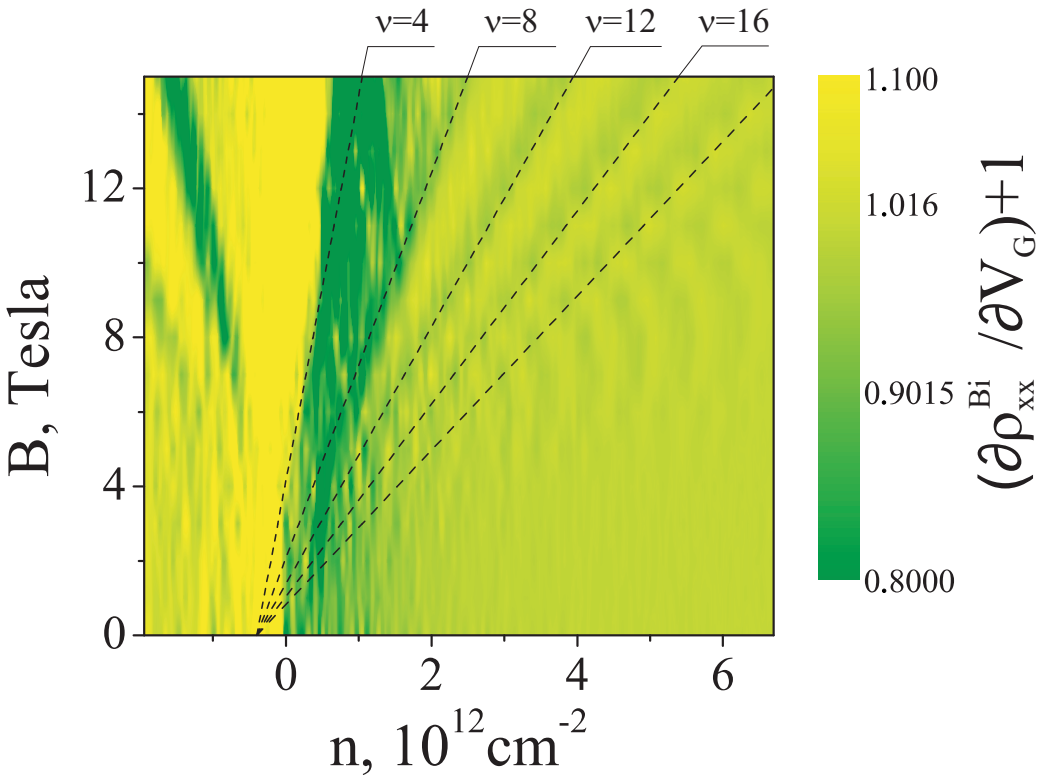

Figure 4.11: $\partial\rho_{xx}^{Bi}/\partial V_G + 1$ is shown in a fan diagram as a function of magnetic field and carrier concentration (the signal is shifted up by 1 in order to avoid negative values). Colour scale is logarithmic. Dashed lines show the lines of constant filling factor $\nu = hn/eB = [-4, 8, 12, 14, 18]$. Signal higher than 1.1 and lower than 0.8 are coloured as levels 1.1 and 0.8, respectively.

Hall regime was found to be $\pm 4e^2/hN$ for $N \geq 1$ with no plateau at $N = 0$. Expected positions of the Landau levels are in a good agreement with the minima on the oscillations of ρ_{xx}^{Bi} as seen in Fig. 4.11. In the figure (as was done for trilayer, Fig. 4.8) it is plotted not the longitudinal resistance itself but its derivative shifted up by 1. Although the lines on the colour plot are rather indistinct, one still can see the signatures of them and can fit them with a set of constant integer filling-factor lines, which are shown as dashed lines. Again, similar to trilayer part, the fitting gives a shifted value for the Dirac point. Dirac point measured as a maximum in $R(V_G)$ dependence is $\sim -34\,\mathrm{V}$, and the value from the fit differs from this value by $\sim 5.6\,\mathrm{V}$.

Thus, the observed behaviour of the longitudinal resistivity of the sample allows us to confirm that the measured part of the sample is indeed bilayer graphene. This, in turn, confirms that the other part of the sample is trilayer graphene since the trilayer part has larger contrast than the bilayer part, Fig. 4.1. The discrepancy between the measured and estimated positions of the Dirac point is not explained, although it is

worth mentioning that in the trilayer part a similar discrepancy of the same value was found from both fitting of the fan diagram and from the Hall coefficient.

4.3.4 Interface resistance in strong magnetic field

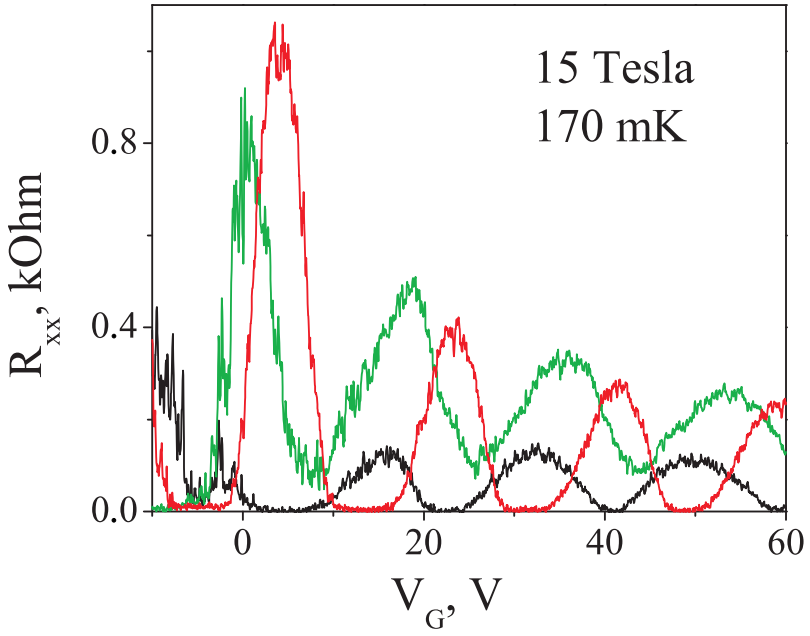

Figure 4.12: Longitudinal resistances of bilayer (black), R_{xx}^{Bi}, trilayer (red), R_{xx}^{Tri}, and interface (green), R_{xx}^{Int}, as functions of the gate voltage at 15 Tesla and 170 mK.

Now let us finally describe the measurement of the interface resistance. One should note that while in Sec. 4.2 the sample was measured in the regime of scalar resistivities, here the presence of magnetic field obliges us to use a two-dimensional matrix of resistivity. This means that the bilayer and trilayer contributions to the interface resistance cannot be simply subtracted. Therefore from here and below the full interface resistance will be considered.

In Fig. 4.12 the oscillations in longitudinal resistance of trilayer and bilayer parts are shown at the highest measured magnetic field (largest separation between the Landau levels). Comparing the oscillations in R_{xx} of trilayer and bilayer parts one can see that they are shifted by a half of a period from each other. This shift is a direct consequence of their Landau level structure. While the bilayer has minima at filling factors $4, 8, 12$, etc., trilayer minima are at $6, 10, 14$, etc. This means that when the Fermi level (which does not change across the sample) crosses the Landau level in the bilayer, it is in between the Landau levels in the trilayer. Therefore, when conductance in bilayer is

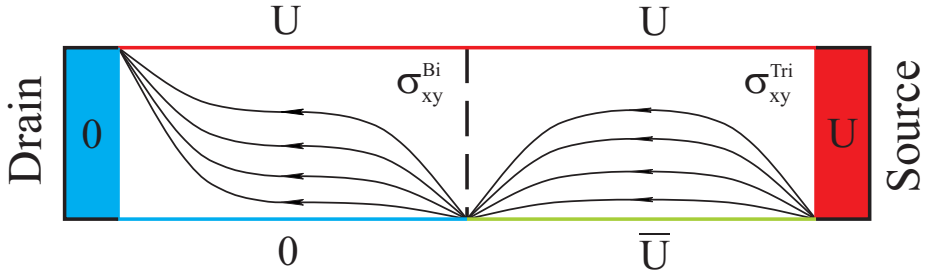

Figure 4.13: Schematic picture of the current lines in the sample under magnetic field perpendicular to the plane. Red and blue filled rectangles denote source and drain contacts with potential U and 0, respectively. Red, green and blue lines shows the lines of constant potential denoted with U, $\overline{U}$ and 0.

realised by the states on the Landau level, the trilayer is insulating and the current is carried only by the edge states, and vice versa.

The longitudinal resistance over the interface region of the flake is also shown in Fig. 4.12 as a green line. As seen it has a periodic structure with a period similar to that of the oscillations in R_{xx}^{Bi} and R_{xx}^{Tri}, and it does not go to zero at any gate voltage. First, one would assume that the interface longitudinal resistance includes longitudinal resistances of bilayer and trilayer. Then, in this case in R_{xx}^{Int} one should expect oscillations with twice smaller period than in R_{xx}^{Tri}. However, R_{xx}^{Int} oscillates with the same period and the phase is shifted by $\pi/2$.

One of the ways to understand this behaviour is to consider a classical model of the conductivity in a 2D sample in the quantum Hall regime. This model requires several assumptions to be made. First, in the quantum Hall regime it can be assumed that $\rho_{xx} \ll \rho_{xy}$. For example in our case while the maximum of oscillations in ρ_{xx}^{Tri} decreases from 0.8 kOhm at $V_G = 0$ to 0.3 kOhm at $V_G = 60$, $R_{xy}^{Tri} = \rho_{xy}^{Tri}$ changes from 4 kOhm to 1.3 kOhm at corresponding gate voltages. Therefore, in the first approximation this assumption is correct. Second, the transverse current J_y near the edge of the sample is zero, but also $\rho_{xx} \ll \rho_{xy}$ $J_y = -\sigma_{xy}E_x + \sigma_{yy}E_y \simeq -\sigma_{xy}E_x$, which means that $E_x = 0$ and therefore the edges of the sample are equipotentials as it is shown in Fig. 4.13. Source and drain contacts are also equipotentials, which means that the current lines are all coming from the corner of the sample (right bottom corner) and end in the opposite corner. Third, at the interface between bilayer and trilayer regions $J_x = \sigma_{xx}E_x + \sigma_{xy}E_y \simeq \sigma_{xy}E_y$. Both J_x and E_y have to be continuous through the interface due to the absence of the accumulated charge at the interface and boundary

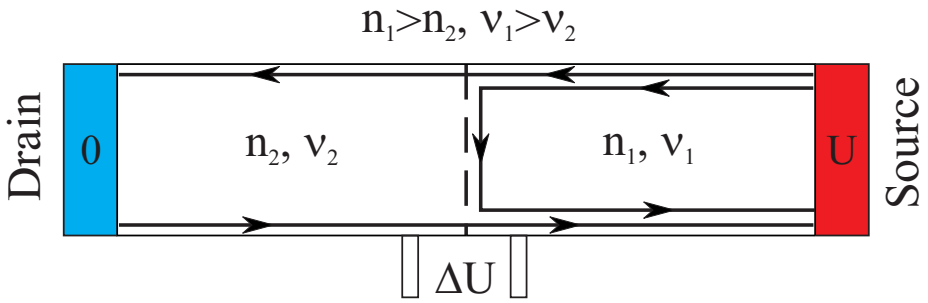

Figure 4.14: Propagation of the edge states through the boundary between two regions with different concentrations in the quantised regime.

conditions, respectively, therefore $J_x^{Tri} = J_x^{Bi}$ and $E_y^{Tri} = E_y^{Bi}$. However, $\sigma_{xy}^{Tri} \neq \sigma_{xy}^{Bi}$, thus $J_x^{Tri} = J_x^{Bi} = 0$ and $E_y^{Tri} = E_y^{Bi} = 0$. This means that the interface is a constant potential line and, therefore, no current flows along the interface.

In the given geometry with two regions of the sample with different transverse conductivities the lines of the current has to go in the way shown in the figure [80]. In this picture the right bottom corner separates two equipotentials: the source contact with potential U and the bottom edge of the trilayer region with potential $\overline{U}$. Also, the interface point on the bottom edge separates two edges with potentials $\overline{U}$ and 0. Thus, the measured interface resistance, R_{xx}^{Int}, is nothing but the voltage difference $\overline{U} - 0$ divided by the current I. For the full current flowing between the source and drain contacts it is known that

$$\begin{aligned} I &= \sigma_{xy}^{Tri}(U - \overline{U}), \\ I &= \sigma_{xy}^{Bi}(U - 0). \end{aligned} \tag{4.4}$$

Therefore $\overline{U}$ reads

$$\overline{U} = U\frac{\sigma_{xy}^{Tri} - \sigma_{xy}^{Bi}}{\sigma_{xy}^{Tri}} = \frac{I}{\sigma_{xy}^{Bi}}\frac{\sigma_{xy}^{Tri} - \sigma_{xy}^{Bi}}{\sigma_{xy}^{Tri}}. \tag{4.5}$$

Thus,

$$R_{xx}^{Int} = \frac{\overline{U}}{I} = \frac{\sigma_{xy}^{Tri} - \sigma_{xy}^{Bi}}{\sigma_{xy}^{Tri}\sigma_{xy}^{Bi}}. \tag{4.6}$$

Alternatively, one can obtain literally the same result within the Landauer-Buttiker formalism as it was done for p-n junctions in graphene [54]. Let us consider a system under a high magnetic field with two regions (bilayer and trilayer), which have corresponding positive carrier concentrations n_1 and n_2, $n_1 > n_2$. In case when in both regions the Fermi level lies between the Landau levels, the charge is carried by the edge states only, Fig. 4.14. The number of the active edge states is given by the filling fac-

tors ν_1 and ν_2, $\nu_1 > \nu_2$. Thus, there are ν_1 channels coming out of the source contact, which then split into ν_2 channels that go into the drain contact and $\nu_1 - \nu_2$ channels that flow along the interface and go back to the drain contact.

The formula for the voltage drop between the potential contacts ΔU in the given geometry reads [81]

$$\Delta U = \frac{\sum_i (1 + R_i - T_i) v_i^{-1}}{2 \sum_i v_i^{-1}} U. \tag{4.7}$$

Here v_i is the Fermi velocity of the i-th channel, T_i and R_i are the total transmission and reflection probabilities into the i-th channel and U is the voltage difference between the source and drain contacts. In our case, assuming that the channels do not mix with each other, the probabilities are simply equal to zero and unity

$$\begin{aligned} &\text{for } \nu_2 \text{ channels} && R = 0,\ T = 1, \\ &\text{for } \nu_1 - \nu_2 \text{ channels} && R = 1,\ T = 0. \end{aligned} \tag{4.8}$$

Then, assuming that the Fermi velocities are the same for all channels and using the values for probabilities one can rewrite Eq. 4.7

$$\Delta U = \frac{\nu_2(1 + 0 - 1) + (\nu_1 - \nu_2)(1 + 1 - 0)}{2 \sum_i 1} U = \frac{\nu_1 - \nu_2}{2\nu_1} U. \tag{4.9}$$

The current I through the sample is determined by the number of states that propagates through the whole system, therefore

$$I = \frac{e^2}{h} \nu_2 U. \tag{4.10}$$

Thus, the conductance measured by the potential contacts is

$$G = \frac{e^2}{h} \frac{\nu_1 \nu_2}{\nu_1 - \nu_2}, \tag{4.11}$$

which is practically the same formula as in Eq. 4.6.

Strictly speaking, the applicability of both approaches in our case is at least questionable. The classic one does not take into account the quantum nature of the phenomenon, whereas the Landauer-Buttiker formalism is based on the assumption of the

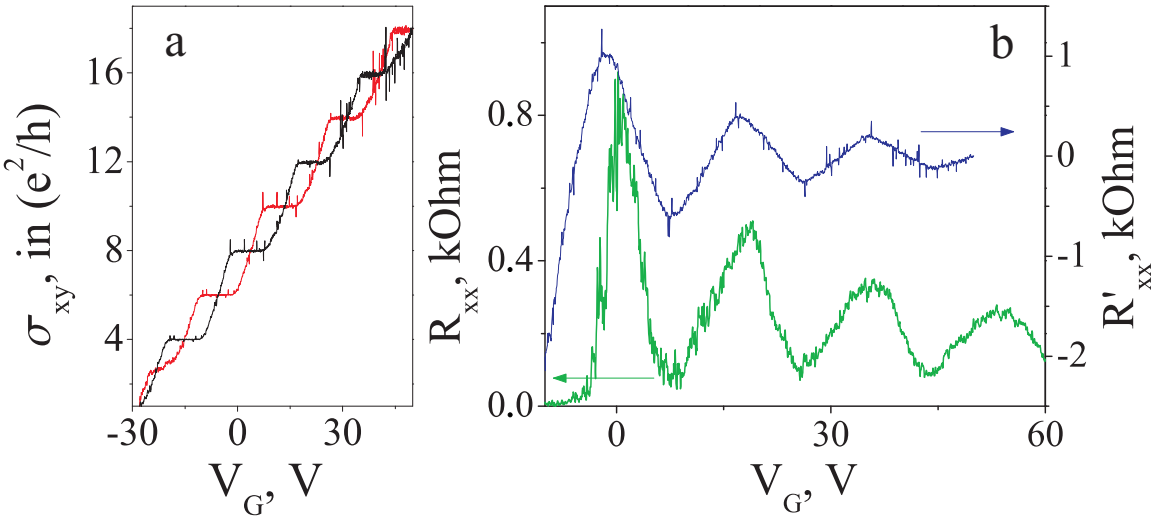

Figure 4.15: (a) $\sigma_{xy}^{Tri}(V_G)$ (red) and $\sigma_{xy}^{Bi}(V_G)$ (black) obtained as a shifted curve for trilayer ($T = 170\,\mathrm{mK}$, $B = 15\,\mathrm{Tesla}$). (b) Interface resistance as a function of the gate voltage. Green curve shows the measured dependence while the blue curve shows the calculated one.

ballistic transport and, therefore cannot describe the diffusive contribution to the resistance from the bulk of the sample. However, we will apply the formula 4.6 and compare the obtained dependence with that measured in the experiment. Knowing transverse conductivities of trilayer and bilayer parts one can calculate the longitudinal resistance of the interface. σ_{xy}^{Tri} can be calculated from the measured R_{xx}^{Tri} and R_{xy}^{Tri}, while σ_{xy}^{Bi} is unknown since the transverse conductivity of bilayer was not measured. However, since the position of the plateaus is roughly known, one can approximate σ_{xy}^{Bi} with σ_{xy}^{Tri} but shifted down by $2e^2/h$ and to the left by half a distance in V_G between adjacent plateaus. Of course, this will give only a qualitative picture for R_{xx}^{Int}.

In Fig. 4.15(a) σ_{xy}^{Tri} and approximation for σ_{xy}^{Bi} are shown. Calculated dependence of the longitudinal interface resistance on the gate voltage is plotted in Fig. 4.15(b) along with the measured dependence. It is seen that there is a very good agreement in positions of maxima and minima between calculated and measured functions. It is worth noting that the evaluated R_{xx}^{Int} oscillates around zero taking positive and negative values. The measured dependence is always positive. This means that although the longitudinal resistivities are smaller than the transverse, they cannot be neglected completely and lead to a weakly changing background. This background sums with oscillations and results in the measured dependence.

Thus the oscillating behavior of the longitudinal resistance of the interface between

bilayer and trilayer graphene in the quantum Hall regime can be explained by Eq. 4.6 and is determined only by the transversal conductivity. The actual resistance coming from the transition between the carriers in bilayer and trilayer graphene may or may not contribute to the measured values. Up to now there are no theoretical expectations for such a resistance and it is not possible to determine and reveal its contribution to the measured value.

4.4 Conclusion

The initial aim of the measurements described in this chapter was to reveal and investigate the propagation of the carriers through the interface between the regions of different thickness. However, at this stage the only confirmation of the effect of the interface is the presence of the interface resistance, which also depends on the gate voltage, has a maximum close to the Dirac point and changes with temperature in a similar way to the bulk bilayer and trilayer. No theoretical predictions have been made for such resistance and the model suggested here was unable to explain the observed behaviour.

The magnetotransport in the structure did not show any particular features that could be ascribed to the interface effect, but showed a behaviour expected for the system that consists of the two regions with different matrices of resistivity. However, bilayer and trilayer regions were studied separately at high magnetic fields and exhibited the expected quantisation of the energy bands seen in both longitudinal and transversal resistivities. Stacking order of the trilayer graphene region (ABA/ABC) was not determined since different features of the results suggested different orders.

As far as the authors are aware, a graphene structure with regions of different thickness was investigated experimentally and described here for the first time. Only one sample was measured and the results have already revealed interesting features of the transport through the interface. Potentially, with better quality sample it will be possible to study these effects in detail.

Chapter 5

Suggestions for further work

As one can see, many questions discussed in this thesis remain unanswered and require further investigation.

The development of the technology of producing multiterminal stencil masks for contacts evaporation was stopped at an early stage, where it was possible to make only one slot in the Si_3N_4 membrane of $2\,\mu$m by $70\,\mu$m size. However, the need for clean graphene multiterminal devices (for instance, for ballistic transport measurements) is present, and employment of such masks is one of the ways to produce them.

Our experiments on the doping of graphene with both inorganic (water) and organic molecules showed a new type of doping effect associated with electrochemical reactions. In spite of the fact that it was consistently shown that toluene undergoes such a reaction in the vicinity of graphene, some details of this process are still unexplored. For example, analysing the product reactants, it would be possible to find the exact initial reactants (which are referred to in this work as third reactant) and to propose an exact reaction. Also, mechanism of the influence of the dipole moment of the molecules on their doping effects is still unclear. Finally, water was suggested to dope in a similar way to toluene, although no investigation of the characteristic times of the corresponding electrochemical reaction has been done.

The flicker noise in graphene was demonstrated to be a sensitive tool for distinguishing between different types of scattering potential, in particular short- and long-range ones. However, up to now there has been no consistent theoretical model which would describe both the concentration and temperature dependences of the noise. Also, experimentally noise was not carefully investigated in both suspended samples and samples

on different substrates and was barely touched in bilayer devices. The development of generalised understanding of the flicker noise would allow one to separate the signatures of various scattering potentials in the noise behaviour and, therefore, would help to identify the dominant type of scatterers contributing to the noise.

In this work the trilayer graphene was investigated in the quantum Hall regime and different signatures of the stacking order were seen. In order to study these effects in more detail a sample of a better quality is required.

For the first time the measurements of the conductance of the 2/3 layer graphene structure were presented. Dependence of the interface resistance on temperature and carrier concentration was measured, although no theoretical model to explain the observed behaviour was proposed. Similar studies in 1/2 layer structures are needed for the complete understanding of the phenomenon.

Bibliography

[1] Reich, S., Thomsen, C., and Maultzsch, J. *Carbon Nanotubes: Basic Concepts and Physical Properties*. Wiley, (2004).

[2] Reich, S., Maultzsch, J., Thomsen, C., and Ordejón, P. *Phys. Rev. B* **66**, 035412 (2002).

[3] Castro Neto, A. H., Guinea, F., Peres, N. M. R., Novoselov, K. S., and Geim, A. K. *Rev. Mod. Phys.* **81**, 109–162 (2009).

[4] Geim, A. K. *Science* **324**(5934), 1530–1534 (2009).

[5] Novoselov, K. S., Geim, A. K., Morozov, S. V., Jiang, D., Katsnelson, M. I., Grigorieva, I. V., Dubonos, S. V., and Firsov, A. A. *Nature* **438**, 197–200 (2005).

[6] Gorbachev, R. V., Mayorov, A. S., Morozov, S. V., Zhukov, A. A., Blake, P., Ponomarenko, L. A., Grigorieva, I. V., Novoselov, K. S., Guinea, F., and Geim, A. K. *Nat Phys* **7**, 701–704 (2011).

[7] Ando, T., Nakanishi, T., and Saito, R. *Journal of the Physical Society of Japan* **67**(8), 2857–2862 (1998).

[8] Katsnelson, M. I., Novoselov, K. S., and Geim, A. K. *Nat Phys* **2**, 620–625 (2006).

[9] Novoselov, K. S., Geim, A. K., Morozov, S. V., Jiang, D., Zhang, Y., Dubonos, S. V., Grigorieva, I. V., and Firsov, A. A. *Science* **306**(5696), 666–669 (2004).

[10] Sze, S. M. *Physics of Semiconductor Devices*. Wiley, (2006).

[11] Ponomarenko, L. A., Yang, R., Mohiuddin, T. M., Katsnelson, M. I., Novoselov, K. S., Morozov, S. V., Zhukov, A. A., Schedin, F., Hill, E. W., and Geim, A. K. *Phys. Rev. Lett.* **102**, 206603 (2009).

[12] Gorbachev, R. V., Riaz, I., Nair, R. R., Jalil, R., Britnell, L., Belle, B. D., Hill, E. W., Novoselov, K. S., Watanabe, K., Taniguchi, T., Geim, A. K., and Blake, P. *Small* **7**(4), 465–468 (2011).

[13] Dean, C. R., Young, A. F., Meric, I., Lee, C., Wang, L., Sorgenfrei, S., Watanabe, K., Taniguchi, T., Kim, P., Shepard, K. L., and Hone, J. *Nat Nano* **5**, 722–726 (2010).

[14] Blake, P., Hill, E. W., Neto, A. H. C., Novoselov, K. S., Jiang, D., Yang, R., Booth, T. J., and Geim, A. K. **91**(6), 063124 (2007).

[15] Novoselov, K. S., McCann, E., Morozov, S. V., Fal/'ko, V. I., Katsnelson, M. I., Zeitler, U., Jiang, D., Schedin, F., and Geim, A. K. *Nat Phys* **2**, 177–180 (2006).

[16] Zhang, Y., Tan, Y.-W., Stormer, H. L., and Kim, P. *Nature* **438**, 201–204 (2005).

[17] Ferrari, A. C., Meyer, J. C., Scardaci, V., Casiraghi, C., Lazzeri, M., Mauri, F., Piscanec, S., Jiang, D., Novoselov, K. S., Roth, S., and Geim, A. K. *Phys. Rev. Lett.* **97**, 187401Oct.

[18] Russo, S., Craciun, M., Yamamoto, M., Morpurgo, A., and Tarucha, S. *Physica E: Low-dimensional Systems and Nanostructures* **42**(4), 677 – 679 (2010).

[19] Gorbachev, R. V., Mayorov, A. S., Savchenko, A. K., Horsell, D. W., and Guinea, F. *Nano Letters* **8**(7), 1995–1999 (2008).

[20] Martin, J., Akerman, N., Ulbricht, G., Lohmann, T., Smet, J. H., von Klitzing, K., and Yacoby, A. *Nat Phys* **4**(2), 144–148 (2008).

[21] Cheianov, V. V., Fal'ko, V. I., Altshuler, B. L., and Aleiner, I. L. *Phys. Rev. Lett.* **99**(17), 176801 (2007).

[22] Commercially available conductive Silver Paint at uk.rs-online.com, product no.:123768.

[23] Commercially available G-vanish glue at uk.rs-online.com, product no.:123768.

[24] In this work 1 mm size squared windows of 200 μm and 500 μm thicknesses on a 10 mm frame were used. Available at www.silson.com.

[25] Chen, J.-H., Jang, C., Ishigami, M., Xiao, S., Cullen, W., Williams, E., and Fuhrer, M. *Solid State Communications* **149**(27-28), 1080 – 1086 (2009).

[26] Shon, N. H. and Ando, T. *Journal of the Physical Society of Japan* **67**(7), 2421–2429 (1998).

[27] Adam, S., Hwang, E., Rossi, E., and Sarma, S. D. *Solid State Communications* **149**(27-28), 1072 – 1079 (2009).

[28] Ando, T. *Journal of the Physical Society of Japan* **75**(7), 074716 (2006).

[29] Tikhonenko, F., Horsell, D., Wilkinson, B., Gorbachev, R., and Savchenko, A. *Physica E: Low-dimensional Systems and Nanostructures* **40**(5), 1364 – 1366 (2008).

[30] Stauber, T., Peres, N. M. R., and Guinea, F. *Phys. Rev. B* **76**, 205423 (2007).

[31] Ni, Z. H., Ponomarenko, L. A., Nair, R. R., Yang, R., Anissimova, S., Grigorieva, I. V., Schedin, F., Blake, P., Shen, Z. X., Hill, E. H., Novoselov, K. S., and Geim, A. K. *Nano Letters* **10**(10), 3868–3872 (2010).

[32] Katsnelson, M. and Geim, A. *Philosophical Transactions of the Royal Society A: Mathematical, Physical and Engineering Sciences* **366**(1863), 195–204 (2008).

[33] Castro, E. V., Ochoa, H., Katsnelson, M. I., Gorbachev, R. V., Elias, D. C., Novoselov, K. S., Geim, A. K., and Guinea, F. *Phys. Rev. Lett.* **105**, 266601 (2010).

[34] Hung, K., Ko, P., Hu, C., and Cheng, Y. *IEEE Transactions on Electron Devices* **37**(3), 654 –665 (1990).

[35] Young, A. F. and Kim, P. *Nature Physics* **5**(3), 222–226 (2009).

[36] Katsnelson, M. I., Novoselov, K. S., and Geim, A. K. *Nature Physics* **2**(9), 620–625 (2006).

[37] Schedin, F., Geim, A. K., Morozov, S. V., Hill, E. W., Blake, P., Katsnelson, M. I., and Novoselov, K. S. *Nature Materials* **6**(9), 652–655 (2007).

[38] Ohno, Y., Maehashi, K., Yamashiro, Y., and Matsumoto, K. *Nano Letters* **9**(9), 3318–3322 (2009).

[39] Cheianov, V. V., Syljuåsen, O., Altshuler, B. L., and Fal'ko, V. *Phys. Rev. B* **80**(23), 233409 (2009).

[40] Castro Neto, A. H., Guinea, F., Peres, N. M. R., Novoselov, K. S., and Geim, A. K. *Rev. Mod. Phys.* **81**(1), 109–162 (2009).

[41] Headen, T. F., Howard, C. A., Skipper, N. T., Wilkinson, M. A., Bowron, D. T., and Soper, A. K. *Journal of the American Chemical Society* **132**(16), 5735–5742 (2010).

[42] Zhang, Y., Liu, C., Shi, W., Wang, Z., Dai, L., and Zhang, X. *Langmuir* **23**(15), 7911–7915 (2007). PMID: 17590031.

[43] Blake, P., Hill, E. W., Neto, A. H. C., Novoselov, K. S., Jiang, D., Yang, R., Booth, T. J., and Geim, A. K. *Applied Physics Letters* **91**(6), 063124 (2007).

[44] Ferrari, A. C., Meyer, J. C., Scardaci, V., Casiraghi, C., Lazzeri, M., Mauri, F., Piscanec, S., Jiang, D., Novoselov, K. S., Roth, S., and Geim, A. K. *Phys. Rev. Lett.* **97**(18), 187401 Oct (2006).

[45] Lide, D. R. *CRC Handbook of Chemistry and Physics*. Cambridge University Press, 74 edition, (1994).

[46] http://www.epa.gov/chemfact/.

[47] Oja, V. and Suuberg, E. M. *Journal of Chemical and Engineering Data* **43**(3), 486–492 (1998).

[48] www.sigmaaldrich.com, 95305 TraceSELECT (FLUKA).

[49] Schmickler, W. *Interfacial Electrochemistry*. Oxford University Press, New York, (1996).

[50] Pinto, H., Jones, R., Goss, J. P., and Briddon, P. R. *Physica status solidi (a)* **207**(9), 2131–2136 (2010).

[51] Pinto, H. HOMO/LUMO levels were calculated using DFT.

[52] Wehling, T. O. and Katsnelson, A. I. L. M. I. *Applied Physics Letters* **93**, 202110 (2008).

[53] Wehling, T. O., Novoselov, K. S., Morozov, S. V., Vdovin, E. E., Katsnelson, M. I., Geim, A. K., and Lichtenstein, A. I. *Nano Letters* **8**(1), 173–177 (2008).

[54] Lohmann, T., v. Klitzing, K., and Smet, J. H. *Nano Letters* **9**(5), 1973–1979 (2009).

[55] Dan, Y., Lu, Y., Kybert, N. J., Luo, Z., and Johnson, A. T. C. *Nano Letters* **9**(4), 1472–1475 (2009).

[56] Bard, A. J. and Faulkner, L. R. *Electrochemical Methods: Fundamentals and Applications*. John Wiley & Sons, Inc, second edition, (2001).

[57] Kogan, S. *Electronic noise and fluctuations in solids*. Cambridge University Press, Cambridge, (1996).

[58] Kirton, M. and Uren, M. *Advances in Physics* **38**(4), 367–468 (1989).

[59] Lin, Y.-M. and Avouris, P. *Nano Letters* **8**(8), 2119–2125 (2008).

[60] Pal, A. N. and Ghosh, A. *Phys. Rev. Lett.* **102**(12), 126805 (2009).

[61] Liu, G., Stillman, W., Rumyantsev, S., Shao, Q., Shur, M., and Balandin, A. A. *Applied Physics Letters* **95**(3), 033103 (2009).

[62] Shao, Q., Liu, G., Teweldebrhan, D., Balandin, A. A., Roumyantesv, S., Shur, M., and Yan, D. *Electron Device Letters, IEEE* **30**(3), 288 – 290 (2009).

[63] Cheng, Z., Li, Q., Li, Z., Zhou, Q., and Fang, Y. *Nano Letters* **10**(5), 1864–1868 (2010).

[64] Pal, A. N., Ghatak, S., Kochat, V., Sneha, E. S., Arjun, B. S., Raghavan, S., and Ghosh, A. *arXiv:1009.5832v2* (2010).

[65] Martin, J., Akerman, N., Ulbricht, G., Lohmann, T., Smet, J. H., von Klitzing, K., and Yacoby, A. *Nat Phys* **4**(2), 144–148 (2008).

[66] Lafkioti, M., Krauss, B., Lohmann, T., Zschieschang, U., Klauk, H., v. Klitzing, K., and Smet, J. H. *Nano Letters* **10**(4), 1149–1153 (2010).

[67] Schedin, F., Geim, A. K., Morozov, S. V., Jiang, D., Hill, E. H., Blake, P., and Novoselov, K. S. *Nature Materials* **6**, 652 (2007).

[68] Kaverzin, A., Strawbridge, S., Price, A., Withers, F., Savchenko, A., and Horsell, D. *Carbon* **49**(12), 3829 – 3834 (2011).

[69] Morozov, S. V., Novoselov, K. S., Katsnelson, M. I., Schedin, F., Elias, D. C., Jaszczak, J. A., and Geim, A. K. *Phys. Rev. Lett.* **100**, 016602 Jan (2008).

[70] Nakanishi, T., Koshino, M., and Ando, T. *Phys. Rev. B* **82**, 125428 (2010).

[71] Koshino, M., Nakanishi, T., and Ando, T. *Phys. Rev. B* **82**, 205436 (2010).

[72] Taychatanapat, T., Watanabe, K., Taniguchi, T., and Jarillo-Herrero, P. *Nature Physics* **7**, 621–625 (2011).

[73] Morozov, S. V., Novoselov, K. S., Katsnelson, M. I., Schedin, F., Elias, D. C., Jaszczak, J. A., and Geim, A. K. *Phys. Rev. Lett.* **100**, 016602 (2008).

[74] Koshino, M. and McCann, E. *Phys. Rev. B* **80**, 165409 (2009).

[75] Yuan, S., Roldán, R., and Katsnelson, M. I. *Phys. Rev. B* **84**, 125455 (2011).

[76] Kumar, A., Escoffier, W., Poumirol, J. M., Faugeras, C., Arovas, D. P., Fogler, M. M., Guinea, F., Roche, S., Goiran, M., and Raquet, B. *Phys. Rev. Lett.* **107**, 126806 (2011).

[77] Zhang, L., Zhang, Y., Camacho, J., Khodas, M., and Zaliznyak, I. *Nat Phys* (2011).

[78] Koshino, M. and McCann, E. *Phys. Rev. B* **79**, 125443 (2009).

[79] Jiang, Z., Zhang, Y., Stormer, H. L., and Kim, P. *Phys. Rev. Lett.* **99**, 106802 (2007).

[80] Davies, J. H. *The Physics of Low-dimensional Semiconductors.* Cambridge University Press, (1998).

[81] Büttiker, M., Imry, Y., Landauer, R., and Pinhas, S. *Phys. Rev. B* **31**, 6207–6215 (1985).

Appendix A

Statistics of the samples

Sample name	PMMA	Water H_2O	Toluene $C_6H_5CH_3$	Aniline $C_6H_5NH_3$	Naphthaline $C_{10}H_8$	Pyrene $C_{16}H_{10}$	Mobility $cm^2V^{-1}sec^{-1}$	L*W $\mu m*\mu m$	Contacts
AG1D1F1	+	+	+	-	-	-	7900	9*4	4
AG2D4	+	-	+	-	-	-	-	5.7*3	3
AG3D10	-	-	+	-	-	-	-	18*	2
AG4D1	+	-	+	-	-	-	-	7*7	4
AG4D4	+	-	+	+	-	-	9700	4*2	4
AG5D1	-	-	+	+	+	+	-	18*2	2
AS1D1	-	-	+	-	+	-	-	18*	2
G16D3F1	+	+	-	-	-	-	11500	5.3*4.1	4
G22D8	+	-	+	-	-	-	-	19*18	4
GB7N4D	+	+	-	-	-	-	11000	6*2.3	4
RP1	+	+	-	-	-	-	10000	6*3	4

Doping samples. Mobility is given as an approximate value calculated at $n \gtrsim 10^{12}\,\mathrm{cm}^{-2}$. Plus in the column with a dopant (like "H_2O") means that the doping effect of this dopant was measured on the sample. Minus in the column "PMMA" means that the sample was produced with a PMMA free fabrication technique.